UNIVERSITÄT DES SAARLANDES

INM
Leibniz-Institut für Neue Materialien

Hydrogel-Based Side-Emitting Optical Waveguides for Light and Heat Delivery

Dissertation

zur Erlangung des Grades

des Doktors der Naturwissenschaften

der Naturwissenschaftlich-Technischen Fakultät

der Universität des Saarlandes

von

Zahra Kafrashian

Saarbrücken

2025

Tag des Kolloquiums:	13.11.2025
Dekan:	Prof. Dr.-Ing. Dirk Bähre
Berichterstatter:	Prof. Dr. Aránzazu del Campo Bécares
	Prof. Dr. Guido Kickelbick
Akad. Mitglied:	Dr. Shrikrishnan Sankaran

Hydrogel-Based Side-Emitting Optical Waveguides for Light and Heat Delivery

Zahra Kafrashian

Aus Tehran, Iran

DISSERTATION

INM-Leibniz Institut für neue Materialien, Saarbrücken

مولانا شمس را گفت:

پس زخم هایمان چه؟!

و او پاسخ داد:

نور از محل آنها وارد میشود

Abstract

Side-emitting optical fibers enable controlled light delivery along their length. A major challenge in fabricating soft, side-emitting fibers for biomedical use is achieving continuous processing with tunable optical properties along the fiber axis. This thesis presents hydrogel-based optical fibers with tunable side-emission using multimaterial extrusion printing. Diacrylated Pluronic F-127 (PluDA) serves as the waveguiding ink, while a PluDA-nanoparticle mix acts as the scattering ink. By switching between inks, 1 mm diameter fibers with segments up to <500 µm are produced continuously. Segment length is controlled by adjusting the switching time. Side-emission is evaluated via fluorescence excitation in a hydrogel with fluorescent particles, demonstrating controlled light distribution in a simulated biological environment.

To add photothermal functionality, plasmonic nanomaterials are embedded in PluDA inks. Gold nanorods are used to enable localized heating under NIR light. Core-cladding waveguides are printed with refractive index contrast achieved by varying PluDA content. Stability and spatially controlled heating are assessed under 808 nm irradiation.

This research advances the design and fabrication of soft optical waveguides by developing inks and processing windows for multimaterial extrusion printing. The findings contribute to the development of waveguides for biomedical applications, like targeted optical stimulation or localized hyperthermia treatments.

Zusammenfassung

Seitlich abstrahlende optische Fasern ermöglichen eine kontrollierte Lichtabgabe entlang ihrer Länge. Eine zentrale Herausforderung bei der Herstellung weicher, seitlich abstrahlender Fasern für biomedizinische Anwendungen ist die kontinuierliche Fertigung mit anpassbaren optischen Eigenschaften entlang der Faserachse. Diese Arbeit stellt Hydrogel-basierte optische Fasern mit steuerbarer Seitenemission vor, gefertigt mittels multimaterialiellem Extrusionsdruck. Diacryliertes Pluronic F-127 (PluDA) dient als lichtleitende Tinte, eine Mischung aus PluDA und Nanopartikeln als streuende Tinte. Durch Wechsel der Tinten entstehen kontinuierlich Fasern mit 1 mm Durchmesser und Segmentlängen von bis ≤500 µm, präzise gesteuert über die Schaltzeit. Die Seitenemission wird durch Fluoreszenzanregung in einem Hydrogel mit fluoreszierenden Partikeln bewertet und zeigt eine kontrollierte Lichtverteilung in simuliertem Gewebe. Zur Integration photothermischer Funktionalität werden plasmonische Nanomaterialien in PluDA eingebettet. Goldnanorods ermöglichen lokales Erhitzen unter NIR-Licht. Kern-Mantel-Wellenleiter mit Brechungsindexkontrast entstehen durch Variation des PluDA-Gehalts. Stabilität und ortsabhängige Erwärmung werden unter 808 nm Bestrahlung untersucht. Diese Arbeit unterstützt die Entwicklung weicher optischer Wellenleiter für gezielte Lichtstimulation oder lokale Hyperthermie.

Dedication

To my mother, who has always believed in me and never doubted what I am capable of. As a science teacher, she nurtured my curiosity and encouraged me to explore and think beyond the frames. Whenever I am afraid, she reminds me, "*What you want is just one step beyond the fear. You just need to take that step*." And no matter what, she tells me, "*I will always love and support you.*" These words have been my light on the hardest days, giving me strength when I needed it most.

To my beloved grandfather,

And To the passengers of flight PS752, many of whom were unable to complete their PhDs.

Acknowledgments

I recently came across an old note on my lab bench that read, "It's gonna work one day." I had written it during one of the most discouraging days of my PhD, when every experiment I had planned that week had failed, and I had absolutely no idea how to move forward. Hundreds of coffees and a couple of months later, here we are. It did work. And for that, I owe a great deal of gratitude to an incredible group of people who kept me going.

First, I would like to thank my supervisor, Prof. Aránzazu del Campo, for trusting me and giving me the opportunity to join the Dynamic Biomaterials group at INM Leibniz Institute for New Materials. I learned so much under your guidance over the years and it helped me grow a lot. My sincere thanks also go to Dr. Samuel Pearson, who patiently guided me through the many hurdles of the PhD. Thank you for having my back on the tough days, offering your meticulous advice and for unofficially being my free therapist.

A big thanks to Stefan Brück, who supported me in the lab, helped with Python scripts, and the phantom tissue experiments and also for always having an exciting box of candy on your desk, which became a source of joy after long lab days. I'm grateful to Dr. Peter Rogin for his guidance in Laser Lab 1.05. Your help and input with laser alignments and experimental design was invaluable. Selim Basaran, thank you for your support with the IR camera measurements, laser alignments, and data analysis. I'm also thankful to Bruno Schäfer for helping with the refractive index measurements. Daniel Sanchez, it was a pleasure supervising you, and your help in designing the core–shell–shell nozzles was essential.

A warm thank you to the INM staff, always helpful and kind, especially Ralf Muth and his team for their constant IT support. Big thanks to Martina Bonnard and Sabine Müller for their help since the beginning of my stay here in Germany. My appreciation also goes to the INM workshop team, whose expertise in designing and fabricating holders and nozzles made a significant difference in my work, and to Ms. Meiser for making the most amazing Sahnekuchen.

To all members of Dynamic Biomaterials and Bioprogrammable Materials, especially those in chemistry and bioprinting labs. Thank you for creating such a collaborative and fun environment. Hanuman, thank you for taking responsibility for everything and everything being your fault.

To my friends and colleagues and officemates at INM. Thank you for all the table tennis matches and volleyball and football (?) tournaments that sharpened both our reflexes and our patience alongside our PhDs. And to basketball, my loyal companion through the years that always brought me to the right people, including Gloria and Ansaf, who now feel like my family here in Germany.

Narges, you were always there during the toughest moments. Your support, wise advice, attentive listening, and your unforgettable saffron chicken meant the world to me. Thanks to my lifelong friends, Niloofar and Anahita, for sticking with me through every phase since our bachelor days. My amazing friends in the MEMS Laboratory in Tehran, Pouria, Sina, Aida, Sepide, Maral, and Ali, made up my first collaborative and scientific professional experience, for which I remain deeply grateful.

Léo, you joined me halfway through this journey, and since then, you've been an incredible source of love, strength, care, and comfort, not to mention amazing coffee and pancakes. You encouraged me through the toughest moments and always found wise and thoughtful solutions when I needed them most.

And last but most importantly to my dearest parents, supportive, kind brother and my beautiful little sister. Your unconditional love and the values you've instilled in me have been the foundation of everything I've done. Thank you for always being there even in distance. We made it 😊

To those I may have unintentionally left out, know that your kindness and support live in my heart. I am deeply grateful, and I look forward to what comes next.

Table of Content

Motivation

The interactions of light with tissue — reflection, refraction, absorption, and scattering— limit the penetration of light in the body to 1-5 mm [1] depending on the light wavelength. In light-based therapies, implantable optical waveguides offer a pathway for light delivery at longer depths. Rigid optical fibers based on silica glass, polycarbonates, polyimides, or polyacrylates have been used for this purpose in optogenetics or photothermal therapies, but the mechanical mismatch between the hard fiber and the soft tissue limits their biocompatibility. Soft elastomeric or hydrogel-based optical fibers are better alternatives from a biocompatibility perspective, as they can be engineered to have comparable optical performance to polymeric fibers (0.1 – 1 dB cm^{-1} in visible wavelength ranges) and comparable mechanical properties to natural tissues (Young's Modulus 1-100 kPa).

Rigid optical fibers are typically fabricated by extrusion or thermal drawing of thermoplastic rigid materials. These processing technologies have experienced huge development and allow continuous fabrication of rigid fibers with different geometries (planar, circular), surface patterns and dimensions. Using coaxial nozzles in extrusion processes or multimaterial preforms in thermal drawing, multilayer fibers integrating waveguiding, conductivity, or sensing functions can be fabricated in one step and attract interest in the field of optoelectronic fibers and textiles. [2] Post-processing of the fibers by laser micromachining allows patterning additional functional features at spatially defined positions along the fiber length. This allows, for example, to modify the internal reflection properties along the fiber and deliberately outcouple light (side-emission) at specific illumination areas.

In contrast to extrusion and thermal drawing processes for rigid fibers, soft elastomeric or hydrogel optical fibers are typically fabricated by molding reactive precursor mixtures or physical hydrogels. To integrate additional functionalities, coaxial layers are added in sequential molding processes. These are typically performed manually[3] and difficult to transfer into continuous processes. In recent years, extrusion printing technologies have expanded the possibilities to process soft, structured multimaterial filaments by co-extruding inks of different properties along the fiber axes to build multi-shell filaments using coaxial nozzles,[4] Janus filaments using single Y or V-shaped nozzles with multiple inlets,[5] multicore filaments using microfluidics printing heads,[6] and more recently filaments with helicoidal cores using rotational

printing heads.[7] In coaxial extrusion printing, processing conditions (temperature, pressure) and material flow properties can be combined synergistically to flexibly tune the dimensions and structure of the filament as it is extruded. More recently, the possibility to vary the compositions and material's properties along the filament has been realized. Filaments with gradient composition using mixing nozzles[8] or multimaterial segmented filaments by switching the flow between inlets of a single nozzle[9] have been reported from photocurable silicones and thermo-reversible hydrogels as inks. Most of the reported work has focused on additive manufacturing of large and structurally complex 3D multimaterial structures.

The wide portfolio of soft inks developed over the last decade in the field of soft electronics and biofabrication,[10] and the intrinsic processing flexibility in soft multimaterial extrusion printing makes this technology potentially interesting to expand the functionalities of soft optical and optoelectrical fibers and textiles, and to allow their continuous fabrication (in contrast to molding). This requires the development of printable soft optical materials that can fulfil multiple processing and functional requirements. Printability in terms of extrudability, filament formation and shape fidelity, involves materials properties like viscosity, shear thinning, yield stress, surface tension or crosslinking kinetics, among others. Optical functions relate to material parameters like transparency, homogeneity, refractive index or surface finish. In a multimaterial filament context, dissimilar properties at the geometrical boundaries between segments of different materials can become critical sites for stability and performance. The design of printable and functional multimaterials is a timely scientific challenge and establishes the scenario to which the work in this thesis contributes.

One such challenge is the processing of fibers with controlled light outcoupling along their length, which is crucial for applications requiring light irradiation of a certain volume (in contrast to end-point irradiation). This can be achieved by introducing internal scatterers along the fiber axes, such as bubbles or solid particles, which allows control over the emission profile by adjusting their size, density or distribution. This has been achieved in manual moulding, which is a batch process with limited scalability.

To overcome this limitation, fabrication methods such as multimaterial extrusion printing can be of interest. Multimaterial extrusion printing allows for the continuous deposition of different materials in a single process. This enables the creation of fibers with alternating compositions, material properties, and geometries along their length, which is useful for achieving multiple functionalities in optical fibers. Lewis et al.[11] developed a microfluidic printhead capable of switching between two viscoelastic materials, achieving fine control over material transitions

within fibers at resolutions as small as 520 µm, later improved to 320 µm using a pneumatic pressure controller.[9a] This allowed for complex material compositions by handling up to eight different inks. Building on these advancements, this thesis focuses on the development of controlled side-emitting optical fibers using a multi-material extrusion printing approach. The method includes the design of a customized 3D-printed Y-shaped nozzle for extrusion of two inks with different optical properties: waveguiding and scattering. By adjusting the scatterer distribution along the fiber's longitudinal axis, it will be possible to control the light outcoupling pattern and emit light with customized intensity profiles.

Waveguides in photomedical applications are not only used to transport light, but also to localize heating in photothermal therapies. Multimaterial fibers, as conceived in this thesis, can also be of help in this context by replacing scattering elements with plasmonic particles, which can generate localized heat when exposed to near-infrared light. This possibility is tested in this thesis using plasmonic nanorods, which are well known for their ability to convert light energy into heat. Fibers that can deliver both light and heat in a targeted and controllable manner are therefore the main focus of this work to develop useful materials and devices for combined light- and heat-based therapies.

This research is organized into six main chapters:

Chapter 1 provides a comprehensive review of the current state of multi-material extrusion printing, with a focus on extrusion techniques, different strategies for side emission in optical fibers, and the integration of plasmonic hydrogels into waveguides.

Chapter 2 details the fabrication method developed for multi-material extrusion printing of segmented core and core-cladding waveguides. This chapter explains the design of the custom Y-shaped nozzle and outlines the step-by-step process for printing waveguides with integrated scatterers or plasmonic elements. The chapter also highlights the challenges overcome during the printing process and discusses the benefits of using this scalable technique for continuous fiber fabrication.

Chapter 3 presents the results of controlled side-emission experiments. It demonstrates how the scatterer distribution within the fibers can be tuned to achieve specific outcoupling patterns, and it discusses the successful activation of fluorophores within the phantom gel. The results highlight the ability to design and fabricate fibers with precise light distribution, which can be applied in a range of medical and therapeutic applications.

Chapter 4 focuses on the thermal studies of the segmented plasmonic waveguides. This chapter explores how different fiber patterns influence heat generation within the waveguide, and it presents results from the NIR light-induced heating experiments. The chapter also discusses the potential of these fibers for photothermal therapies and heat-triggered drug delivery.

Chapter 5 concludes the thesis by summarizing the key findings of the research and discusses broader implications of the printed waveguides in the context of optical devices for therapeutic applications.

Chapter 6 contains the materials and methods, which includes all the materials used, as well as detailed experimental methods.

1. State of the art

1.1. Optical waveguides for photomedicine

Light is a non-invasive tool for in vivo diagnostics and therapy.[12] The ability to tune light at different wavelengths and doses facilitates the manipulation of light-dependent processes for various applications, from illuminating microscopic structures in imaging techniques to activating specific biochemical reactions in phototherapy.[13]

Light's interactions with tissues through absorption, scattering, and reflection[14] determine how far it can propagate through them and determine the efficacy of the light delivery. Absorption involves the uptake of light energy by tissue chromophores.[15] Scattering occurs due to the heterogeneous nature of tissues, causing light to deviate from its original path and affecting the resolution of optical imaging methods.[16] Reflection occurs due to the difference in refractive indices between tissues and their surrounding environments, causing a portion of the light to bounce back at the tissue boundaries.

Figure 1 [17] presents the distance at which light intensity drops to 10%, 1%, and 0.1% of the initial irradiance when it penetrates into brain tissue. The greatest penetration depth (Le ≈ 3.5–4.5 mm) is found within the 700–900 nm range, known as the "first near-infrared (NIR) window" or the "first therapeutic window".[18] Light-based processes activated by photons in this range can be excited at distances 100 times deeper than processes driven by UV light. However, this NIR window is not entirely transparent, with less than 0.1% of photons reaching beyond a few centimeters. Simply increasing the photon count to improve depth is problematic due to the risk of causing photothermal or photochemical damage to the tissue above.

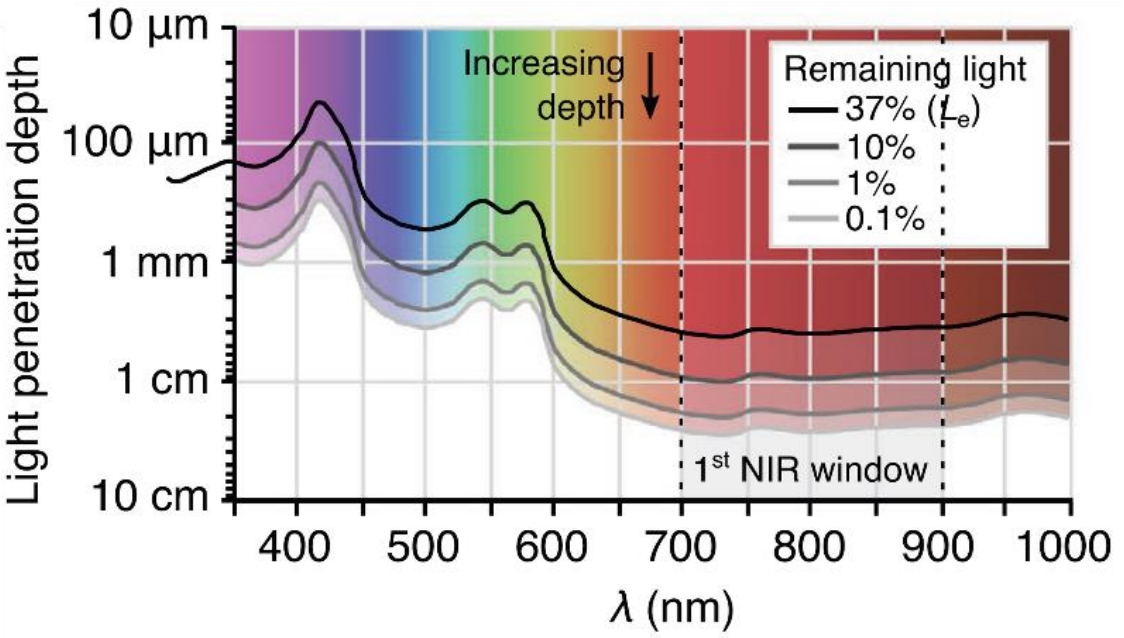

Figure 1. Penetration depth (Le) in brain tissue as a function of wavelength, defined as the depth at which irradiance falls to 1/e (≈37%) of its initial value. The data correspond to different levels of hemoglobin oxygenation (72% oxygen saturation, fully deoxygenated, and fully oxygenated conditions). Dashed lines indicate depths at which light intensity drops to 10%, 1%, and 0.1% of the incident value. Adapted with permission.[17]©2021. Advanced Functional Materials published by Wiley-VCH GmbH.

Implanting optical waveguides to deliver light to target locations within the body is one strategy to overcome the light penetration limitation. The most common optical waveguides are silica optical fibers (SOFs), which exhibit high optical transparency and low propagation loss ($\alpha = 0.2$ dB km^{-1} at 1550 nm).[19] However, unlike most tissues, SOFs are rigid (Young's Modulus E ≈ 70 GPa)[20] and brittle (elongation at break <1%)[21] and show low biocompatibility. Polymer optical fibers (POFs) are less rigid and flexible,[22] and show higher tissue compatibility. POFs are far less efficient waveguides than SOFs ($10^{-3}<\alpha<10$ dB cm^{-1}) from thermoplastics[19] to hydrogels[23] at visible wavelengths, but sufficient to guide light along typical distances in the body of therapeutic relevance (20-30 cm). In the following paragraphs, examples of application fields of POFs are summarized.

Sensors for Diagnostics: Fluorescent and luminescent probes like antibody-conjugated organic dyes for detecting proteins and biomarkers,[24] glucose [25] [26] or blood oxygen,[3b, 27] [3b] dye-linked nucleic acids for monitoring gene expression,[28] pH-sensitive fluorophores, or Förster

resonance energy transfer (FRET)-based sensors,[29] can be incorporated into implantable light-guiding hydrogels for in vivo monitoring of proteins, peptides, RNA, electrolytes, biomarkers, and toxic substances. For example, *P*oly(acrylamide-co-poly(ethylene glycol) diacrylate) hydrogel waveguides with an alginate hydrogel cladding layer functionalized with glucose-specific receptors were used to monitor glucose levels in porcine tissue by measuring the variation in light transmission through the hydrogel fibers.[30] In a similar manner, wearable devices can integrate sensing optical fibers woven into textiles to detect biomolecules of different kinds. [31]

Photodynamic therapy (PDT): PDT combines light and a photosensitizer[32] and is applied to treat cancer. In PDT, light of a specific wavelength excites the photosensitizer, which transfers energy to tissue oxygen, producing reactive oxygen species (ROS) like singlet oxygen and free radicals that are cytotoxic to cancer cells. PDT has received clinical approval for treating cancers such as skin, lungs, esophagus, bladder, ovarian, and brain cancers. For treating pancreatic cancer, an endoscopic ultrasound-guided PDT has been applied in clinical trials.[33] In this technique, a long optical fiber connected to a short cylindrical diffuser placed near the pancreas is used to excite the photosensitizer verteporfin. Light-emitting fabrics made from side-emitting optical fibers are used to treat skin conditions like actinic keratosis. These fabrics can be woven into wearable devices and provide uniform light distribution by emitting light at bending positions of the fibers. In a clinical trial, a PDT fabric integrated into a helmet was successfully used to treat actinic keratosis.[33c] Hydrogel microneedle arrays have also been applied to deliver light and photosensitizer transdermally.[34]

Photochemical tissue bonding (PTB): PTB is used to treat eye disorders such as keratoconus and corneal ectasia.[35] This clinical procedure uses riboflavin and light to activate photosensitizers and induce crosslinking in the collagen-rich corneal stroma, improving its mechanical properties and promoting collagen regeneration. A similar approach has been proposed for the treatment of myopia, with the idea of stiffening the sclera to prevent excessive eye growth during childhood. However, the challenge of delivering light to the scleral tissues around the eye remains. Flexible elastomer optical waveguides provide a solution for in situ equatorial sclera crosslinking. Silver-coated PU/PDMS waveguides efficiently delivered blue light to the equatorial sclera with minimal leakage which caused a 2-fold increase in scleral stiffness (Young's modulus) after treatment.[36]

Photobiomodulation (PBM): PBM uses low-intensity red or near-infrared light to relieve pain, promote healing, and reduce inflammation. While the precise mechanisms are still debated, it is

believed that light interacts with mitochondria and calcium ion channels, increasing adenosine triphosphate (ATP) production, ROS, and nitric oxide.[37] PBM has shown promise in applications such as pain management, wound healing, and treating traumatic brain injuries. Wearable devices using side-emitting polymer fibers have been developed for large-area PBM. [32, 38]

Photothermal therapy (PTT): PTT is a localized treatment that uses heat generated by photothermal agents to address medical conditions like cancer.[39] A photothermal agent is administered and directed to the target tumor site. Once the agent has accumulated in the tumor, near-infrared (NIR) light of high intensity is irradiated directly into the tumor.[40] The photothermal agent absorbs the light and converts it into heat, which destroys the tumor cells.[41] A recent innovation integrated photothermal agent administration, light delivery, and tissue sampling into a single multi-mode fiber (MMF)-based injectable optical system.[42] This system uses a modified syringe needle along with a conventional optical fiber. The needle guides the optical fiber into the tumor, where it delivers light to the targeted area. The space between the needle and the fiber is used to administer the photothermal agent and collect tissue samples for biopsy analysis.

Optogenetics: In optogenetics, light-sensitive ion channels allow the control of ion transport across cell membranes using visible light.[43] While optogenetics initially focused on brain research, it has expanded to other electrically active cells in the spinal cord,[44] heart,[45] and muscles.[46] Optical fibers have been employed for their ability to precisely deliver light deep into the brain, providing a versatile and minimally invasive solution to overcome challenges related to penetration depth, spatial accuracy, and targeted light delivery. Tapered optical fiber with tailored emission was demonstrated to enable both large-area and spatially restricted illumination, eliminating the need to move the implant for precise light control.[47] For larger illumination areas, implantable and biocompatible light-guiding hydrogels were developed by molding and photo-crosslinking of PEGDA (polyethylene glycol diacrylate).[48] Multifunctional optical fiber was fabricated featuring six electrodes made of graphite-loaded conductive polyethylene for neural signal transmission, two microfluidic channels for viral vector delivery, and a polycarbonate waveguide core for precise light delivery and stimulation.[49]

1.2. Fundamentals and classification of optical waveguides

Optical waveguides guide light efficiently over long distances with minimal loss. Waveguiding principles revolve around the confinement of light through total internal reflection (TIR),

facilitated by core-cladding structures where the RI of the core exceeds that of the cladding or surrounding medium. Key factors influencing waveguide performance include the refractive index contrast, core geometry, and material properties such as transparency. Mechanical flexibility is an additional requirement for introducing potential in biomedical applications. In the following sections, these concepts will be explained in more detail.

1.2.1. Absorbance and scattering properties

Optical loss, also referred to as optical attenuation, describes the reduction in light power or signal strength as it propagates through a waveguide, which is typically measured in decibels per centimeter (dB cm^{-1}). Optical loss in these materials can be divided into two primary categories: intrinsic loss and extrinsic loss.[50] Both mechanisms are influenced by the inherent material properties and the structure of the waveguide.

Intrinsic optical loss is associated with the material's inherent absorption and scattering properties. This loss can arise from several phenomena:

Absorption due to electronic transitions: Molecules of the material can absorb photons in the ultraviolet (UV) and visible light ranges, leading to electron excitation from the ground state to higher energy states. For example, electronic transitions such as $\pi \rightarrow \pi^*$ or $n \rightarrow \pi^*$ transitions occur in organic compounds, particularly in those with highly conjugated systems, such as carbon-carbon (>C=C<) or carbon-oxygen (>C=O) double bonds.[51] These transitions are primarily active in the UV range but can also extend into the visible spectrum, thereby affecting the light transmission efficiency in optical waveguides.

Absorption due to molecular vibrations: In the near-infrared (NIR) range, molecular vibration absorption becomes a dominant mechanism. This type of absorption occurs when the frequency of the incoming light matches the vibrational frequencies of molecular bonds, such as stretching and bending vibrations. Harmonics or overtones of these vibrations further enhance the absorption, leading to light attenuation. These vibrational absorptions are particularly significant in polymeric biomaterials, where large, flexible molecules exhibit diverse vibrational modes.[50]

Light scattering (Rayleigh and Mie scattering): Scattering within the material also contributes to intrinsic optical loss. Rayleigh scattering occurs when the inhomogeneities in the material are much smaller than the wavelength of light. Since Rayleigh scattering scales with the inverse fourth power of wavelength (λ^{-4}), shorter wavelengths are scattered more intensely than longer wavelengths. This scattering is independent of the material's specific chemical composition and arises from microscopic density fluctuations or compositional variation.[52]

Mie scattering, on the other hand, occurs when the size of the inhomogeneities is comparable to the wavelength of the light. In polymeric waveguides, Mie scattering can be several orders of magnitude stronger than Rayleigh scattering due to the inherent structural heterogeneity of the polymer network. Long polymer chains and macromolecular pores introduce irregularities on a nanometer to micrometer scale, which increases the scattering of light and thus elevates optical loss.

Extrinsic loss is primarily introduced during the manufacturing process or due to environmental contamination. It arises from defects such as surface roughness, structural imperfections, and the inclusion of impurities like dust particles, bubbles, and insoluble substances. These external factors cause additional scattering and absorption, further reducing the efficiency of the optical waveguide.

The total scattering in polymer-based optical waveguides can be described by the following empirical model[52b]:

$$\propto_{scatter} = A + \frac{B}{\lambda^2} + \frac{C}{\lambda^4} \qquad (1.1)$$

where A represents scattering due to large inclusions (>> λ), B corresponds to scattering from inhomogeneities with dimensions on the order of the wavelength (Mie scattering), D accounts for scattering from atomic-scale inhomogeneities (Rayleigh scattering), and λ is the wavelength of the propagating light. This equation provides insight into how different sources of scattering contribute to the overall optical loss, with shorter wavelengths being more prone to Rayleigh scattering and large inclusions dominating Mie scattering losses.

1.2.2. Refractive Index

The Refractive index (RI) of a material is another factor that measures how much light, or any other electromagnetic wave slows down as it passes through a medium. It is defined as the ratio of the speed of light in a vacuum to the speed of light in the medium. The refractive index of a material is influenced by its packing density (free volume), polarizability, and the difference between the optical wavelength used and the material's maximum absorption wavelength.[52b, 53] At optical frequencies, only electronic polarization occurs, making it the dominant contributor to the refractive index. Aromatic polymers have higher refractive indices than aliphatic ones due to better packing and higher electronic polarizability. Polymers with π-conjugated structures, like

those containing aromatic groups or dyes, also exhibit higher refractive indices. High-temperature densification further increases the refractive index by reducing free volume. Fluorine substitution affects the refractive index in three ways: increasing free volume (which lowers refractive index), reducing electronic polarizability of C-F bonds, and blue-shifting the absorption wavelength (which also lowers the refractive index. The RI of polymeric hydrogels range from 1.33 for PEG-based polymers t to 1.7 for silk-based waveguides.[1]

1.2.3. The principle of Total Internal Reflection (TIR)

When light travels from a medium with a higher refractive index (n_1) to a medium with a lower refractive index (n_2), it bends away from the normal direction (reflection). The Snell's Law describes this behavior and relates the angles of incidence and refraction to the RIs of the two media:[54]

$$n_1 \sin\theta_1 = n_2 \sin\theta_2 \quad (1.2)$$

where n_1 and n_2 are the RIs of the first and second media, θ_1 is the angle of incidence and θ_2 represents the angle of refraction. As the angle of incidence (θ_1) increases, the angle of refraction (θ_2) also increases.

For light to propagate along an optical waveguide, the RI of the waveguide needs to be higher than the RI of the surrounding medium. The RIs of the fiber and the medium define the numerical aperture (NA) as:[55]

$$NA = \sqrt{n_1^2 - n_2^2} \quad (1.3)$$

A large NA means that a wider range of incident angles, relative to the fiber axis, can undergo total internal reflection (TIR) within the waveguide. This allows the waveguide to capture and guide light more efficiently, as it can accept light from broader angles. The maximum incident angle which can undergo TIR (θ_{NA}) is defined by:

$$\theta_{NA} = Arc\sin\frac{NA}{n_1} \quad (1.4)$$

Alternatively, the critical angle of incidence (θ_C) can be defined $\theta_C = 90° - \theta_{NA}$ at which total internal reflection (TIR) happens. If the angle of incidence exceeds the critical angle ($\theta_1 > \theta_c$), light cannot pass to the second medium. Instead, it is entirely reflected in the first medium. For implanted waveguides, the surrounding medium is biological tissue, with refractive index values ranging from 1.33 to 1.56, depending on the type of tissue.[56] In most cases, optical fibers with

a core-cladding structure, where the core's refractive index is higher than that of the cladding, are used to maintain a large difference in the refractive index and achieve TIR.

1.2.4. Classification of optical waveguides

Depending on the refractive index profile across the waveguide, there are two primary types: step-index waveguides, where the RI change at the core-cladding boundary is abrupt, and graded-index waveguides, where the RI gradually decreases from the core to the cladding.[57]

Waveguides can support either single-mode or multimode propagation, depending on the wavelength of the light and the dimensions of the core. Single-mode waveguides have small core diameters and only support the fundamental mode, which propagates with minimal interaction with the cladding, reducing optical losses. Multimode waveguides, with larger core diameters, support multiple modes of light propagation. These modes often interact with the waveguide's cladding, increasing scattering and absorption, and consequently, higher optical losses occur.[58]

In tapered waveguides, the core dimensions decrease along the propagation direction, and therefore fewer modes are supported as the core narrows. This effect is exploited in certain applications, like side emission, where light is gradually emitted from the waveguide as the number of supported modes decreases.[59]

Waveguides can also exist in various geometries. Non-planar waveguides exist in the form of optical fibers[60] channel waveguides, rib waveguides, and ridge waveguides.[61] Planar waveguides, also known as slab waveguides[3b], consists of a flat, thin guiding layer.

Attending to the material, optical waveguides can be classified as glass, polymer (and hydrogel) or semiconductor waveguides.

1.2.5. Optical loss, attenuation and propagation length

The performance of an optical waveguide is quantified by its optical loss, also referred to as attenuation. The optical loss represents the reduction in light power as light travels along the waveguide. The optical loss (A) at a given distance (L) is calculated by the ratio of the transmitted light intensity (I) at that distance from the initial input intensity (I_0) as:[62]

$$A = 10\ log\frac{I_0}{I} \qquad (1.5)$$

The optical loss is measured in decibels (dB). An optical loss of 1 dB means the output intensity *(I)* has decreased to approximately 79% of the input light intensity (I_0). To quantify the decay of light per unit length of a waveguide, the attenuation coefficient (α) is used, which represents the optical loss in centimeter distance, expressed in dB cm^{-1} and defined by:

$$\propto = \frac{A}{L} \qquad (1.6)$$

The Propagation Length (Le) is the distance over which the light intensity (*I*) decays to a fraction of 1/e (approximately 0.37) of its original value (I_0). It provides a more intuitive measure of optical loss, particularly when comparing it to the penetration depth of light in tissue.[17] Silica-based optical fibers, widely used in telecommunications, exhibit very low attenuation (α = 0.2 dB km^{-1} at 1550 nm). Polymer-based waveguides exhibit higher attenuation, i.e. poly (methyl methacrylate) fibers show attenuation values of 0.15 dB m^{-1} and polycarbonate fibers 1 dB m^{-1} at visible wavelengths. In biomedical waveguides, attenuation values around 1 dB cm^{-1} are common, which corresponds to effective propagation lengths (Le) of approximately 4 cm.

1.2.6. Mechanical properties and biocompatibility of optical waveguides

Implantable waveguides need to be biocompatible and, therefore, their mechanical properties should closely resemble those of the surrounding tissue. The mechanical properties of reported implanted waveguide materials vary widely, as shown in **Figure 2**.

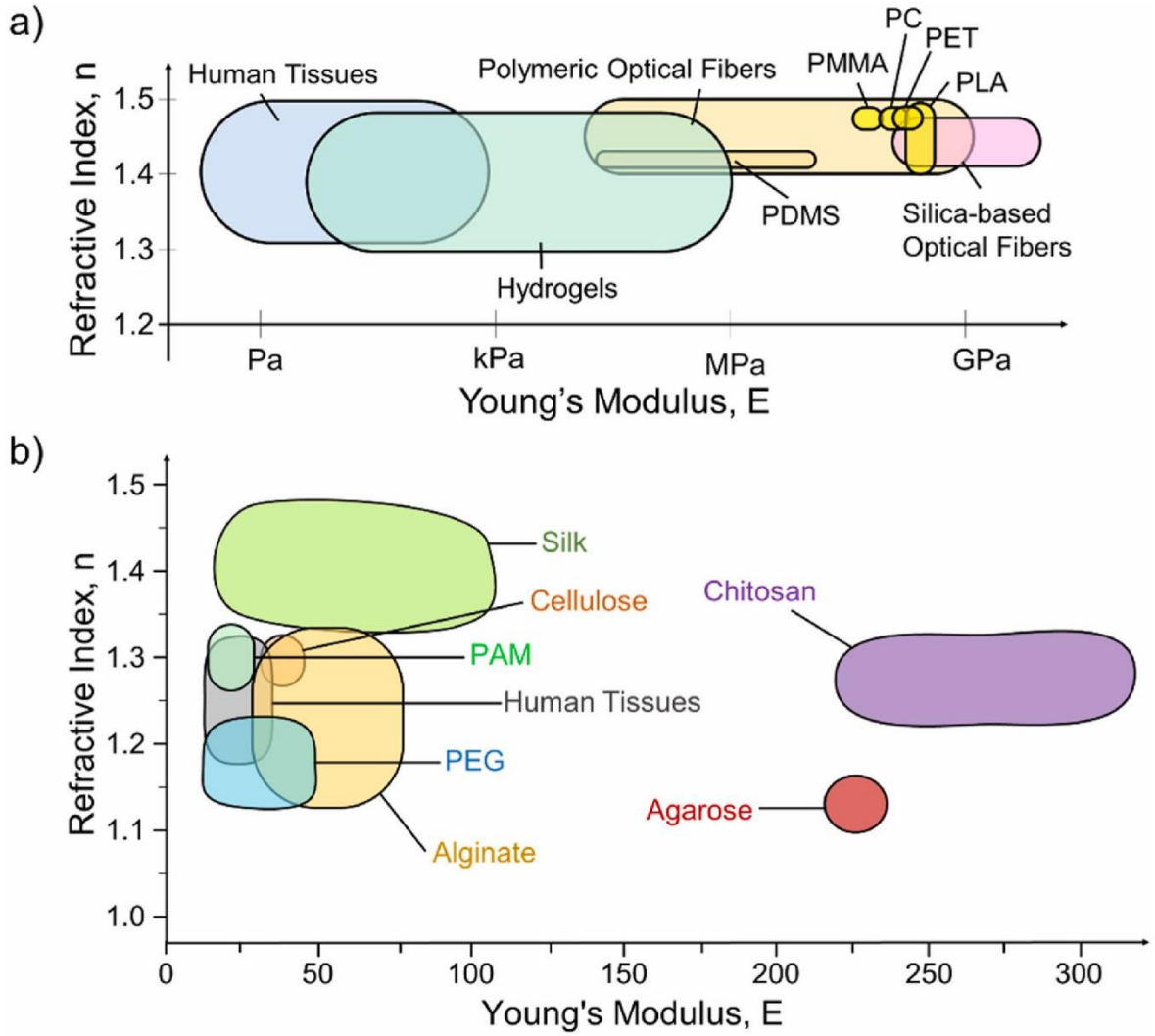

Figure 2. A comparison of the optical properties across the mechanical properties for a) biomedical waveguides and b) hydrogels. Reprinted with permission from [1] Copyright 2024 Bioactive Materials.

Silica waveguides are at the upper end of the stiffness spectrum with a Young's Modulus around 70 GPa[20] and an elongation at break < 1%.[63] Polymer-based materials, such as polymethyl methacrylate (PMMA) [64] and polyesters like poly(L-lactide) (PLLA),[65] have been developed to provide optical transparency with enhanced biocompatibility and mechanical properties. However, polymer optical fibers (POFs) still exhibit a significantly higher Young's Modulus (1 MPa–10 GPa) compared to soft human tissues, which are around 10 kPa.[66] [67] Natural polymers like regenerated silk fibroin hydrogels have mechanical properties similar to cartilage, skin, and the eye's lens, with a tunable modulus ranging from 0.07 to 6.5 MPa, comparable to soft tissues.[68] For softer and more stretchable waveguides, elastomers derived from polyurethanes,[36] polysiloxanes,[69] or citrate-based polyesters have been used.[70]

Polydimethylsiloxane (PDMS) is commonly used due to its good biocompatibility, ability to be molded at sub-micron scales, oxygen permeability, and chemical inertness.[71] PDMS's high optical transparency across the visible spectrum makes it an attractive option for stretchable waveguides.[72] Tailoring the crosslinking density of PDMS allows for core-cladding waveguide designs with customizable refractive indices.[73]

Hydrogel-based waveguides represent softer alternatives with mechanical properties close to soft tissues (E < 1 kPa to 5 MPa).[1, 66] These hydrogels can be formed through either chemical or physical crosslinking. More complex network architectures like interpenetrating polymer networks (IPNs) can enhance hydrogels' strength, extensibility, and toughness without drastically increasing stiffness, making hydrogels an appealing choice for soft tissue-compatible waveguides.

1.3. Fabrication of polymeric waveguides

This section describes fabrication methods to process polymeric materials into optical waveguides with fiber geometry. These optical fibers are typically fabricated by thermal drawing, extrusion, or molding.

Thermal drawing is used to fabricate optical fibers from thermoplastic polymers. The process starts from a fiber preform, which is a larger-scale version of the desired fiber with typically more than 100 times the final diameter. This preform is heated at temperatures above the glass transition temperature (Tg), when it becomes soft and pliable, and is drawn to a thin fiber. The resulting fibers have diameters of hundreds of microns and can be drawn to diameters below tens of microns through a second drawing step. Once the desired dimensions are reached, the fiber is cooled below Tg to solidify in its final shape. Thermal drawing offers scalability and continuous processing, allowing the production of thousands of meters of fibers. Controlled heating and precise drawing conditions are essential to achieve fibers with constant dimensions and optical properties. It is also possible to integrate additional functionalities in the cladding of the fiber by using fiber preforms with a multilayer structure.[2a, 74] Thermal drawing is also applied to fabricate silica fibers.[47, 59, 75]

Molding involves filling a precursor solution of the optical material into a mold with the desired dimensions of the waveguide and allowing it to react and solidify. The material is cured typically using heat or UV light and solidifies into the shape of the mold. Thermoplastic materials can also be molded into fibers. Molding allows to produce waveguides with alternative geometries, like films. Molding has been utilized to create rigid waveguides from materials such as silk[76],

poly(L-lactic acid) (PLLA),[61] and elastomers like PDMS,[77] polyurethane (PU),[36] and citrate-containing polyesters.[70] It has also been used to produce hydrogel-based waveguides from materials such as polyethylene glycol diacrylate (PEGDA),[48] polyacrylamide (PAM), agarose, and silk.[76] However, molding is inherently a batch process and is limited to single-material structures. For more complex core-cladding waveguide designs, sequential molding steps are required,[76] which can be time-consuming and labor-intensive. After molding, the waveguides need to be removed from the mold, which, in the case of hydrogel-based optical fibers, is often done by swelling the silicone mold in organic solvents and applying water pressure to eject the waveguide. These additional steps, especially when using organic solvents, are significant drawbacks of the molding process and, therefore, are not ideal for manufacturing.

Extrusion is another fabrication method that offers to create more intricate structures, such as multilayer fibers and non-cylindrical shapes. Compared to drawing, extrusion allows for greater design complexity while being simpler and more scalable than the molding process. In a fabrication process by extrusion, the precursor optical polymer is forced to flow through an extrusion head to produce fibers with a specific cross-sectional profile. This is possible starting from either a thermoplastic polymer that is processed above the flow temperature and cooled right after the extrusion head, or from a reactive precursor mixture that crosslinks after the extrusion process. Extrusion allows for the continuous production of fibers. Fibers with core-cladding structures are possible by using coaxial extrusion heads. Extrusion can be applied to a variety of meltable, chemically, or physically curable materials, as long as the waveguide's structural integrity is quickly achieved post-extrusion. This is typically done through cooling below the glass transition temperature (Tg) or through rapid crosslinking. For example, extrusion has been employed to create complex pre-forms, such as oversized hollow-channel pre-forms made from resorbable glasses, which are later thermally drawn to form the final waveguide structure.[78] Extruded optical fibers can be coated with a different material by dip coating. In this process, the fiber passes through a solution of the coating material and is withdrawn from the bath at a controlled speed. As the fiber is pulled out, a thin layer of the solution adheres to its surface.[79] The coated fiber is allowed to dry to form a uniform layer around the fiber core. This method is beneficial for adding functional coatings to improve the optical properties of waveguiding fibers. It also overcomes the low throughput of molding techniques.

Extrusion has been applied to fabricate optical waveguides from biomaterials. Feng J. et al. fabricated waveguides from the degradable thermoplastic polyesters PLA and PLA-co-PCL using an extrusion head coupled to a bioprinter at temperature ranges of 90-100 °C.[80] The

printed fibers transmitted 400–808 nm light, even along bent shapes. Optical losses ranged from 0.02–0.26 dB cm^{-1} in air and 0.14–0.73 dB cm^{-1} in tissue at wavelengths of 405–520 nm. In a further study, extrusion-based processing combined with in situ photopolymerization was applied to fabricate hydrogel-based optical waveguides. These waveguides had a core of PEGDA-DTT and a cladding of acrylated Pluronic (PluDA). The step-index fibers were printed with varying core diameters (340 to 640 µm) and a fixed outer diameter of 1.02 mm. Continuous lengths of up to 50 cm were achieved, with optical losses of 0.1 dB cm^{-1} at 520 nm, 0.4 dB cm^{-1} at 405 nm in air, and 0.25–0.7 dB cm^{-1} in tissue. These waveguides demonstrated light delivery for activating optogenetic switches and controlling cell adhesion and migration in a photo-responsive 3D fibroblast culture.[81] In a subsequent study, core-cladding PDMS waveguides were extruded and cured in situ through photo-crosslinking.[60] The fibers showed optical loss values ranging from 0.13 to 0.34 dB cm^{-1} in air and tissue across the 405–520 nm wavelength spectrum. Core-cladded fibers, with PluDA as the cladding, displayed a Young's Modulus of 150 kPa and demonstrated elasticity, allowing them to be stretched to over five times their original length.

Naturally derived spider silk has been used to fabricate optical waveguides through direct ink writing of an aqueous silk fibroin solution, as demonstrated by S. Parker et al. The extruded silk waveguides, printed on borosilicate glass slides in both straight and wavy configurations, had lengths of several centimeters and a diameter of about 5 µm, but could not be removed from the glass substrate.[82] These waveguides exhibited an attenuation of approximately 0.25 dB cm^{-1} at 633 nm.

H. Orelma et al. used a wet-jet spinning method to fabricate cellulose-based optical fibers, with a core made from cellulose dissolved in [EMIM] AcO and a cellulose acetate cladding. After spinning, filaments were soaked in water for two hours, dried at room temperature, then coated with cladding, followed by solvent evaporation at room temperature. The fibers, with a diameter of 210 µm and cladding thickness of 3.40 ± 0.20 µm, showed a minimum attenuation of 5.9 dB cm^{-1} at 1130 nm, with optical losses below 10 dB cm^{-1} in the 750–1350 nm range.[83]

1.4. Fiber Fabrication by Multimaterial Extrusion Printing

In a classical fabrication process, complexity in material properties or functions is achieved by assembling material elements of different compositions. In a multimaterial fabrication approach, different materials or material properties are combined in a single fabrication process to create objects that inherently integrate parts of different compositions and functionality, without the

need for assembly steps. Multimaterial structures enable the integration of multiple properties across space and scales and reduces problems associated with connecting individual materials or elements in a functional device. They extend the design scope of materials by allowing alterations of the material properties across a single object and thus tailoring the local material properties to the particular functional requirements.

Different fabrication approaches have been employed to create fibers with multiple components, properties and functionalities. **Figure 3** illustrates various multimaterial fabrication techniques, including thermal drawing (A), coaxial extrusion printing (B), and segmented fiber production via multimaterial printing (C). In this section, methodologies and material combinations used for printing multimaterial fibers are described. This description is not limited to polymeric optical fiber applications, it also includes methodologies that have the potential to be applied to the fabrication of multimaterial optical fibers.

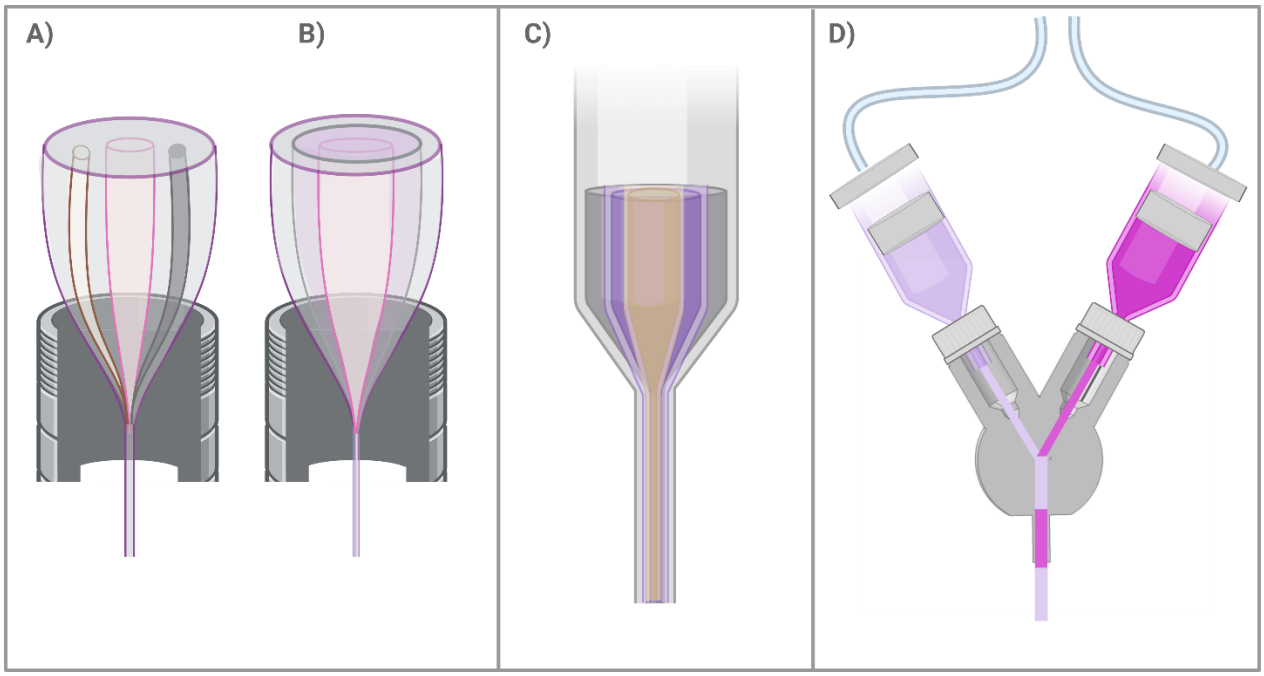

Figure 3. Schematic representation of different multimaterial fabrication methods. A) Multimaterial thermal drawing, B) Coaxial extrusion printing of multimaterial fibers, and C) Segmented fibers produced via multimaterial printing.

1.4.1. Multimaterial thermal drawing of fibers

Leber and their colleagues[84] explored thermal drawing to fabricate multi-material fibers for soft robotics. This technique is adapted to integrate a variety of materials into a single fiber while maintaining the intricate cross-sectional designs from the macroscopic preform through to the microscale fiber. The process involves co-drawing multiple materials, which are assembled in the preform stage, to create fibers with complex internal architectures. The materials employed include thermoplastic polycarbonate (PC) with high elastic modulus and softer thermoplastic elastomers poly(styrene-b-(ethylene-co-butylene)-b-styrene) (SEBS) and Geniomer. The thermo-processable inks showed high viscosity to sustain integrity during thermal drawing. Optical waveguides, metallic wires, and microfluidic channels were integrated within fibers of 700 µm in diameter. The fabrication process starts with the creation of a detailed preform that includes all desired materials and structural features by compression molding. This preform is then thermally drawn, where it is heated and stretched to form long fibers that preserve the designed microstructures at a reduced scale. The fibers are equipped with functionalities that support various robotic movements and sensing capabilities, driven by embedded tendons and controlled by an external mechanism. These fibers find their application in soft robotics, particularly in minimally invasive medical procedures. However, this technique limits the choice of materials to those that have similar rheological properties and can withstand the thermal and mechanical stresses of the process without degrading or losing their optical properties.

Multimodal optical fibers were fabricated using thermal drawing, which enabled the creation of fibers with diameters ranging from 70 to 700 µm.[49b] The multimaterial preform included polycarbonate (PC), cyclic olefin copolymer, conductive polyethylene (CPE), and tin (Sn). Low-loss optical waveguides integrated with neural recording electrodes in polymer-based fiber probes were achieved and enabled optical stimulation and neural recording as well as drug delivery in freely moving mice.

1.4.2. Coaxial extrusion printing of multimaterial fibers

Multi-material coaxial printing enables the simultaneous extrusion of fibers containing

different materials through a single nozzle. With a coaxial nozzle setup, materials with various properties can be aligned and deposited in a concentric configuration as part of a single fiber.

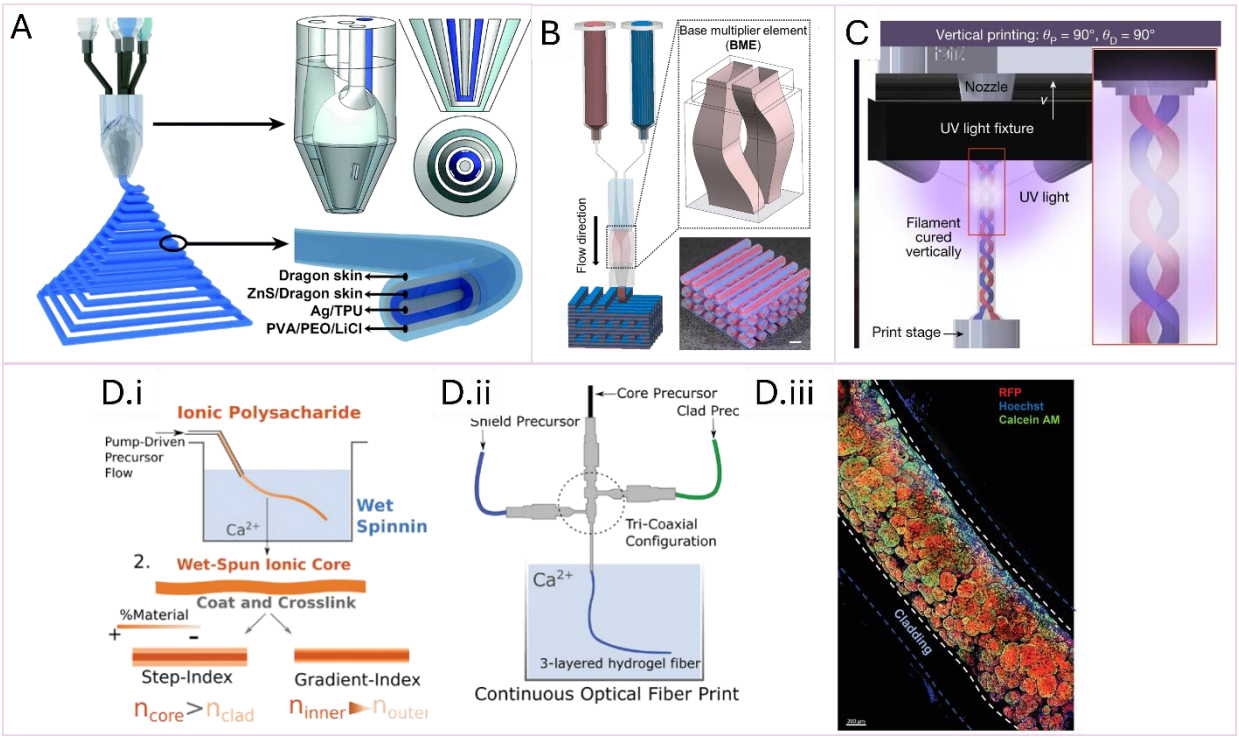

Figure 4. Multimaterial coaxial extrusion printed fibers. A) Multicore-shell printheads and 1D stretchable alternating electroluminescent devices.[85] B) Schematic of the printing system and modular extruder head for 3D architectures. Reprinted from [86] Copyright (2024), with permission from Elsevier. C) Configurations of printing setup for rotational core-cladding structures.Reproduced with permission from[7] 2023. © Springer Nature. D) i. Wet-spinning approach for continuous optical fiber core fabrication with customizable hydrogel coatings for core-cladding architectures. ii. Tri-coaxial nozzle for optical fiber printing. iii) Microscopy image of a fully developed fiber core, scale bar: 200 µm. Printed with permission from[87]. © 2021 Wiley-VCH GmbH.

Liu and colleagues [85] (**Figure 4A**) reported a printhead with a 4-layer tapered coaxial nozzle with an inner core of 200 µm diameter and three cladding layers of 200 µm thickness. The extruded fiber had an Ag/thermoplastic polyurethane conductive core, a first cladding layer of reactive silicone containing ZnS particles with adjustable emission colors, a third conductive layer containing polyvinyl alcohol (PVA), polyethylene oxide (PEO), and lithium chloride (LiCl), and an additional encapsulating layer of the reactive silicone. The formulated inks exhibit shear-thinning properties and sufficient yield stress to maintain the coaxial fiber shape post-extrusion. Electroluminescent fibers that emitted light in multiple colors with high stretchability of up to 450% were obtained.

Ren and coworkers [88] (**Figure 4B**) used modular extruder heads connected in series or in parallel to integrate multiple materials into filament structures with controlled layering and patterns. The number of coaxial layers in each filament is controlled by the design of the nozzle. The study explores using two immiscible materials with similar rheological properties (soft/hard PDMS by varying ratios and epoxy/silicone). Differing mechanical properties for co-extrusion create structures like lamellar elastomer composites and bio-inspired nacre-like architectures. Using a modular printhead allows for creating multiple layers in a filament, ranging from 4 to 128 layers, with layer thickness from 250 to 8 µm, respectively. After printing, the elastomer composites and silicone/epoxy composites were thermally cured.

In a different study, a rotational multimaterial 3D printing method was applied to coaxially extrude multiple materials [7] (**Figure 4C**). This approach combines multi-material extrusion with controlled rotation to create helical filaments with programmable geometries. The fabrication process involved the extrusion of different inks through a rotating nozzle, creating a helical structure within the fibers. The transparent ink was PDMS based, and the dielectric elastomer components were composed of a soft and stiff urethane acrylic ink with carbon black (CB) additive for conductivity. Filaments were cured in situ during the printing process using UV light. The resolution of the printing process was enhanced by the control over the nozzle's rotational rate and allowed subvoxel adjustments to the material layout within the fibers. The printed fibers had core diameters from 250 to 700 µm, and filament diameters from 2.5 to 5 mm. Authors printed artificial muscles consisting of helical dielectric elastomer actuators, featuring individually controllable conductive helical channels embedded within a dielectric elastomer matrix.

Multilayer optical waveguides were fabricated by Guimarães and coworkers [87] (**Figure 4D**) by wet spinning and extrusion of ionic-crosslinked natural polysaccharides. They used alginate 7 % with RI ≈ 1.34 as well as gold nanoparticles in the core and Gelangum with RI 1.33 in the cladding which resulted in core-cladding optical fibers with ≈ 1.5 mm diameter. In the first part of the work, they encapsulated protein-G-coupled AuNPs within the fiber core and used them for sensing. In the next step, A coaxial 3D printing nozzle was employed for the continuous fabrication of living optical fibers, enabling precise integration of biological materials. The fibers with cancer cells encapsulated in alginate cladded with two layers of Gelangum were extruded in an ionic bath to crosslink. The fibers have a final diameter of ≈1.5 mm and allow light interaction with living cells, facilitating the quantification and digitalization of complex biological phenomena, such as 3D cancer progression and drug susceptibility.

1.4.3. Segmented fibers by Multi-material Fabrication

The ability to use a single nozzle to print fibers with alternating composition along the axis creates new possibilities for fabricating fibers with customized compositional and property gradients.

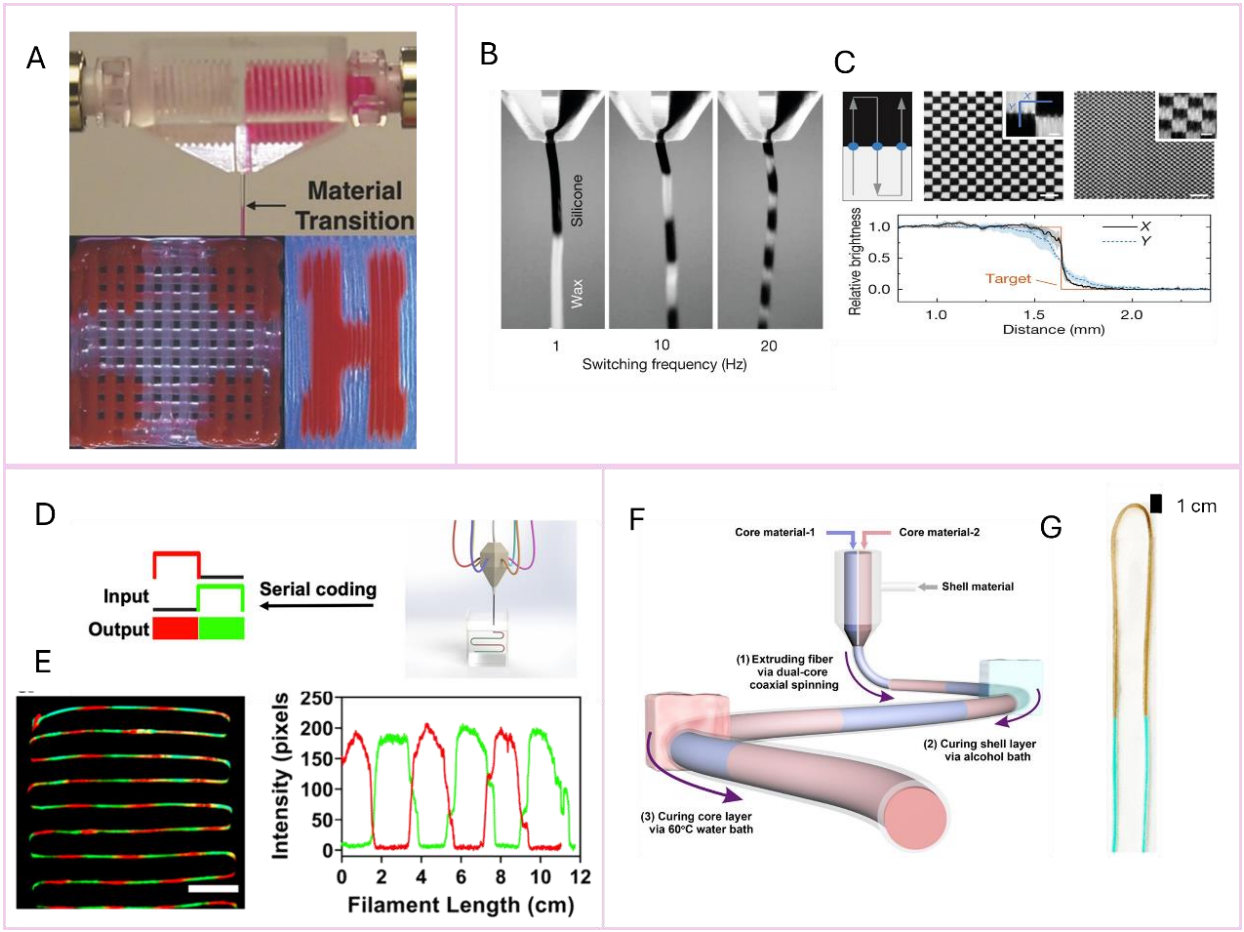

Figure 5. Segmented fibers via multimaterial printing A) Multimaterial microfluidic printhead with printed structures.[11] B) Continuous voxelated filament from a two-material nozzle with varying switching frequencies. C) Checkerboard patterns of silicone and wax from an 8 × 1 MM3D printhead with parallel material transitions.[9a] D) Schematic of ink switching capabilities using a single nozzle printhead. E) Prints and intensity profiles of red-to-green switching in linear modes. scale bar: 1.5 cm. Reprinted with permission from [5]. Copyright 2022 American Chemical Society. F) Core–shell segmented fibers fabricated via dual-core coaxial spinning with shell curing in an alcohol bath and core curing in a 60°C water bath. G) Thermochromic elastomer/conductive hydrogel fibers as wearable strain sensors for respiratory monitoring. scale bar: 1 cm. Reprinted (adapted) with permission from [89]. Copyright 2020 American Chemical Society.

Hardin et al. (**Figure 5A**) used a microfluidic printhead that switched between two viscoelastic materials to print in 1D, 2D, and 3D architectures.[11] PDMS inks are pushed through two channels (200 µm) into a microfluidic junction (200 µm expanded to 400 µm) by two opposed syringe pumps, which facilitate rapid switching between inks. Key to the system's effectiveness is the design of the junction and expansion sections to minimize the transition volume and sharpen the interfaces between materials in the printed filaments. The system allowed a minimum transition length of 520 µm at flow rates of 1600 µL min^{-1}. Filaments with segments of alternating composition were printed. In follow-up work, the printing resolution was improved [9a] (**Figure 5B,C**) by using a mixing nozzle with a shorter dead zone and a pneumatic pressure controller that processed up to eight different inks through bifurcating channel networks that converged at a junction just before the nozzle outlet (≈ 200 µm). The system allowed for continuous printing with controlled variability in material composition along the printed filament with a resolution of 250 µm, different silicone and epoxy inks with different mechanical properties were printed into objects with spatially tailored mechanical properties. For precise deposition, inks with yield stress between 150 to 500 Pa and shear thinning behavior were required. The printhead deposited materials in a voxel-by-voxel manner, where the composition of each voxel was varied by changing the material flow through solenoid-actuated valves. At the points where materials switched, a transition zone of 320 micrometers in length was observed at a switching frequency of 60 Hz. This nozzle design was further used in other studies for different applications like food processing.[90] The study investigates a continuous switching 3D printing method for food using a dual-channel extrusion nozzle, focusing on surimi paste with varying moisture contents. The extrusion was performed with a dual-channel nozzle diameter of 1 mm which allowed switching between pastes, achieving a resolution of 2 mm in deposition. Hassan and coworkers[5] (**Figure 5D,E**) implemented a computer-controlled pneumatic pressure controller paired with a microfluidics-based single nozzle printhead. This setup allowed for laminar flow-based voxelation using up to seven different hydrogel-based bioinks. The inks consisted of gelatin methacryloyl (GelMA), alginate—valued for its shear-thinning properties—and cellulose nanofibrils. These were printed in a supporting bath of agarose or gelatin with calcium chloride, which acted as a temporary scaffold and stabilized the ink during printing. The alginate ink crosslinked upon contact with calcium chloride and the GelMA was stabilized by a UV curing step after printing. The inks merged at a junction just before being extruded through a 330 µm nozzle, which had integrated pressure valves to prevent backflow. This allowed control over the material composition and physical properties of the extruded filament by toggling the pressure between the inks. Fiber diameters between 300 and 500 µm were obtained using

pressures between 3 to 7 psi (i.e. 20.7 to 48.3 kPa). A long transition zone of 6 to 1.8 cm was obtained between the printed segments of different materials at a print speed of 1400 mm min^{-1} and switching frequencies of 2.6 to 5.2 Hz.

In another insightful study, researchers[89] (**Figure 5F,G**) have developed a dual-core coaxial wet spinning method to extrude fibers with a segmented core with alternating segments of a conductive hydrogel or thermochromic elastomer and a shell formed by a thermoplastic polymer. The conductive hydrogel was polyacrylamide mixed with graphene oxide and the thermochromic elastomer was silicon rubber with thermochromic microcapsules that change colour with temperature. The polystyrene-block-polyisoprene-block-polystyrene shell allowed for maintaining structural integrity by protecting the core from environmental and mechanical damage and providing electrical insulation. For extrusion, a dual-core coaxial stainless-steel needle (14G) with two inner needles (22G) was used. The shell was cured by immersion in an alcohol bath. The core material was polymerized by thermo-initiated radical polymerization by immersing the fiber in a water bath at 60°C. The fiber dimensions were tuned by adjusting the flow rates during extrusion. Fibers with core/shell thickness of 192/796 µm and 96/1010 µm with alternating segments (≥ 5 cm) were fabricated. These fibers have potential as sensors for wearable sensor materials and technologies.

In this study, we implemented a multimaterial extrusion printing technique to fabricate soft optical fibers with customizable side-emitting segments. To control the side emission, it is essential to distribute scattering elements precisely along the fiber, necessitating accurate deposition of the scattering ink. Inspired by the ability to switch between multiple elastomeric inks, we designed a Y-shaped nozzle. The goal is to achieve a continuous and reliable process for producing soft fibers that allow the deposition of scattering elements with variable and controllable sizes (≥ 400 µm). By alternating between a waveguiding ink and a scattering particle-infused ink, we created optical fibers with adjustable waveguiding and side-emitting properties. This approach enables precise control of the emission profile along the fiber in a single, continuous printing process. The resulting hydrogel optical fibers, with their tailored illumination patterns, hold promise for applications such as activating photophysical processes in biomaterials or tissues.

Table 1. Multimaterial fabrication approaches.

Design	Fabrication method	Material	Geometry	Applications	Ref.
Coaxial multimaterial extrusion	DIW, Single nozzle with multiple layers	Core: Ag/PU,shell 1: ZnS/DS Shell 2: PVA/PEO/LiCl Shell 3: DS	200 µm for each layer	Stretchable electroluminescent fibers	[85]
Coaxial multimaterial extrusion	DIW, Single modular printhead	Soft/hard PDMS, commercial silicone, and epoxy mixtures	1 mm × 1 mm filaments, 4-128 layers, layer thickness 250-8 µm	Lamellar composite filaments and printed woodpile structures	[88]
Coaxial multimaterial extrusion	DIW, rotational nozzle with multiple cores	PDMS, urethane acrylate oligomer + CB for conductivity	2.5 - 5 mm filaments with 0.25 - 0.7 mm core strands	Functional artificial muscles	[7]
Coaxial multimaterial extrusion	Triaxial wet-spinning setup followed by crosslinking in $CaCl_2$ bath	Alginate + Gellan gum + cells + AuNrs	Core-cladding optical fibers with ≈ 1.5 mm diameter	Sensing, light interaction with living cells	[87]
Multimaterial thermal drawing	Thermal drawing	PC, SEBS, and Geniomer	700 µm	Soft robotic fibers	[84]
Multimaterial thermal drawing	Thermal drawing	PC, cyclic olefin copolymer, CPE, Sn.	70 – 700 µm	optical stimulation and neural recording as well as drug delivery	[49b]

Segmented fiber printing	3D printing, Single microfluidic printhead	PDMS + pigments	≈ 420 µm filaments with a transition length of 520 µm at Qp = 1600 µL min -1 between inks	Multimaterial printing	[11]
Segmented fiber printing	DIW, single nozzle with 4 junctions	Silicone/epoxy/wax	Filament diameter ≈250 µm With a 320 µm transition length at a switching frequency of ≈ 60 Hz	Miura origami pattern and a millipede-like soft robot	[9a]
Segmented fiber printing	DIW, microfluidic nozzle	GelMA/Alginate/Cellulose	Filament diameter between 300 to 500 µm with a transition 1.8 cm length at a switching frequency of ≈ 5.2 Hz	Living tissue constructs	[5]
Segmented fiber printing	Extrusion, Multicore-cladding nozzle followed by 2-step curing	Core: PAM/GO/silicon Shell: Polystyrol-block-polyisopren	Core/shell thickness: 192/796 µm, 96/1010 µm alternating segments ≥ 5cm	Wearable sensors	[89]

1.5. Strategies to achieve side-emission in polymeric optical waveguides

End-emitting optical fibers [81] are designed for scenarios requiring local lighting at a specific point at the fiber's end.[91] In contrast, side-emitting optical fibers are designed to emit light along the fiber and illuminate larger volumes than end-point optical fibers. Side-emitting waveguides are interesting for architectural lighting[92], automotive displays[93], inhibition of biofilm growth on surfaces[94] and for biomedical contexts, including photodynamic therapies[95] or optogenetics.[96] To outcouple light along the fiber length, these fibers incorporate light-scattering elements in their core or have cladding layers or geometries. The following sections describe different fiber designs for side emission and present literature examples with a focus on the materials and the method used for their fabrication. While this description focuses on polymeric optical fibers, a few examples with other materials or geometries are also shown in cases where the design or the methodology could also be transferred to polymeric materials.

1.5.1. Tapered fibers

Fiber tapering is one of the mechanisms for lateral outcoupling of light from an optical waveguide.[59] This involves a gradual change in the diameter of the fiber along its length. When a light ray is focused into the fiber core at an input angle θ, it is initially guided through the tapered region by total internal reflection. At each reflection within the fiber, the propagation angle of the ray relative to the fiber's optical axis increases by an amount equal to the taper angle Ψ (**Figure 6**).[47] This process continues until the ray reaches a critical section where total internal reflection is no longer maintained, resulting in the ray radiating into the surrounding medium.

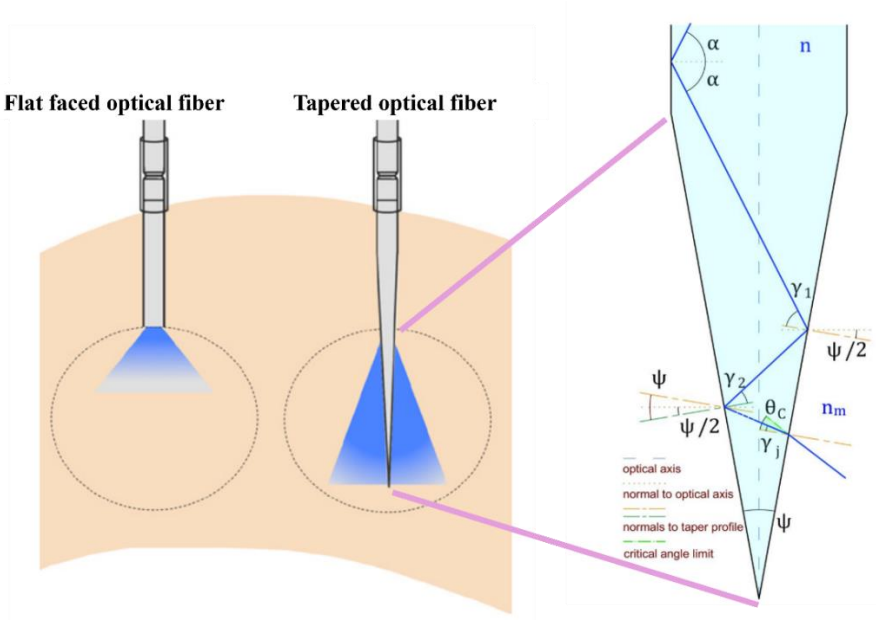

Figure 6. Comparison of the shape and emission profile of flat vs. tapered optical fibers, including single-ray tracing within a tapered fiber.[47] Reproduced with permission from Springer Nature.

The location of this light-emission point along the Fiber depends on the input angle θ, the fiber's numerical aperture (NA), and the taper angle. Adjusting these parameters allows for precise control over the side emission profile.

Pisanello et al. [47] (**Figure 7 A-D**) fabricated tapered silica optical fibers by thermal drawing. The fibers were designed with taper angles from 2° to 8° and lengths between 1.5 mm and 5.6 mm. The tapered fibers enabled homogeneous and spatially defined illumination of path lengths up to 1.8 mm and were applied to optogenetic activation of mouse brains. Incoupling all light angles within the NA range allowed emission along the entire taper. Site-selective illumination was achieved by using specific incident angles. This enabled selective activation of locomotion behaviors in mice by irradiating specific striatum sub-regions. The illumination of extended brain structures and subregions of interest along a tapered segment lowered the photodamage to the brain caused by flat-faced fibers. The devices were tested in the mouse motor cortex and striatum, requiring five times less excitation power than flat-faced fibers to achieve a comparable effect at both depths. Furthermore, even at higher power levels, tapered fibers exhibited more pronounced inhibition, suggesting they stimulate a greater number of neurons over a larger area.

In subsequent work[75b] (**Figure 7E**), tapered fibers with illumination lengths up to 3 mm were attained by increasing the NA of the waveguides. This allowed for the simultaneous illumination

at two different brain depths using 473 nm and 561 nm light injected at different angles at the same time.

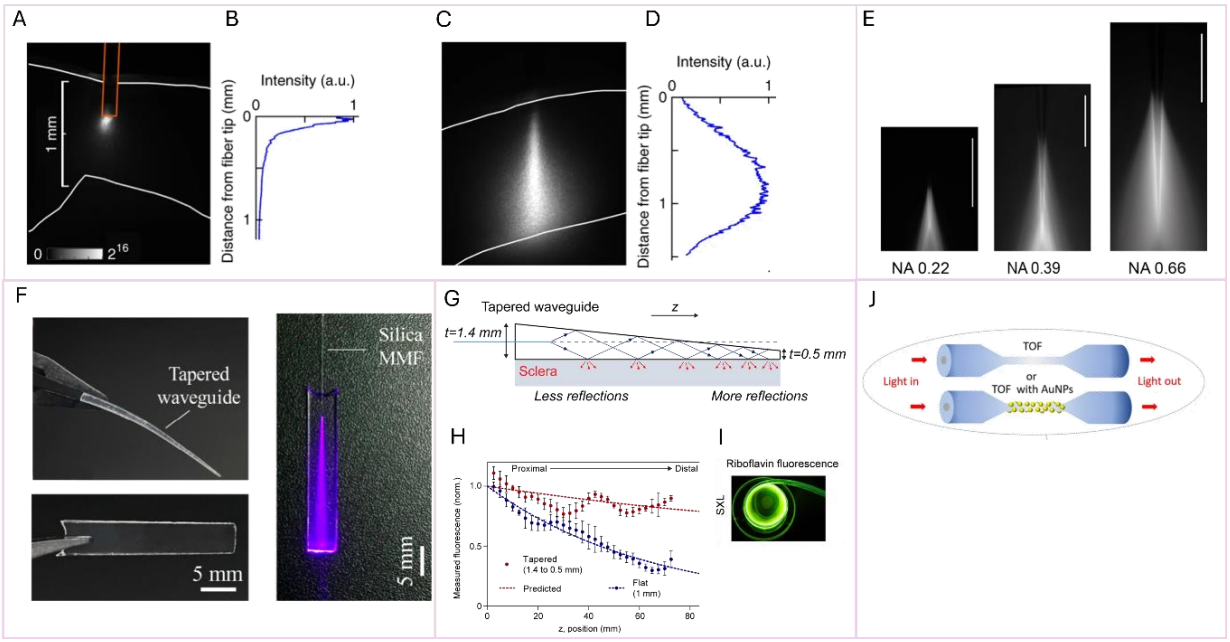

Figure 7. Side emission waveguides using tapering strategy. A) A flat-cleaved fiber demonstrates B) Low light penetration depth in a fluorescently stained brain slice, in contrast to C) The broader emission profile anticipated from a tapered fiber when light is coupled into the fiber and D) The intensity distribution along the emission length.[47] Reproduced with permission from Springer Nature. E) The depth of an emission spot from the taper tip could be varied based on the NA. scale bar 1 mm, Reprinted with permission from [75b] Copyright © 2018. F) Tapered PEGDA waveguides with extended emission profile. Reprinted (adapted) with permission from [97] Copyright 2018 American Chemical Society. G) Tapered PDMS waveguide design with H) extended fluorescence emission profile 70 mm. Image of porcine eyeballs during illumination with blue light.[77] I) Tapered narrow waisted silica fiber. Copyright © 2023.[98]

Tapering geometries have also been explored to achieve side emission in poly(ethylene glycol) diacrylate (PEGDA) hydrogel waveguides (**Figure 7F**).[97] The tapered hydrogel waveguide was fabricated by moulding the PEGDA precursor solution into a tapered rectangular mold and curing it by photoinitiated radical polymerization. The resulting waveguide dimensions were 0.5−1.1 mm in thickness, 5 mm in width, and 30 mm in length. A thin film of PEGDA doped with quantum dots was coated around the tapered fiber while molding for sensing. The waveguides with taper angles of 1.2° and 2.3° resulted in scattering intensities of approximately 0.3 and 0.45

dB mm^{-1}, respectively, over a 20 mm length. The tapered hydrogel waveguide demonstrated in-situ and rapid sensing of Pb^{2+} with high selectivity and sensitivity within biological tissues.

Another example of tapered hydrogel waveguides is the work by Kwok et al., [77] (**Figure 7G,H**) who developed flexible optical waveguides from polydimethylsiloxane (PDMS) elastomer. The waveguides were fabricated by curing a mixture of PDMS base and curing agent in customized molds to create elastomer sheets, which were then cut into waveguides. The dimension of these waveguides was 75 mm in length, 5 mm in width, and tapering from a 1.4 mm thickness at the proximal end to 0.5 mm at the distal end. The PDMS waveguides showed >95% transmittance in the VIS to NIR range (400-800 nm). Propagation loss measured using the cut-back method, was 5.9×10^{-3} mm^{-1} in scleral tissue and 4.4×10^{-3} mm^{-1} in air. The waveguides were used for periscleral cross-linking on porcine eyes with 445 nm blue light and riboflavin as photosensitizer (**Figure 7I**). Irradiation at 25 and 50 mW cm^{-2} for 30 minutes increased the Young's modulus of the sclera, indicating stiffening of the tissue as a consequence of the photoinitiated crosslinking. In another work, Ujah et al fabricated a tapered optical fiber by pulling or stretching the silica fiber (Φ = 125 µm) while it was heated to create a narrow waist (Φ = 5 or 12 µm) in the middle section in 5 mm length (**Figure 7J**).[98] This tapering enhances light interaction with the surrounding environment due to the evanescent field, making it more sensitive to refractive index change and glucose detection. The fiber was coated with gold nanoparticles (AuNPs) to enhance sensitivity through localized surface plasmon resonance.

Table 2. Reported methodologies for fabricating side-emitting fibers.

Side-emission mechanism	Material	Fabrication method	Geometry	Side-emission length	Optical properties	Ref.
Tapered	Commercial core-cladding silica	Thermal drawing	Taper angle Core diameter = 50 μm Cladding diameter = 125	1.8 mm	NA = 0.22 , 0.39	[47]
Tapered	Commercial core-cladding silica	Thermal drawing	Taper angle = 2-8 ° h NA=0.22, core/cladding=50/125μm NA=0.39, core/cladding=200/225μm NA=0.66, core/ cladding=200/230μm	3 mm	NA = 0.22, 0.39, 0.66	[75b]
Tapered	PEGDA doped with CdTe quantum dots	Injection molding, UV crosslinking	0.5−1.1 mm (thickness) × 5 mm (width) × 30 mm (length) taper angle 1.2 ° and 2.3 °	20 mm	0.3 – 0.45 dB/mm	[97]
Tapered	PDMS	Molding	Taper angle ≈ 34 °	80 mm	n=1.42 scattering loss coefficient to scleral tissue, 5.9 × 10^{-3} mm^{-1})	[77]
Tapered	Silica	Thermal drawing		5 mm		[98]

Surface patterning	PLGA, PLA, PVP, Silk fibroin	Molding, laser cutting with wave structures	200-800 µm thick, 1-10 mm long, comb-shaped or H-shaped waveguides	≈ 10 mm	580 µm width PLA: 0.15 dB mm^{-1} in air, 0.62 dB mm^{-1} in water, 1.5 dB mm^{-1} in oil	[61]
Surface patterning	Poly(methylmethacrylate), Silica	Chemical etching, sandpaper roughening, laser writing	750 µm diameter, 35 cm length, roughened over last 10 cm	10 cm	0.5-3.5 dB cm^{-1}	[99]
Surface patterning	Commercial core-cladding silica	Thermal drawing, followed by metal coating as Reflective layer with FIB-milled side-emission windows	NA=0.22,core/cladding=50/125 µm NA=0.39, core/cladding=200/225µm NA=0.66, core/ cladding=200/230µm	20 µm x 20 µm laser-cuoptical windows (15-60 µm)	NA = 0.22, 0.39 and 0.66	[75a]
Surface patterning	Polyurethane (PU) core, Polydimethylsiloxane (PDMS) cladding	Mold casting, coated with reflective silver layer	Ribbon-shaped core-cladding, coated on three sides with reflective silver	70 × 4 × 1.8 mm	NA = 0.5	[36]
Scatterers - Cladding	Fused silica core, sol-gel coating with Ag clusters	Dip coating in sol-gel bath with thermal treatment	440 µm core diameter, segments up to 100 mm	Up to 100 mm	0.063 ± 0.003 mm^{-1} for the photoluminescence and 0.062 ± 0.002 mm^{-1} for UV	[100]
Scatterers - Cladding	Quartz core, silicone cladding, TiO_2 coating	Dip coating in $Ti(OBu)_4$ sol	600 nm TiO2 layer, 7.54 nm crystallite size	Uniform over 10 meters	Optical loss ≈ 1.81 dB m^{-1}	[101]

Scatterers - Cladding	Silica core, UV-transparent polymer cladding with silica nanoparticles	Stripping cladding, coating with aminated silica spheres and Cytop polymer	1 mm core, 5 cm length	Total length of 5 cm	2.9 log inactivation of *Escherichia coli* at a delivery dose of 15 mJ cm^{-2}	[102]
Scatterers - Core	PES as a waveguide and microbubbles as scatterers	Localized heating (150 – 200 °C)	300 and 800 µm fiber diameter/Bubbles formed ~30 µm inside from the outer surface	5.4 cm	0.7 - 0.8 dB cm^{-1} at 633 nm	[103]
Scatterers - Core	PEGDMA/PS/TiO_2	Moulding and manually pipetting the scatterers	3 cm long, 2mm diameter fibers	≈ 1 cm	Not mentioned	[3a]

1.5.2. Surface patterned fibers

Surface patterning is another method for controlled light out-coupling along an optical fiber by disrupting TIR. Surface patterning introduces irregularities or specific geometrical features (e.g., grooves, ridges, or microstructures) on the surface of the waveguide. These patterns create local angles and surface normals that vary along the waveguide's length. When light encounters these irregularities, it is reflected and refracted at angles that do not satisfy the TIR condition. This results in light escaping the waveguide.

Nizamoglu and coworkers (**Figure 8A,B**)[61] fabricated patterned optical waveguides from the thermoplastic polymers poly(D,L-lactide-co-glycolide) (PLGA) and poly(L-lactic acid) (PLA) and from hydrogels obtained from polyvinylpyrrolidinone (PVP) and silk fibroin solutions. Polymer films were obtained by moulding. Polymer films with thicknesses ranging from 200 to 800 µm and lengths from 1 mm to 10 mm were laser-cut into specific shapes, like comb-shaped or H-shaped waveguides. Sine-wave surface patterns with different periods (0.23 and 0.11 mm) were introduced for side emission. A 650 µm PLA wide waveguide, showed a loss coefficient of 0.16 dB mm^{-1} in air 532 nm, 0.76 dB mm^{-1} in water, and 2 dB mm^{-1} in oil. Thicker waveguides exhibited lower loss coefficients. A PLA waveguide with a width of 580 µm showed an optical loss of 0.15 dB mm^{-1} in air, 0.62 dB mm^{-1} in water, and 1.5 dB mm^{-1} in oil for 532 nm. These waveguides were used for photochemical tissue bonding (PTB), using Rose Bengal dye as a tissue photocrosslinker. A 10 mm incision in porcine skin was closed using a comb-shaped PLA waveguide array and 532 nm light. The waveguide was fabricated by melt pressing the material into a thin film, followed by laser cutting to achieve the desired shape.

Wondraczek et al. (**Figure 8C**)[99] developed side emitting Poly(methylmethacrylate) (PMMA) and silica waveguides through roughening the surface of the fibers by chemical etching or by sandpaper, and by patterning the surface by laser-written gratings. The dimensions of the side-emitting fibers varied, for example, PMMA fibers with a diameter of 750 µm and a length of 35 cm were used. The roughened section of these fibers using sandpaper extended over the last 10 cm of the fiber. The optical loss of the fibers varied with the surface roughness. Optical attenuation values ranging from 0.5 to 3.5 dB cm^{-1} were reported. By immersing the fibers within photobioreactors, an enhancement in the illuminated volume was achieved compared to top-surface illumination methods. This led to an increase in the proliferation of microalgae Haematococcus pluvialis by 93%. Nevertheless, achieving uniform side-emission from fibers remains a challenge in this report.

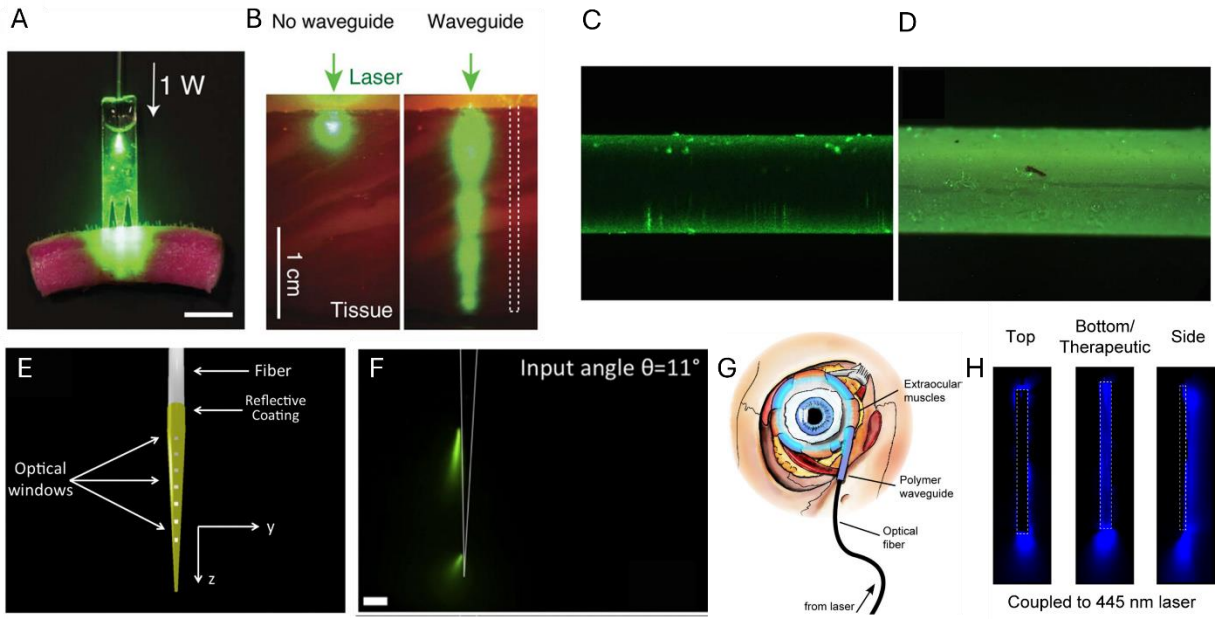

Figure 8 side emission waveguides by introducing surface pattern. A) Cross-section of dyed porcine skin after varying illumination times via a biopolymer-based waveguide bundle. Photobleaching throughout the tissue depth after 30 min confirms efficient light penetration. B) Microscopic images of bovine tissue (~2 mm thick) before (left) and after (right) waveguide insertion. Left: direct green laser illumination on the surface. Right: laser coupled to an implanted waveguide. Scale bar: 10 mm. Adapted permission from [61]. Copyright © 2016. C) PMMA fiber after acetone etching, and D) PMMA fiber after sandpaper scratching. Adapted with permission from [99] Copyright © 2019. E) Schematic of a tapered fiber with reflective coating and selective piercings, enabling light escape at specific modes. F) Tapered fiber emission in fluorescein-stained mouse brain slices for 11° input-coupling angle. Scale bar 100 μm. Reprinted from [104]. Copyright (2014), with permission from Elsevier. G) Schematic of a waveguide inserted in the orbit for equatorial sclera crosslinking. H) Images of the top, bottom, and side views of a waveguide (dotted white lines) with blue light coupled through an input fiber. Reproduced from [36]. ©2019 The Association for Research in Vision and Ophthalmology (ARVO), with permission from the copyright holder.

The addition of a reflective layer can also create patterned surfaces on the surface of the waveguide. This can be either to create precise emission windows at the nanoscale for controlled light out-coupling or to avoid unwanted light outcoupling from certain regions of a waveguide. Pisanello et. al (**Figure 8E,F**) fabricated gold-coated waveguides with precisely milled side-emission windows using a focused ion beam (FIB).[104] These windows allow for controlled light

out-coupling, which can be independently regulated by adjusting the in-coupling light angles. This enables optogenetic stimulation at various depths, using different wavelengths. Similarly, laser-cut windows measuring 20 µm x 20 µm were added to the cladding of waveguides, enabling side emission at multiple points across brain regions in live mice. In a further study from Pisanello group [75a], the optical window was fabricated by FIB milling of silica fibers coated with aluminum. The FIB removed the metal coating and created features of different dimensions (15-60 µm) at specific taper lengths (230, 750, and 1,250 µm). Using the patterned tapered fiber, dopamine transients with dLight1 were measured in freely moving mice. However, such microfabrication techniques can be labor-intensive, requiring hours of manual work with expensive equipments.

In a study by Kwok and coworkers (**Figure 8 G,H**)[36], outcoupling of light in bending areas was avoided by local coating of the waveguides with a reflective silver layer. They fabricated ribbon-shaped core-cladding waveguides using commercial polyurethane (PU) as the core and polydimethylsiloxane (PDMS) as the cladding, through mold casting that could be wrapped around the equator of ex vivo rabbit eyes to achieve photochemical crosslinking of scleral collagen. Three of the waveguide's surfaces were coated with a reflective silver layer, less than 200 nm thick, which directed light toward the sclera, the intended therapeutic area. Without this reflective layer, bending of the waveguide could cause light to escape towards unintended regions, such as the outer bend, which could damage the retina if even a small amount of light leaked.

1.5.3. Introducing scatterers

Introducing scatterers within an optical fiber disturbs the propagation of light and facilitates lateral light emission along the fiber's length. The scatterers have a different refractive index from the core material and alter the photons' trajectories by refracting and diffracting the photons, thereby allowing some of the light to escape the confinement of total internal reflection. This scattered light exits the fiber and produces side-emission. The control over the side emission profile can be achieved by adjusting the scatterers' size, density, and spatial distribution. Internal scatterers have been incorporated into both the core and cladding of waveguides to enhance light outcoupling. In this section, we review studies focused on integrating scatterers within these regions to optimize light emission.

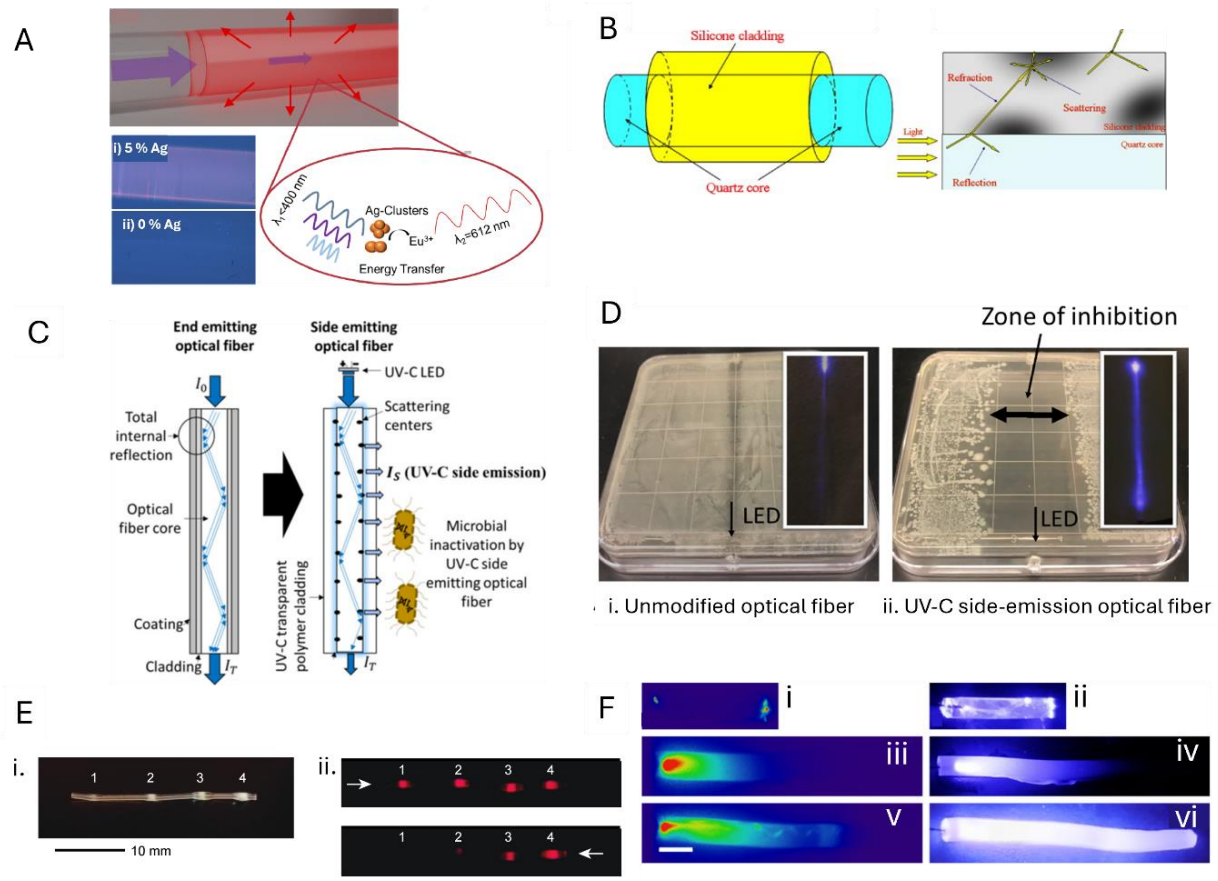

Figure 9. Side-emission optical fibers by introducing scatterers. A) Schematic of a photoluminescent coating on optical fibers, where Ag clusters extract UV energy and transfer it to Eu^{3+} emission centers, enhancing red photoluminescence (i, ii) with and without Ag-co-doping. Adapted with permission from[100] © Optical Society of America. B) Schematic of a single SOF and its irradiated segment highlighting higher-density regions in the cladding.[101] C) Schematic of end-emitting and side-emitting fibers with scattering elements between core and cladding for microbial inactivation. Reprinted (adapted) with permission from [102]. Copyright 2019 American Chemical Society. D) *E. coli* lawn after 480 min of exposure to (i) an unmodified fiber and (ii) a UV-C SEOF connected to a 265 nm LED. Insets show emitted light from each fiber. Reprinted from[105]. Copyright (2020), with permission from Elsevier. E) Photograph of a PES fiber with four scattering spots (i) and (ii) side emission profile of the fiber with light entering from the left (top) and the right (bottom). Adapted with permission from[103] © Optical Society of America. F) Pseudocolor images and photographs of light coupled into PEGDMA 8000 (10%) cylinders with varying PS particle distributions: (i,ii) no particles, (iii,iv) uniform 1 μm PS particles (1 mg/mL), and (v,vi) increasing concentrations (0.25/0.5/1 mg mL^{-1}). Fiber inserted from the left; pseudocolor images captured with 1 ms exposure. Scale bar (i,iii,v): 3 mm.

(ii,iv,vi) samples were ~1 cm, others ~3 cm. Adapted with permission from[3a] © Optical Society of America.

Schröder and coworkers introduced a method to enhance side emission in optical fibers by modifying the photoluminescence of europium (Eu3+) using small clusters of silver (Ag) embedded within a sol-gel coating (**Figure 9A**).[100] Photoluminescence in Ag clusters arises from the re-emission of absorbed light, which is essentially a scattering mechanism where the excited electrons redistribute the emitted light in various directions, including lateral scattering, influenced by factors like nanoparticle size, shape, and surrounding medium.[106] The fibers used in the study have fused silica cores with a diameter of 440 µm obtained by dip coating in a sol-gel containing tetraethyl orthosilicate, triethyl borate, and AgNO3. The fibers are drawn through a sol-filled bath at a controlled speed, followed by thermal treatments to cure the coating layer and develop the Ag clusters. Side emission properties were obtained along segments up to 100 mm in length. The fibers are applied in photobioreactors for algae growth, highlighting their potential to convert UV into visible light to enhance photosynthetic activity. The emission intensity from the fiber diminished exponentially with greater distance from where the coating begins.

Xu et al[101] developed side-glowing optical fibers for photocatalysis under solar light. The waveguide consists of a quartz core and a silicone cladding (**Figure 9B**). A 600 nm TiO2 thin layer with an average crystallite size of 7.54 nm is coated on the silicone cladding by dipping the fiber in a Ti(OBu)4 sol at a controlled speed. The side-glowing light intensity (I_s) is related to the side-glowing coefficient (k), the input light intensity (I_0), the intensity of the exported light, (I), after traveling through a side-emitting optical fiber (SOF) (Δx) and can be described as:

$$I_s = I_0 - I = (4\pi^{-1}).I_0(1 - e^{(-k\Delta x)}) \qquad (1.7)$$

When light is injected from both ends of the SOF, the total side-emitted intensity adjusts accordingly based on the contributions from both light sources:

$$I_s = (4\pi^{-1}).I_0(2 - e^{(-k\Delta x)} - e^{(1-k\Delta x)}) \qquad (1.8)$$

The achieved side-glowing coefficient is k = 0.31 ± 0.03 m^{-1}. To counteract the optical attenuation along the fiber, light is incoupled from both sides of the fiber. The optical fibers allowed uniform side emission over 10 meters and were used in a photoreactor for the photocatalytic degradation of 4-chlorophenol.

Lanzarini-Lopes and colleagues[102] developed side-emitting optical fibers by introducing nanoparticles to the interface of fiber's core and cladding. These nanoparticles scattered incoupled UV light sideways along the fiber (**Figure 9C**). Waveguides with a glass core and a UV-transparent polymer cladding ensured high light transmission. Silica nanoparticles were included in the core and showed size-dependent scattering properties. Smaller particles (50 nm in diameter) absorbed more and scattered less UV light, whereas larger particles (>200 nm in diameter), which predominantly scattered light, were used for the studies. The fabrication process involved stripping the original cladding of a silica fiber, followed by coating a 1 mm core fiber with aminated silica spheres as a scattering layer and with the Cytop polymer cladding. The fiber is UV-transparent across a total length of 5 cm. The side-emitting optical fiber was used to inactivate *E. coli* in water, demonstrating its potential as a water treatment system by effectively distributing UV-C light within a reactor.

In the following work, the same design was applied to surface disinfection and achieved an inhibition zone around the fiber up to 2.9 cm (**Figure 9D**).[105]

The scatterers can also be used within the core of the optical fibers. This concept has been applied to control side emission in polyethersulfone (PES) optical fibers fabricated by thermal drawing (**Figure 9E**). PES can absorb up to 2% w/w water. When exposed to temperatures above the glass transition temperature (T_g 140–200 °C) for several seconds, [103] the absorbed water in the PES fiber vaporizes and forms microbubble cavities within the material. Due to their lower refractive index compared to the surrounding PES matrix, these microbubbles serve as scattering centers. The bubbles formed majorly at a distance of 30 μm from the outer surface of fibers with diameters 800 μm. By varying the heating exposure time, the size and distribution of the microbubbles could be changed, and the resulting optical losses were varied between 0.7 and 2 dB cm^{-1} at 633 nm, which corresponds to attenuation lengths (L_e) between 5.4 and 0.2 cm.

Johannsmeier and coworkers[3a] tailored side emission in waveguides made from poly(ethylene glycol) dimethacrylate (PEGDMA) hydrogels obtained by moulding (**Figure 9F**). For PEGDMA hydrogels with 10% concentration, the attenuation coefficients at 450 nm wavelength were approximately 0.80 dB cm^{-1}. Side emission was achieved by incorporating polystyrene (PS) particles (0.625, 1, and 10 μm diameter) and TiO2 particles (<5 μm) into the precursor hydrogel solution. The transmission, reflection, and optical loss values of the samples containing PS-particles with different diameters showed stronger scattering at shorter wavelengths and a reduced dependency of scattering intensity on wavelength as particle size increased, in agreement with the Mie scattering theory. A longitudinal particle concentration gradient was used to tailor

side emission along the fiber by manually depositing PEGDMA precursor solutions with increasing particle concentrations along the mould. This allowed extending scattering along 1 cm length.

In most of the previously reported strategies for achieving side-emission, controlled side emission is often limited to very short distances (less than 3 mm), or managing side emission loss along the fiber presents significant challenges. While some approaches achieve side emission, they often require light incoupling from both ends of the fiber to compensate for optical losses along the fiber. In methods such as distributed integration or the incorporation of scattering bubbles, the process is typically manual and not continuous. In this study, we address these challenges by introducing a multimaterial extrusion printing technique to distribute scattering elements along soft optical fibers, enabling controlled and tailored side-emission.

1.6. Thermoplasmonic hydrogels for medical applications

Photothermal materials absorb light and convert it into heat, a process called photothermal conversion. In a medical context, photothermal materials are used to raise the local temperature and cause cell death at the tissue where they are injected or transported, or to raise the temperature of thermoresponsive drug carrier materials and trigger drug release at a therapeutic site.

Suitable photothermal agents are materials with high photothermal conversion efficiency and photostability at the application wavelength. In this context, gold nanorods (AuNR) have been extensively reported as interesting photothermal materials due to their tunable localized surface plasmon resonance and high NIR-light absorbance properties.[107] The plasmonic properties arise from the collective oscillation of free electrons in response to incident electromagnetic radiation, particularly in the visible and near-infrared (NIR) regions. The anisotropic shape of nanorods results in two distinct plasmon resonances: a longitudinal resonance and a transverse resonance. The longitudinal resonance, occurring in the NIR region, is particularly notable because it corresponds to the oscillation of electrons along the rod's extended axis, which supports lower energy (longer wavelength) resonances than those observed in spherical nanoparticles. This shift into the NIR range is advantageous for several reasons. NIR light can penetrate into biological tissues more effectively than visible light due to reduced scattering and absorption. Additionally, the position of the longitudinal resonance peak can be finely tuned by adjusting the nanorod's aspect ratio (length to diameter ratio), allowing for control over optical properties for applications that require specific NIR wavelengths. Furthermore, NIR plasmon resonances enhance the sensitivity of surface plasmon resonance (SPR) sensors, as the longer wavelength leads to stronger interactions with analytes near the particle surface. These characteristics make the longitudinal resonance in the NIR region especially useful across various fields, including optics, sensing, and medicine.

1.6.1. Thermoplasmonic hydrogels in photothermal therapies

When gold nanorods are incorporated into a hydrogel, the plasmonic behavior persists. The plasmonic nanorods absorb light and generate a temperature rise within the hydrogel. This localized heating effect has been used to trigger drug release, promote cell growth, or facilitate photothermal therapies. In most cases, AuNPs are incorporated into thermo-responsive polymers to control polymer responses with light. This section describes some examples to illustrate the properties of thermo-plasmonic hydrogels and the variety of compositions reported.

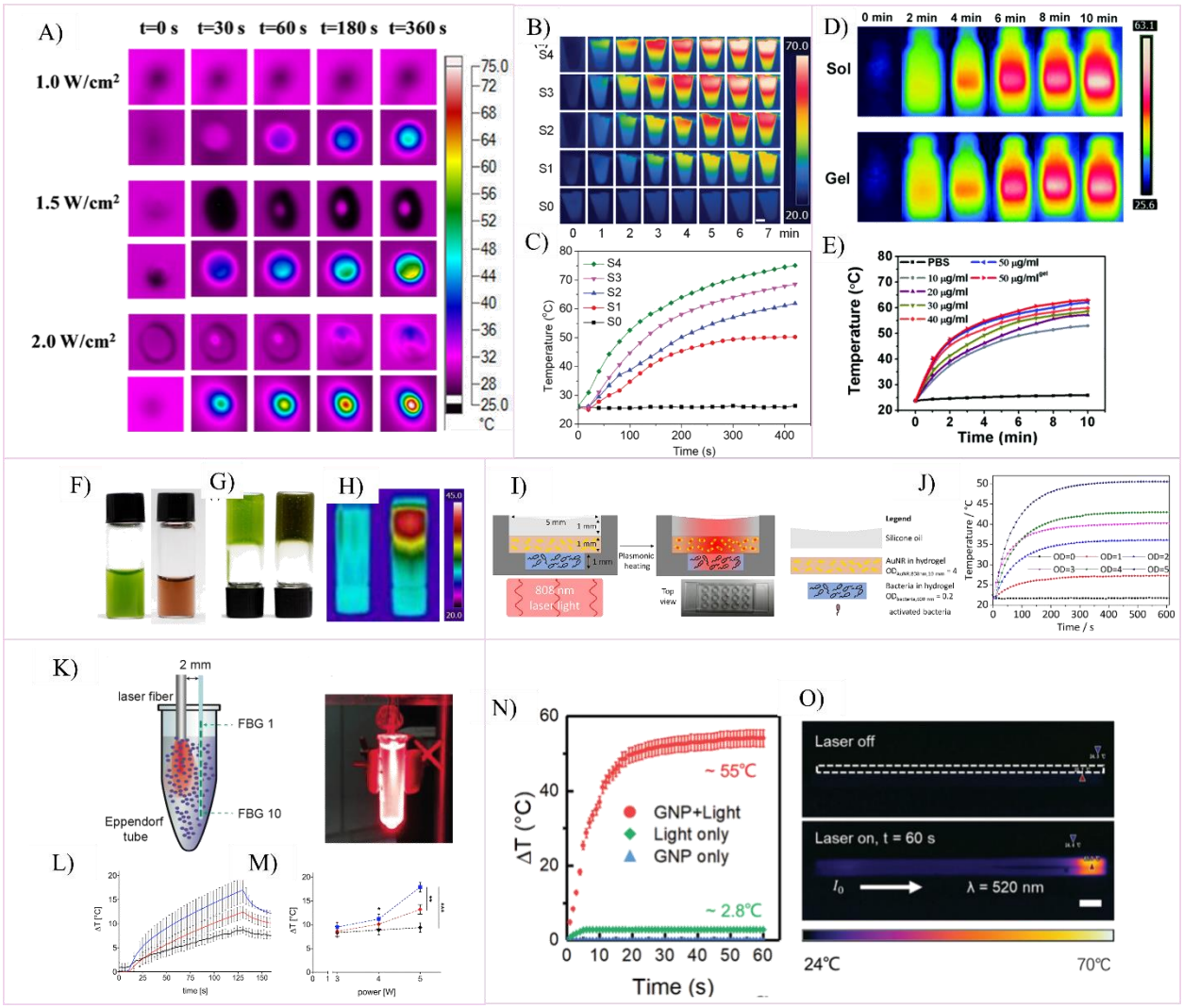

Figure 10. Photothermal behavior of hydrogels containing AuNR. A) Thermographic images of the CGP/Alg-DA/AuNR hydrogel (lower images) in comparison to PBS buffer (pH 7.4) (top images) irradiated at 808 nm for 6 minutes at varying laser powers. Reprinted (adapted) with permission from [108]. Copyright 2019 American Chemical Society. B) Thermal images of PNIPAM hydrogels with varying AuNR mass concentrations (S0–S4) under 808 nm laser irradiation (1150 mW/cm²). Scale bar: 1 mm. S0–S4 correspond to AuNR concentrations of 0, 0.015 – 0.06 mg mL^{-1}, respectively. C) Light-induced heating curves of S0–S4 under the same irradiation conditions.[109] D) Temperature increases of PBS and AuNR-mPECT solutions (0.01–0.05 mg/mL) under 808 nm , laser irradiation (2 W/cm², 10 min). E) IR images of AuNR-mPECT (0.05 mg/mL) at intervals during 808 nm laser irradiation (2 W/cm², 10 min). [110] F) Photographs of Chlorella and AuNRs solutions in glass vials; H) inverted vials displaying Chlorella BSA-Gel and Chlorella AuNRs BSA-Gel after gelation (~60–90 s) H) corresponding thermal images of the inverted vials post-gelation (~60–90 s).[111] I) Illustration of a bilayer hydrogel in a polymer well plate, where the gold nanorod-containing top layer converts 808 nm light into heat to trigger

mCherry expression in bacteria within the bottom layer above 39 °C. J) Thermal response of hydrogel bilayers exposed to 0.8 W/cm² light intensity for different AuNR gel ODs. Reprinted from [112] ©2023, with permission from Elsevier. K) Setup scheme for NIR irradiation and real-time temperature measurement of AuNR samples (left) and image of the sample under NIR exposure, showing red light from the pilot source (right). L) Maximum ΔT recorded for AuNR-loaded hydrogel samples (0.00182 mg/mL, blue; 0.00091 mg/mL, red) compared to control samples (black) under 5 W irradiation; error bars represent standard deviation from three replicates. M) Influence of laser power on ΔT, with significant differences at 5 W compared to 3 W (*p < 0.05, **p < 0.01, **p < 0.001). Reproduced from [113] with permission from the Royal Society of Chemistry. N) Rapid temperature rise observed upon green laser activation. O) Thermal images showing the optical fiber with a GNP-doped segment at the tip. Adapted with permission. [114] © 2021 Wiley-VCH GmbH

Zeng et al. (2019) [108] (**Figure 10A**) encapsulated dopamine modified AuNRs in chitosan and β-glycerophosphate to develop an injectable thermo-plasmonic hydrogel. AuNRs with an average length of 60 nm and a diameter of 16 nm were modified with a thin dopamine layer and incorporated within mixtures of chitosan and dopamine-modified alginate. The composite hydrogel underwent a temperature increase between 52 and 77 °C over 6 minutes when exposed to 808 nm light. Hydrogels injected around a tumor and maintained at a temperature of 55-65°C with repeated NIR irradiation were able to suppress tumor growth.[115]

Jiang and coworkers [109] (**Figure 10B,C**) embedded AuNRs within thermoresponsive poly(N-isopropylacrylamide) (PNIPAM) hydrogels and utilized the photothermal properties for drug release. PNIPAM hydrogels exhibit a reversible volume phase transition around 32°C, transitioning from a swollen, hydrophilic state to a deswollen, hydrophobic state. AuNRs with 59.2 ± 2.5 nm length and 21.5 ± 1.3 nm diameter in different concentrations (0.015 – 0.06 mg mL^{-1}) were embedded in the monomer mixture, together with curcumin (CUR) and doxorubicin (DOX) as drug models and polymerized. Upon exposure at 808 nm, the temperature of the hydrogels increased from 25°C to 65°C within 7 minutes. The rise in temperature induced a traction in hydrogel and enabled light-controlled drug release.

Liu et al. [110] developed an injectable nanocomposite hydrogel for localized chemo-photothermal cancer therapy. In this case, the AuNRs were mixed with methoxy poly (ethylene glycol)-b-poly(e-caprolactone-co-1,4,8-trioxa[4.6]spiro-9-undecanone) (mPECT) and paclitaxel containing mPECT nanoparticles (PTX/mPCT-NPs). Through host-guest inclusion using α-

cyclodextrin, these components were combined to form an injectable hydrogel ($^{AuNR/PTX}$Mpect gel). AuNRs with 45 ± 3 nm length and 8 ± 2 nm width were added at varying concentrations from 0.01 – 0.05 mg mL^{-1}. Upon irradiation with an 808 nm NIR laser at 2 W cm^{-2}, the hydrogel's temperature increased from 23.5°C to 31.1 - 60.2°C within 10 minutes, demonstrating effective photothermal conversion and dependency of temperature rise to AuNR concentration (**Figure 10 D,E**). The hydrogel sustained the release of PTX/mPECT NPs for two weeks in vitro. In vivo experiments in breast cancer mouse models showed complete tumor regression and effective inhibition of tumor recurrence post-surgery.

The treatment of hypoxic tumors, which are resistant to conventional therapies due to low oxygen levels, has triggered the development of technologies for local oxygen generation within the tumor microenvironment.[111] In a recent work, the green microalgae Chlorella vulgaris and AuNRs were integrated into injectable albumin-crosslinked PEG hydrogel via a thiol-maleimide reaction (**Figure 10F,G**). These hydrogels combine the oxygen-generating capability of Chlorella with the heat generation provided by AuNRs. Illumination at 660 nm triggers photosynthesis and illumination at 808 nm controls hyperthermia. An increase in the gel temperature to 41°C was observed in response to alternating on/off 808-nm laser irradiation over 140 seconds (**Figure 10H**). In vivo studies where the microalgae hydrogel mixture (100 µL) was injected around tumors with an average size of 100 mm^3 demonstrated mitigation of the hypoxic conditions within tumors.

AuNRs have also been incorporated in engineered living materials (ELMs) for remote control of biofactories through NIR light.[112] In the studied configuration, AuNRs with a length of 41 nm and a diameter of 10 nm were integrated into a Pluronic-based hydrogel matrix together with thermally responsive bacteria engineered to produce a therapeutic molecule upon a temperature raise to 40°C. The hydrogel had a thickness of 1 mm to allow diffusion of oxygen for bacteria metabolism (**Figure 10I**). At a laser power density of 0.8 W cm^{-2}, the temperature rise (ΔT) ranged from 5°C to nearly 29°C for AuNRs with optical densities (OD) of 1 to 5, respectively (**Figure 10J**).

In all the aforementioned studies, NIR light was applied externally to the hydrogel/AuNR samples. To improve light delivery to the hydrogel, Lacroce and coworkers [113] inserted an optical fiber into plasmonic hydrogel samples (**Figure 10K**). They incorporated AuNRs at concentrations of 0.00182 and 0.00091 mg mL^{-1} into agarose-carbomer-based hydrogels. These hydrogels demonstrated temperature increases of 16.9 and 13.2 °C when irradiated with NIR light (5 W) over 2 minutes (**Figure 10L,M**).

To apply photothermal therapies in vivo, researchers have explored the integration of AuNRs into optical fibers to deliver NIR light directly to the targeted site. Liu et al. [114] developed an optical fiber with gold nanoparticles (20 nm) at 0.005 mg mL^{-1} included in a polydimethylsiloxane (PDMS) core, which was coated with polyacrylamide (PAAm) hydrogel. The fabrication process involved several steps: injection moulding of the PDMS/Au core, curing at 65°C for 2 hours, and subsequent plasma treatment to enhance surface wetting. PDMS/Au fibers with a diameter ranging from 0.3 to 1.5 mm were obtained and coated by immersion in a polyacrylamide bath and pulled out at a velocity of 10 mm/min, with a typical hydrogel coating thickness of 30 µm. The optical fibers generated heat under 520 nm laser light, causing a temperature rise of nearly 50°C within 1 minute over ≈ 2cm (**Figure 10N,O**) (compared to a 3°C increase in fibers without nanoparticles).

In this work, AuNRs are incorporated into segmented optical fibers to enable localized photothermal heating. The thermal response of the fibers is characterized in **Chapter 4.**

Table 3. Thermo-plasmonic hydrogels for photothermal therapies.

Material / AuNR concentration (mg mL^{-1})	Geometry	Irradiation setup	Temperature rise	Demonstrations	Ref.
CS/β-GP/Alginate-Dopamine/Dopamine modified AuNR	Cylindrical hydrogel (1.0×1.0×1 cm^3)	NIR laser beam	52 °C, 60 °C, and 77 °C for laser powers (1.0, 1.5, 2.0 W cm^{-2}	In vivo antitumor test	[108]
PNIPAM//DOX/CUR/AuNR(0.015 – 0.06)	Test tubes	NIR laser beam	20-50 °C	Controlled drug release	[109]
PTX/mPECT NPs/AuNR (0.01 – 0.05)	Glass bottles (D = 1 cm)	NIR laser beam	36.7 °C at 2 W cm^{-2}	Local chemo-photothermal synergetic cancer therapy	[110]
4-arm PEG-Mal/Chlorella/AuNR (≈ 0.167)	1.5 mL Eppendorf tubes	NIR laser beam	36.7 °C 0.5 W cm^{-2}	O2-generating and heat-emitting hydrogel for treating hypoxic tumors	[111]
PluDA/thermo-responsive bacteria/AuNR (0.035-0.175)	Wellplates	NIR laser beam	≈ 5 – 29 °C	Stimulation of Thermo-responsive bacteria within the hydrogel	[112]
Agarose/Carbomer 974P/AuNR (0.002)	1.5 mL Eppendorf	NIR laser fiber inside hydrogel	16.9 °C (0.00182 mg $mL^{-1)}$,13.2 °C (0.001 mg mL^{-1}) 8.6 °C for the control sample	The photothermal effect of the composite	[113]
PDMS/PAAM/AuNR (0.005)	Optical fiber 2 mm diameter × 100 mm length, doped length: 2 cm	Waveguiding the NIR	ΔT 55°C within 1 minute	The photothermal effect of the composite	[114]

1.7. Pluroic hydrogels

Pluronic F127 (F127) is a thermoresponsive, amphiphilic copolymer composed of polyoxyethylene-polyoxypropylene-polyoxyethylene (PEO-PPO-PEO) blocks (70 wt.% PEG, Mn ≈ 12 600 g mol^{-1}).[116] It exhibits inverse thermogelation, meaning it transitions from a liquid state at lower temperatures to a soft, physical gel as the temperature increases.[117] In aqueous solutions, Pluronic F127 forms micelles at concentrations >1 wt.%. The critical micellar concentration is 0.1 wt.% at temperatures >30 °C.[117-118] At low temperatures, the fluid nature of Pluronic enables the homogeneous incorporation of cells and biopolymers. Various grades of Pluronics, ranging from liquids to pastes and solid systems, have been developed with molecular weights between 1100 and 14,000, depending on the PEO-to-PPO ratio in the Pluronic chain.[119]

Pluronic F127 micelles contain several tens of macromolecules[120], with their aggregation number increasing by temperature. At T< 25 °C, dynamic light scattering (DLS) shows that the micellar diameter is 11–12 nm, showing little variation with temperature changes.[121] Cryogenic transmission electron microscopy (cryo-TEM) estimated the core size of these micelles to be between 5–7 nm. An increase in micellar diameter from 6 to 12 nm when the polymer concentration increased from 5 to 10 wt.% has been observed.[122] At higher concentrations and temperatures, Pluronic F127 forms gel phases where the micelles aggregate and form a physical network. At 25 °C, the sol-gel transition occurs at temperatures above 14°C for polymer concentrations >5 wt.%.[123]

The terminal hydroxyl groups of Pluronic can be chemically modified to attach crosslinkable groups such as acrylates[124], producing mechanically robust and stiff gels. These characteristics make Pluronic F127 highly versatile for developing bioinks. One notable modification is Pluronic diacrylate (PluDA), which features end-chain polymerizable acrylate groups enabling the covalent crosslinking of micelles, thereby maintaining the gel structure. Photocrosslinked PluDA hydrogels show viscoelastic properties and retain the internal micellar structure.[124b, 125]

Wu and coworkers printed 3D microvascular networks with PluDA 23% w/w embedded in a PluDA 25% w/w matrix using omnidirectional printing (ODP)(**Figure 11A**).[126] In this work, they used PluDA both as fugitive writing ink and added a photoinitiator to the reservoir to enable photopolymerization. The inks exhibit shear-thinning behavior and maintain shape stability after deposition, with a high shear elastic modulus $G' > 10^4$ Pa. After curing, the hydrogel matrix shows a compressive elastic modulus E' of ≈ 1.33 MPa. Priks et al.[127] printed Pluronic dimethacrylate (PluDMA) 30 wt.% containing viable microbial cells large-scale (3 cm) high-

resolution (30 µm) (**Figure 11B**). Employing direct-write extrusion printing, 3D hollow racetrack structures measuring 10 × 3 × 3.5 mm^3 were created and applied to immobilized yeast (**Figure 11C**) within these shear-thinning hydrogels.[127] In a study from Liu and coworkers[128], Pluronic F127 diacrylate solution at 27 wt.% concentration was used as hydrogel inks in a multilayer fibrillar extrusion process. The inks were extruded in a filament shape through nozzles with diameters between 30 and 200 µm at pressures from 20 to 140 kPa. The printed fibers were crosslinked by UV exposure to improve hydrogel's mechanical integrity. A living tattoo composed of fibers with different programmed cells that integrated multiple chemical-sensing cells was printed onto an elastomeric sheet and was used as a multimodal sensor (**Figure 11D**).

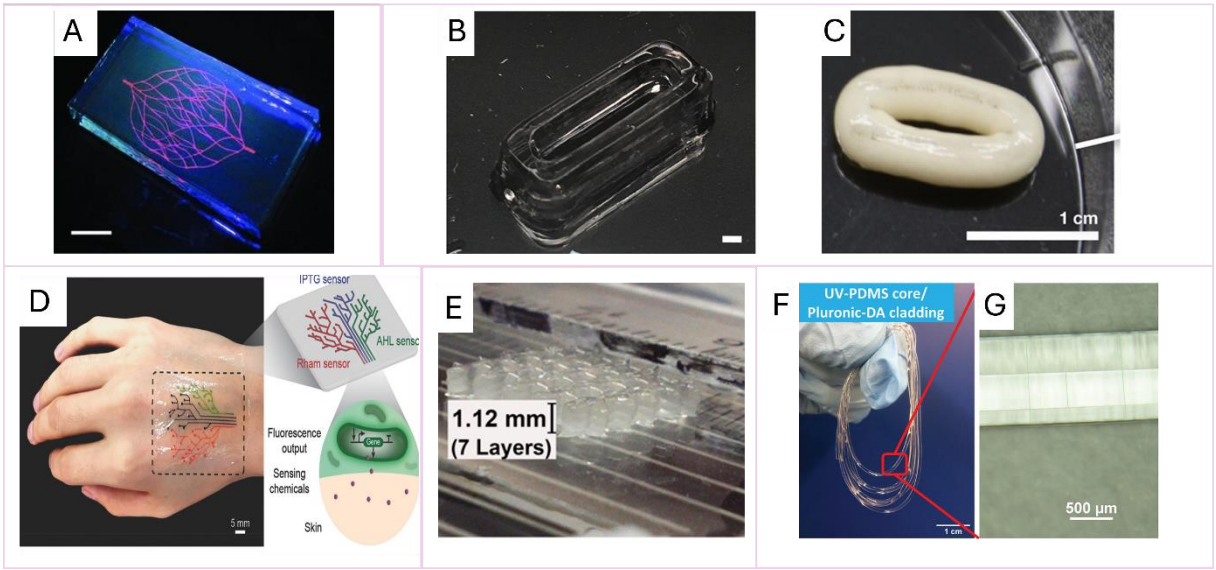

Figure 11. Different examples of extrusion printed PluDA A) Fluorescent image of a 3D microvascular network printed with red-dyed fugitive ink in a photopolymerized Pluronic F127-diacrylate matrix. Scale bar = 10 mm. Reproduced from[126] © 2011 WILEY-VCH Verlag GmbH & Co. KGaA, Weinheim B) printed control structures (cell-free PluDA printed hydrogels) after 24 hours of equilibration C) Yeast-Laden printed PluDA after 7 days of incubation. Reprinted with permission from [127] Copyright 2020 American Chemical Society. D) Design of the "living tattoo": A tree-like PluDA pattern with different colored cell types adhered to human skin. The inset scheme shows embedded living sensors within the tattoo that fluoresce in response to specific chemicals.[128] E) Side view of the PluDA scaffolds with height of 1.12 mm, equal to 7 layers.[125b] F) Macroscopic and G) Microscopy image of a printed flexible core/cladding optical waveguide with PluDA in the cladding. Reproduced from[60]. © 2022 with permission from Wiley-VCH GmbH.

Müller et al.[125b] used a combination of Pluronic and PluDA for extrusion printing of chondrocytes, with a total polymer concentration of 20 wt.% and a Pluronic to PluDA ratio of 17:3. To improve the mechanical strength of the bioink, hyaluronic acid methacrylate (HAMA) was added. After printing, UV crosslinking of PluDA was performed, followed by the removal of excess Pluronic through low temperature washing (**Figure 11E**). This process resulted in a nanostructured PluDA/HAMA scaffold, which supported high cell viability, with 79.9% of chondrocytes remaining viable after 14 days in culture. Feng et al employed PluDA as cladding in core-cladding extrusion of PDMS waveguides (**Figure 11F,G**). PluDA 33.3 % w/w with RI of 1.377 and fabricated core-cladding waveguides with optical loss values of 0.13–0.34 dB cm^{-1} in air and tissue in a wavelength range of 405–520 nm.[60]

In this thesis, PluDA was chosen as the main matrix for extrusion printing of the waveguide and core and core-cladding fibers with segmented structures is printed in order to achieve controlled optical and photothermal properties.

2. Multimaterial extrusion printing of optical waveguides

2.1. Introduction

Multimaterial extrusion printing allows the fabrication of filaments integrating different material compositions and local properties.[129] It enables the continuous extrusion of filaments where individual segments—each with unique properties and functions—are patterned along their length.[7] The technique uses a microfluidic nozzle where multiple ink channels merge, and the flow of each ink is regulated by independent pumps. These pumps control the order in which the inks are introduced at the nozzle's outlet. To be extruded, inks should have viscoelastic properties, such as a shear yield stress 100 Pa to prevent backflow in the stationary channels and avoid transition zones at the interfaces between the extruded materials.[9a, 129] With multimaterial extrusion, fibers with discrete segments that exhibit different properties along their length can be fabricated. Reported examples include silicon filaments with sub-millimeter-scale segments used in structures with tailored mechanical attributes[9a], as well as voxelated scaffolds composed of alginate/gelatin methacryloyl bioinks loaded with different cell types.[130] This capability makes multimaterial extrusion printing a promising tool for embedding contrasting optical characteristics within soft optical fibers.

In this chapter, the formulation of hydrogel-based inks with different optical properties (waveguiding, scattering, and plasmonic) and their processing into hydrogel optical fibers with customized side-emitting or plasmonic segments by multimaterial extrusion printing is described. By controlling the printing conditions and switching times, fibers with tunable lengths of waveguiding, scattering and plasmonic segments were fabricated. Inks and nozzle designs for core-cladding fiber designs were also developed. **Figure 12** shows a schematic of the segmented A) monofilament and B) core-cladding fibers.

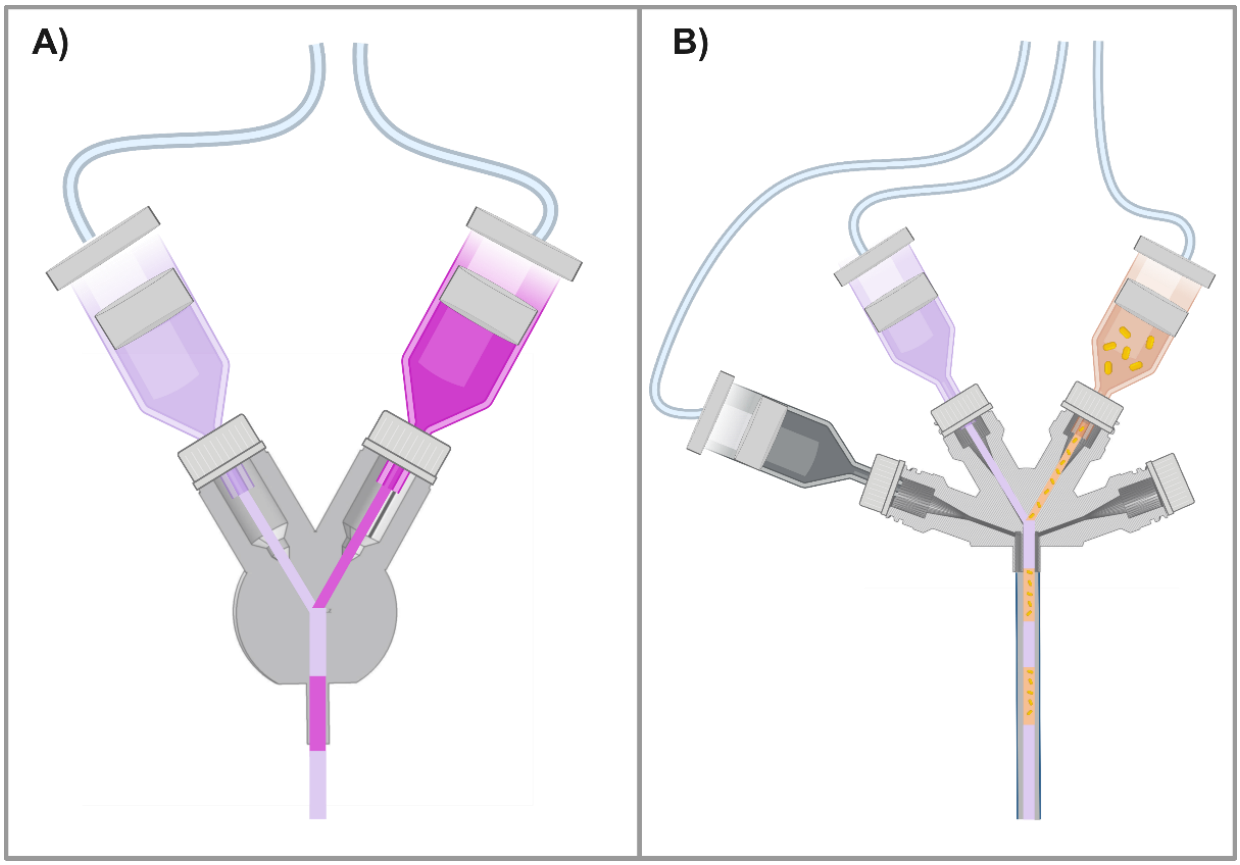

Figure 12. Schematics of the nozzle design for extrusion printing of A) monofilament and B) core-cladding segmented fibers.

2.2. Results and discussion

Inks to be extruded as optical fibers with segments of controlled length and alternating optical properties using a microfluidic nozzle and switched flow need to meet several criteria:

1) From a rheological standpoint, multimaterial extrusion printing demands inks that exhibit viscoelastic behavior with a sufficiently high shear yield stress to prevent backflow in static channels, and the ability to stabilize post-extrusion. Inks reported as suitable for multimaterial printing have shown yield stresses of up to approximately 1600 Pa and have been stabilized through both physical (e.g., gelatin, wax) and chemical (e.g., silicones, epoxies) crosslinking mechanisms.[9a]
2) For waveguiding function, the ink must possess high optical transparency in the visible spectrum after curing. An attenuation coefficient of less than 1 dB cm^{-1} is required to be competitive with state-of-the-art hydrogel optical fibers.[17, 131]
3) For the scattering function, the ink must support the incorporation and homogeneous dispersion of scattering particles to ensure effective optical performance.

2.2.1. Formulation of extrudable hydrogel inks

We selected Pluronic F-127 diacrylate (PluDA) as the ink material for fabricating printable waveguides for the following reasons:

1) Thermosensitivity: Pluronic F-127 is a triblock copolymer and forms physically crosslinked micellar hydrogels within specific concentration and temperature ranges. Solutions of Pluronic F-127 at concentrations exceeding 15% w/w exhibit a lower critical solution temperature (LCST) near room temperature[132], transitioning from low-viscosity liquids to gels when the temperature rises above this threshold. This facilitates the temperature-based processing of Pluronic hydrogels by extrusion.
2) Viscoelasticity: At a concentration of 17% w/w and a temperature of 35 °C, Pluronic F-127 gels display a yield stress of 155 Pa[133], fulfilling the necessary criteria for use as inks in multimaterial extrusion printing. These gels exhibit viscoelastic properties and shear yield stress, and they demonstrate shear-thinning behavior beyond the yield stress, facilitating the extrusion process.[134]
3) Reactivity: Pluronic can be modified with terminal acrylate groups to yield PluDA. This modification does not significantly affect the rheological properties of Pluronic hydrogels [123a] while it enables post-processing stabilization through chemical crosslinking via radical or photopolymerization. PluDA hydrogels, prepared at a polymer concentration of 23.1% w/w, have previously been utilized as photocrosslinkable inks.[60, 81] These hydrogels exhibit mechanical characteristics that make them highly suitable for applications in soft biomedical devices, such as flexible waveguides. **Table 4** provides an overview of the physical properties of PluDA relevant to this study.

Table 4. Properties of PluDA (23.1% w/w) before and after photocrosslinking.

State	Property	Value	Conditions	Ref.
Uncrosslinked[a]	Shear yield stress	0.6 ± 0.1 kPa	22-23 °C	[123a]
	G'	18.4 ± 1.1 kPa	22-23 °C	[123a]
Crosslinked[b]	*G'*	47.5 ± 2.9 kPa	22-23 °C	[123a]
	Refractive index[c]	1.363	20 °C, 589.3 nm	[60]
	Swelling ratio[d]	1.4	37 °C, water, 2 h	[135]

[a] Physically crosslinked gel.

[b] Photocrosslinked by including Irgacure 2959 (0.2 – 0.3 % w/v) and exposing to UV light (365 nm, 1 – 6 mW cm^{-2}) for 1 – 15 min.

[c] Immediately after photocrosslinking.

[d] Hydrogel mass after 2 h of swelling in water divided by the mass of the hydrogel directly after photocrosslinking (time zero).

In previously reported work, PluDA inks with a polymer concentration of 23.1 % w/w were successfully used for extrusion printing of monolithic PluDA fibers with 1 mm diameter by applying 1700 mbar printing pressure.[60] Core-cladding fibers with a PDMS core and a PluDA cladding were also printed using 33.3% w/w PluDA hydrogels.[60] This range of concentrations and printing parameters establish the starting points for ink formulation for core-cladding PluDA-based plasmonic fibers.

The viscosity of PluDA inks at concentrations ranging from 23.1% to 33.3 % w/w at 25°C was characterized using a cone-plate rheometer over a shear rate range of 0.01 s^{-1} to 100 s^{-1} **(Figure 13).** At a shear rate of 0.01 s^{-1}, the measured viscosities were approximately 15.8 ± 0.23 kPa·s for 23.1% w/w, 29.17 ± 1.62 kPa·s for 30% w/w, and 40.29 ± 1.43 kPa·s for 33.3 % w/w. These values indicate an increase in viscosity with higher PluDA concentrations, showing an approximately 2.5-fold increase from 23.1% to 33.3 %. These differences in initial viscosity indicate that higher polymer concentrations require higher extrusion pressures, potentially impacting the printing process. All three inks exhibit strong shear-thinning behavior which is advantageous for multimaterial printing.[9a, 136] Shear thinning inks flow during extrusion while maintaining their structural integrity upon deposition.[4]

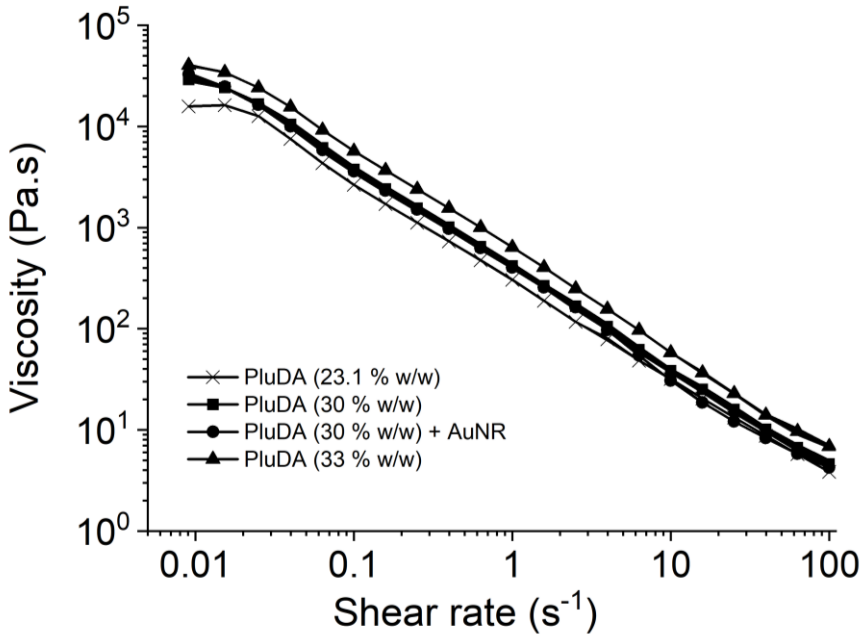

Figure 13. The viscosity of PluDA inks at concentrations of 23.1, 30, and 33.3 % w/w as a function of shear rate.

An important parameter for extrusion multimaterial printing is the critical yield stress (> 100 Pa).[129] [129, 137] Inks suitable for multimaterial printing have shown yield stresses reaching approximately 1600 Pa and have been stabilized using physical approaches like gelatin and wax, as well as chemical methods such as silicones and epoxies. [9a] To see how the critical yield stress varied with polymer concentration, strain amplitude sweeps were conducted on Pluronic inks **(Figures 14 A,B).** As concentration increased from 23.1 to 33.3% w/w, the critical yield stress increased from 665.7 ± 19.2 Pa to 2020.6 ± 99.0 Pa. The higher critical yield stress implies that higher pressures are required to overcome the flow resistance as the polymer concentration in the ink increases.

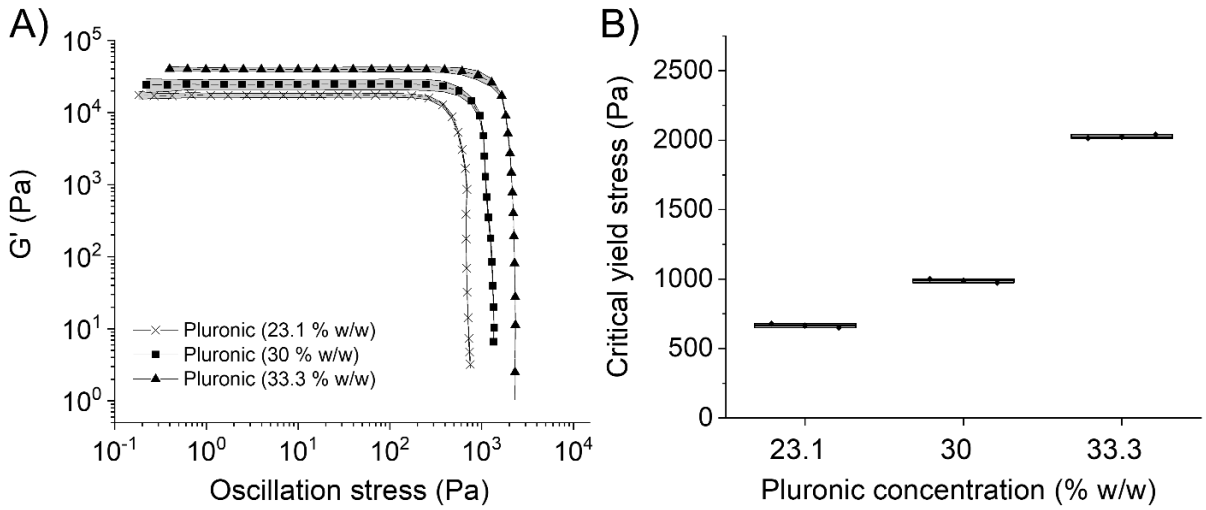

Figure 14. A) Stress sweeps of Pluronic inks at concentrations 23.1, 30, and 33.3 % w/w and B) Corresponding critical yield stress.

2.2.2. Formulation of waveguiding PluDA ink

Waveguiding materials need to have high transparency (transmittance ≥ 90 %) in visible wavelengths.[1] PluDA hydrogels at 23.1 % w/w are transparent at the visible wavelength range (**Figure 15B**).

Waveguiding materials need to have a RI exceeding the RI of the surrounding medium. The RI of tissue ranges from 1.32 to 1.56 for wavelengths between 450 and 1551 nm.[1, 138] Polymeric biomaterials used in hydrogel waveguides are reported to have RI ranging from 1.33 to 1.7. [1, 139] The refractive index of hydrogels is influenced by factors like polymer concentration, chemical composition, water content, temperature, and incident light wavelength.[1, 140] As the concentration increases, the density of the polymer and, therefore the number of interactions between the polymer chains and the surrounding medium increase, resulting in an increase in the

refractive index.[60, 141] The RI of 23.1 % w/w PluDA is 1.363 (**Table 4**). This RI value is higher than tissue (1.32 reported for skin). In addition, this is an intermediate RI value in hydrogel materials (1.33-1.37) [1] and allows the selection of cladding materials with lower RI for total internal reflection (see **section 2.2.5**).

PluDA solutions below the LCST are low viscous fluids and can be mixed with other components to vary their optical properties. To formulate side-emitting PluDA inks, we introduced scattering particles (200-nm-diameter polystyrene nanoparticles, PS-NP) as scattering elements in the PluDA ink. The PS-NP had a negligible impact on the rheological properties of the PluDA solution (**Figure 15A**). The introduction of 0.01 % w/w PS-NP in the ink attenuated the incident light. This attenuation was stronger at decreasing wavelength, indicating optical loss by light scattering (**Figure 15B**). At this NP concentration, 75 % of 520-nm light is attenuated over the 1-cm path length of the UV/Vis measurement, corresponding to an attenuation coefficient of 1.4 cm^{-1}.

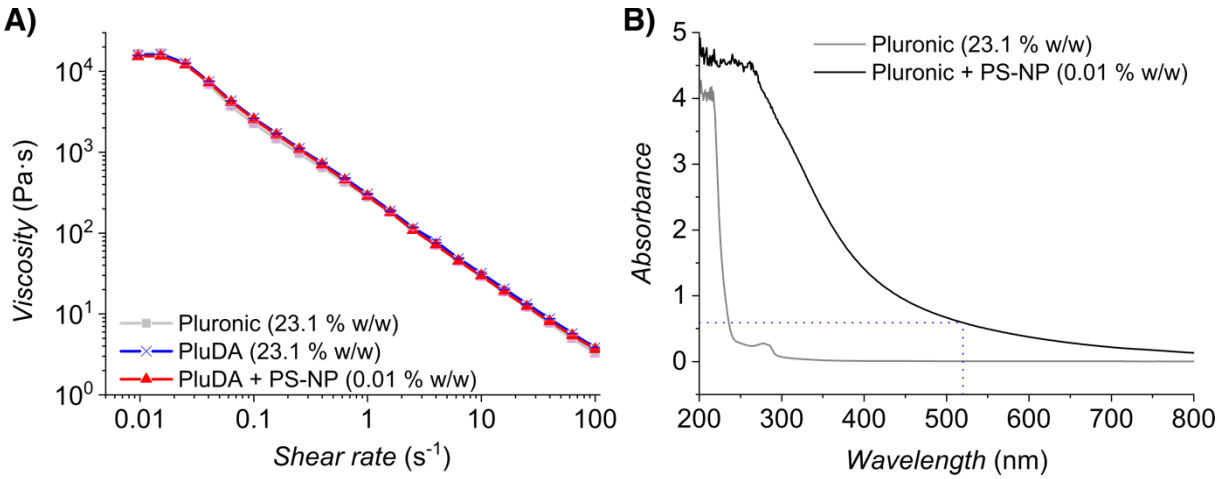

Figure 15. A) Shear sweep rheology curves at 25 °C comparing Pluronic F-127, PluDA, and PluDA plus 200-nm PS-NP (0.01 % w/w) at a polymer concentration of 23.1 % w/w in each case. n = 3 for each ink. B) UV/Vis spectra of Pluronic F-127 (23.1 % w/w) without and with 200-nm PS-NP (0.01 % w/w). In some experiments in this work, we used PS-NPs labeled with Crimson fluorophore to image the position of the scattering segments in the fiber by fluorescence microscopy.

2.2.3. Formulation of PluDA inks with photothermal properties

Photothermal materials, such as gold nanorods (AuNRs), have been integrated into hydrogels to achieve localized heating. AuNRs are particularly advantageous due to their tunable localized surface plasmon resonance (LSPR) in the near-infrared (NIR) range, which enables effective

light penetration through biological tissues. This has been harnessed for applications such as controlled drug release, tumor ablation, and the modulation of biological responses in a variety of hydrogels, including chitosan-based hydrogels[108], PNIPAM (poly(N-isopropylacrylamide)) hydrogels[109], and Pluronic.[112]

According to a previous report, AuNRs embedded in 23% w/w PluDA hydrogels at concentrations from 0.035 to 0.175 mg mL^{-1} retain their plasmonic properties and can induce temperature changes when illuminated at 808 nm.[112] The authors used a bilayer hydrogel sample with a 1 mm thick bottom PluDA layer, and a 1 mm thick PluDA/AuNR top layer with an optical density of 4 ($OD_{AuNR,\ 808\ nm}$=4, corresponding to

$mgmL^{-1}$ particle concentration). When the samples were irradiated with an 808 nm laser with a beam area of 12.6 mm^2, a temperature increase (ΔT) from 10 to 21°C was observed. By increasing the AuNR concentration in the top hydrogel layer to $OD_{AuNR,\ 808\ nm}$=5 (corresponding to 0.175 $mgmL^{-1}$ particle concentration), a ΔT from 5 to 29°C was observed.

We tested a concentration of AuNRs of 0.07 mg mL^{-1} in a 30% w/w PluDA solution. The UV-Vis spectrum of this composition is shown in **Figure 16A**. Two absorbance peaks are visible at 520 and 808 nm which correspond to the localized surface plasmon resonance (LSPR) of the AuNRs. The 520 nm peak, known as the transverse plasmon resonance, corresponds to electron oscillations along the nanorod's short axis. The 808 nm peak corresponds to the longitudinal plasmon resonance and is associated with electron oscillations along the long axis of the nanorod and is sensitive to the nanorods' aspect ratio. The strong absorbance at 808 nm confirms the successful dispersion of AuNRs within the hydrogel.

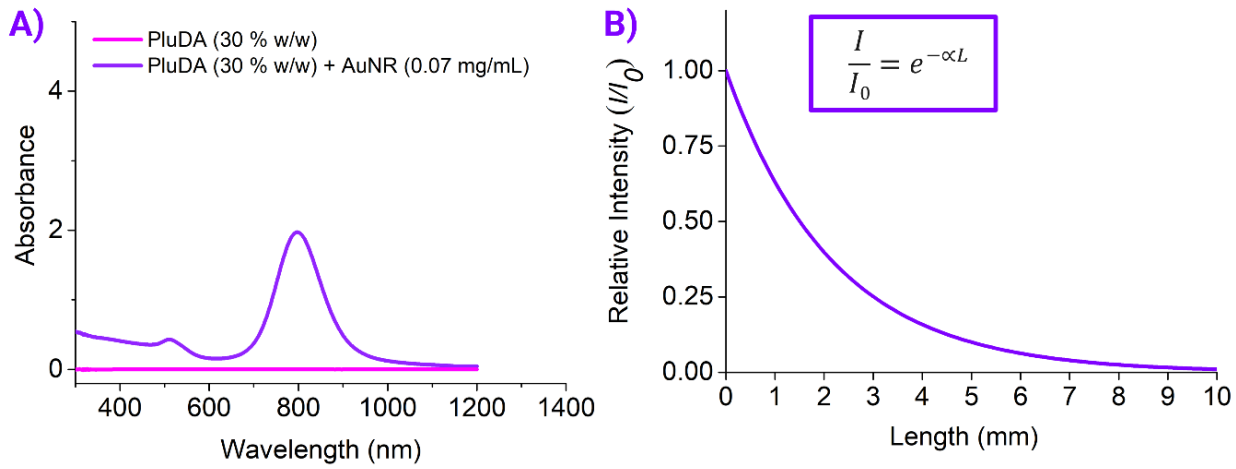

Figure 16. A) UV/Vis spectra of 30 % w/w PluDA ink without and with AuNR (0.07 mg mL^{-1}). B) Theoretical relative light intensity along a 10 mm sample of PluDA 30 % w/w hydrogel with embedded AuNR (0.07 mg mL^{-1}) and α = 0.46 mm^{-1}

To quantify the decay of light per unit length of a waveguide, the attenuation coefficient (α) is used, which represents the optical loss in centimeter distance, expressed in dB cm $^{-1}$. From the absorbance value of the 30 % w/w PluDA ink with 0.07 mg mL^{-1} at 800 nm **(Figure 16A)**, we estimated the attenuation coefficient, α, for the plasmonic ink as:

$$Attenuation\ coefficient\ (\propto)(mm^{-1}) = \frac{-ln\left(\frac{I}{I_0}\right)}{x} = \frac{-ln(0.\ 01)}{10\ mm} = 0.46\ mm^{-1}$$

A value of 0.46 mm^{-1} was obtained according to the above-mentioned formula. The expected decay of the intensity along a 10 mm path is shown in **Figure 16B**. According to these results, 91% of the incident light is absorbed by the gold nanorods within 5 mm. This provides information about the maximum realistic length scale at which the plasmonic waveguide with embedded 0.07 mg mL^{-1} AuNRs will show a photothermal effect (**Chapter 4**).

2.2.4. Formulation of PluDA inks for coextrusion of core-cladding optical fibers

In core-cladding waveguide designs, the RI of the core needs to be higher than that of the cladding and the RI contrast determines the TIR. Pluronic F127 aqueous solutions are transparent above 300 nm [142] across a concentration range of 1 to 35 wt.%. [143] The RI of PluDA solutions, measured across the wavelength range of 404 to 707 nm, increased as the polymer concentration increased from 23.1 to 33.3% w/w. In all wavelength ranges, the refractive index rises with increasing polymer concentration **(Figure 17)**. This indicates that RI contrast in a core-cladding Pluronic fiber can be achieved using 23.1 % w/w PluDA hydrogel in the cladding and PluDA hydrogels with higher concentrations in the core.

To estimate the RI of Pluronic hydrogels at longer wavelengths of relevance for our studies, we fitted the experimental data to the Cauchy model, which describes the wavelength-dependence of the RI in transparent materials: [144]

$$n = f(\lambda) = A + \frac{B}{\lambda^2} + \frac{C}{\lambda^4} \qquad (\lambda \text{ in } \mu m)$$

Here, the terms A, B, and C are the Cauchy coefficients: A is the refractive index of the material at an infinite wavelength and B and C are the dispersion coefficients that describe how the refractive index changes with the wavelength of light. The estimated RI values of PluDA hydrogels at 23.1, 30, and 33.3% w/w concentration at 808 nm were 1.3602, 1.3701 and 1.3739. The study demonstrates that a refractive index (RI) contrast suitable for core-cladding optical

fiber designs using Pluronic-based hydrogels can be achieved by employing a lower polymer concentration (23.1% w/w) in the cladding and higher concentrations (e.g., 30% w/w or 33.3% w/w) in the core. This configuration ensures that the core possesses a higher RI than the cladding, which is essential for effective light guidance within the fiber. **Table 5** summarizes the optical and flow properties of the three PluDA inks at concentrations of 23.1%, 30%, and 33.3% w/w.

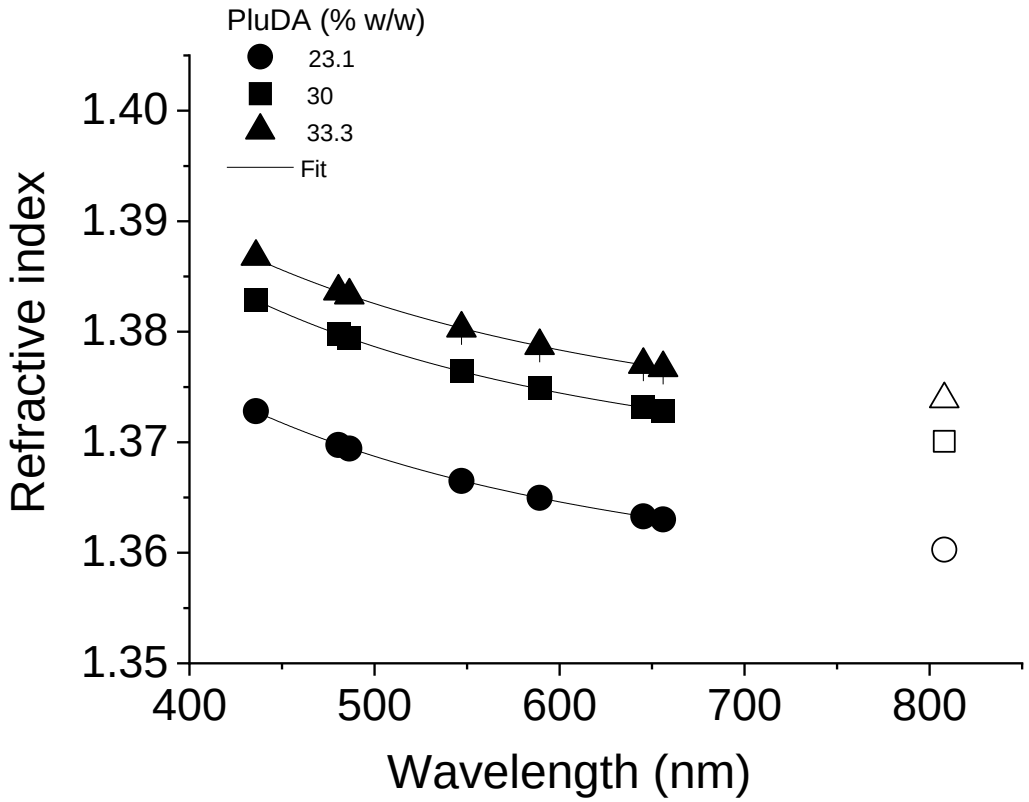

Figure 17. The refractive index of aqueous PluDA inks at concentrations of 23.1 %, 30 %, and 33.3 % w/w were measured at different wavelengths (N=3). The experimental results are fitted to Cauchy model.

Table 5. Summarized optical and flow properties of the uncrosslinked waveguiding inks.

Concentration (% w/w)	Critical yield stress (kPa) at 22-24 °C	Viscosity (kPa s^{-1}) at 0.009 s^{-1}	Estimated refractive index at 808 nm
23.1	0.67 ± 0.02	15.80 ± 0.23	1.3602
30	0.99 ± 0.12	29.17 ± 1.62	1.3701
33.3	2.02 ± 0.10	40.29 ± 1.43	1.3739

2.2.5. Flow properties of Pluronic inks for multimaterial extrusion of strands

To print multimateiral fibers with segments of two different compositions (waveguiding and scattering or plasmonic), the two inks were connected to a Y-shaped nozzle with two inlets of 500 mm diameter and an outlet of 1 mm (**Figure 18A,B**). A pneumatic pressure controller connected to ink-filled syringes allowed switching the flow between the two inlet channels of the nozzle and extrusion of strands with segments of alternating compositions. (**Figure 18 C,D**)

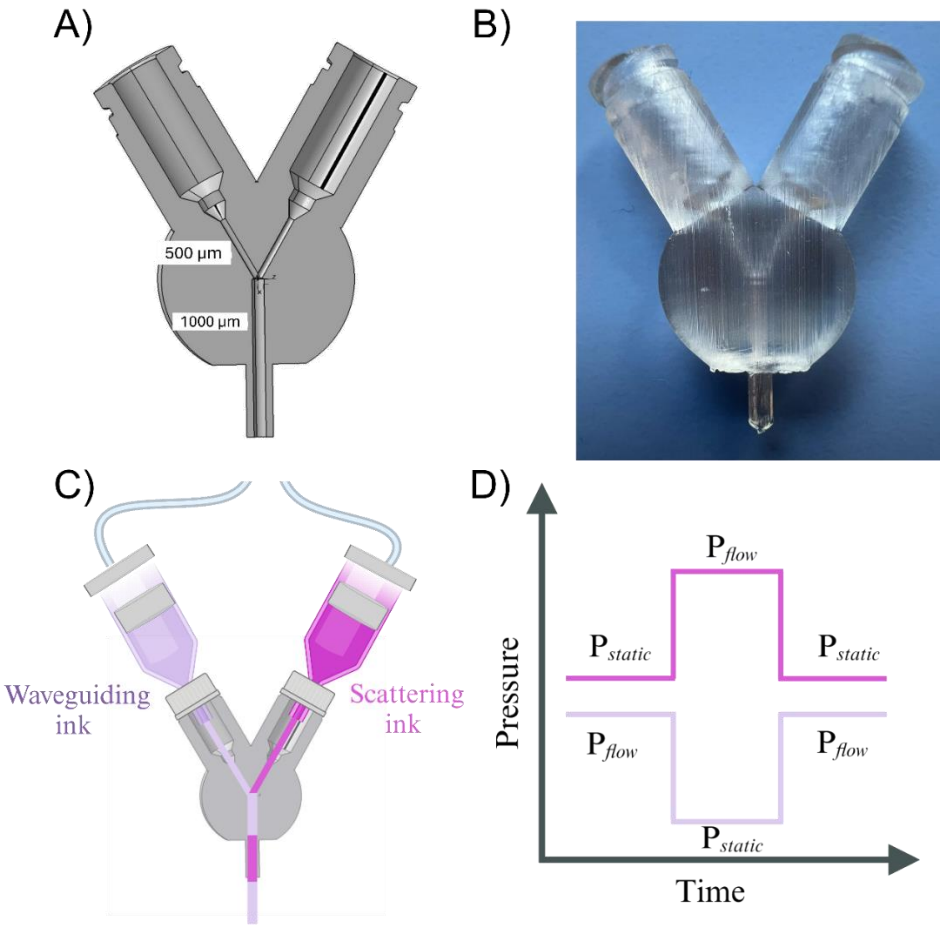

Figure 18. A) Image depicting the cross-sectional view of the Y-shaped nozzle design. B) Image of the printed nozzle C) Scheme of the extrusion printing setup with D) Schematic pressure profile.

At the printing temperature of 22.7 ± 0.6 °C, PluDA 23.1% w/w is a physical gel inside the syringes. Flow pressures (P_{flow}) of 700 mbar and switching times between 0.5 and 5 s were tested for extrusion printing of 23.1% w/w. Continuous and alternating flow of the two Pluronic inks through the nozzle was observed by applying a P_{flow} = 700 mbar alternately to the two inlets (**Figure 19).** The segment length was adjusted by modifying the switching times and ranged from ≈ 12 mm to 0.8 mm.

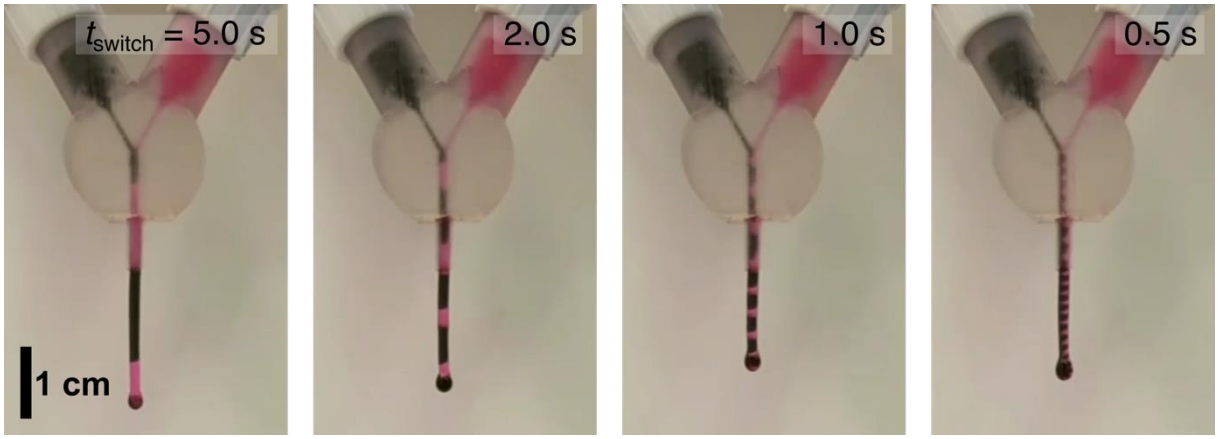

Figure 19. Snapshots from a video of the multimaterial extrusion process using Pluronic F-127 (23.1 % w/w) inks using different switching times. The inks were stained with carbon black (0.5 % w/w) and pararosaniline (0.06 % w/w) for visualization. P_{flow} = 700 mbar, P_{static} = 0 mbar. The scale bar applies to all images.

Pluronic solutions with higher concentrations, for example 30 and 33.3 % w/w show higher viscosity and critical yield stress and are expected to require higher pressures to overcome the enhanced resistance to flow. The high viscosity could also affect the resolution of switching during the extrusion process, a critical parameter for achieving multimaterial structures.

We systematically studied the flow behavior of 30 and 33.3 % w/w Pluronic inks at different pressure conditions. We used Pluronic F127 for these preliminary experiments, which has similar flow properties to PluDA inks. To extrude segmented fibers with alternating ink compositions, we used a Y-shaped nozzle with two inlets of 500 µm diameter connected to a pressure controller that switched between two ink cartridges at desired frequencies and pressures. For 30 % w/w Pluronic ink, continuous extrusion occurred within the P_{flow} range of 1000 to 2000 mbar and a P_{static} of 500-1500 mbar. We investigated the alternating flow behavior of 30% w/w Pluronic inks at different switching times. We added 0.5% w/w carbon black and 0.06 % w/w pararosaniline to the inks to visualize the two different segments. Continuous flow with alternating

compositions was achieved with 30% w/w Pluronic at 2000 mbar Pflow. Segments with lengths between 7 and 1 mm were obtained for switching times between 30 and 5 s **(Figure 20)**. The segments exhibited well-defined segment boundaries with minimal tailing (< 1mm). At the boundary between the segments, the typical parabolic flow profile of a viscoelastic fluid in a laminar flow regime is observed. The parabolic profile is a consequence of the frictional forces of the fluid at the walls of the nozzle.

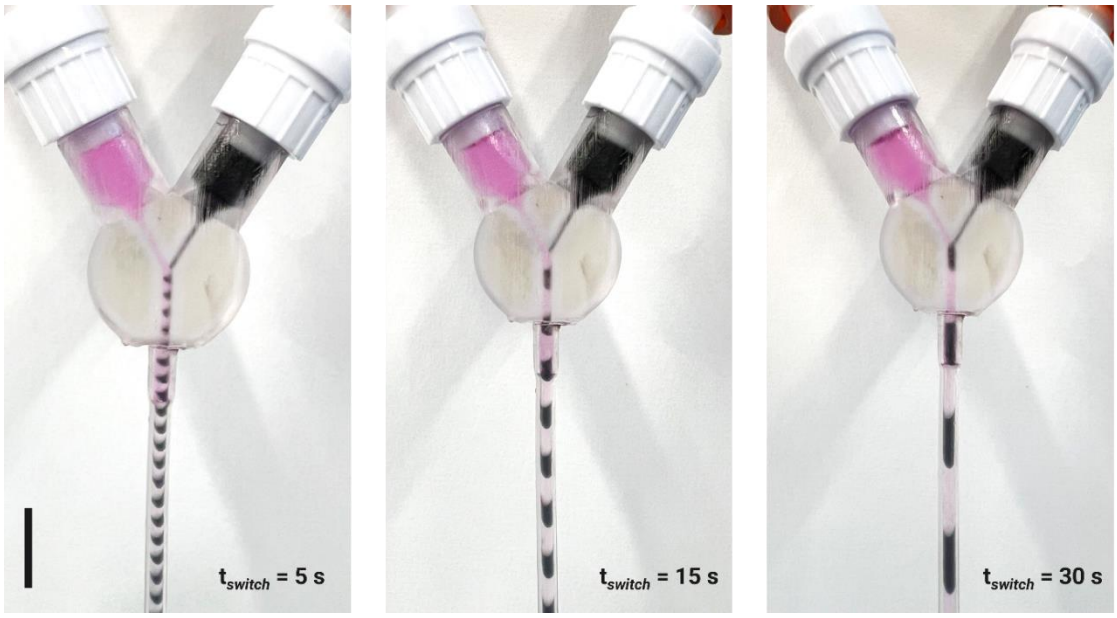

Figure 20. Flow of Pluronic F-127 (30% w/w) inks at increasing switching times. The inks were stained with carbon black (0.5 % w/w) and pararosaniline (0.06 % w/w) for visualization. P_{flow} = 2000 mbar, P_{static} = 1000 mbar. The scale bar corresponds to 1 cm for all images.

The 33.3% w/w Pluronic ink required a pressure range of 2000 to 3000 mbar to achieve stable flow, reflecting differences in both viscosity and critical yield stress compared to lower concentrations. At a shear rate of 0.01 s^{-1}, the viscosity of the 33.3% w/w ink (40.29 ± 1.43 kPa·s) is approximately 1.4 times higher than that of the 30% w/w ink (29.17 ± 1.62 kPa·s) and 2.5 times higher than the 23.1 % w/w ink (15.8 ± 0.23 kPa·s). Similarly, the critical yield stress of the 33.3 % w/w ink (2.02 ± 0.10 kPa) is more than double that of the 30 % w/w ink (0.99 ± 0.12 kPa) and threefold higher than the 23.1 % w/w ink (0.67 ± 0.02 kPa). These differences in viscosity and yield stress explain the significantly higher pressure requirements for 33.3 % w/w ink.

The 30% w/w ink maintains stable flow within a pressure range of 1000–2000 mbar, whereas the 33.3% w/w ink requires pressures of 2000–3000 mbar due to its higher resistance to flow. At pressures below the critical threshold for 33% w/w ink, dripping behavior was observed. This

can be attributed to localized deformation under applied pressure forces exceeding the yield stress in certain regions but insufficient to sustain continuous flow and fill in the tube.

In Pluronic inks at 33% w/w concentration, continued flow with segments with longer tails and ill-defined transition zones was observed **(Figure 21)**. The higher viscosity of the 33% w/w Pluronic ink creates greater resistance to flow which leads to the dragging of the polymer strand when switching occurs. As viscosity increases, the laminar velocity profile flattens[145], as described by the Navier-Stokes equation for incompressible flow.

Simultaneously, higher viscosity reduces wall slip due to stronger intermolecular forces that enhance adhesion between the fluid and nozzle walls. This reduction in wall slip further slows the flow near the walls. Consequently, delayed flow dynamics can negatively impact the resolution of printed segments, as the lack of sharp transitions between material segments compromises their distinctness.

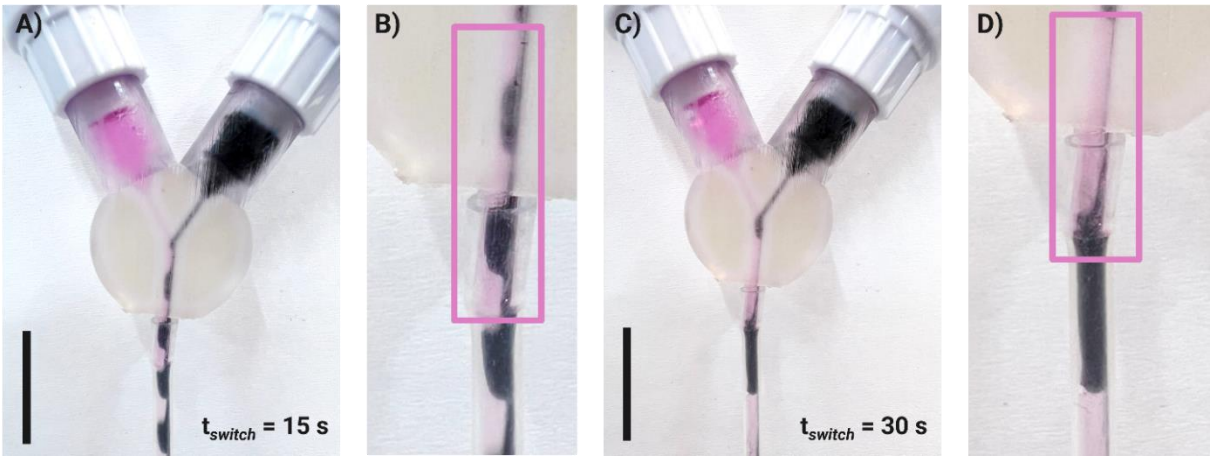

Figure 21. Flow of 33.3 % w/w Pluronic inks extruded at t_{switch} = 15 and 30 s, applied pressure of 3000 mbar, and a static pressure of 2500 mbar. Scale bar is 1 cm.

To identify the $\Delta P = P_{flow} - P_{static}$ that provides well-defined segments with minimal tailing and no backflow between the two channels, experiments were conducted with 30 % w/w Pluronic at a constant P_{flow} of 2000 mbar, a t_{switch} of 30 seconds and at variable P_{static}. These experiments were performed without crosslinking.

At ΔP = 1300 mbar, direct flow from one channel to another was observed (**Figure 22A, B**). [9a, 146] When ΔP was reduced to 1000 to 500 mbar (**Figure 22C,D**), no backflow between channels was observed, and a clear switching between the two inks and shorter tailing of the segments was observed. At ΔP = 300 mbar, simultaneous co-flow from both channels was observed (**Figure 22E**). These findings align with prior research by Skyler-Scott et al.[9a], which demonstrated that

preventing backflow requires that P_{flow} remains below the critical yield stress of the ink in the non-active channel. Failure to maintain this balance leads to backflow or coextrusion, both of which compromise segment quality. A ΔP between 1000 and 500 mbar allowed effective switching between channels and avoided simultaneous coextrusion from both channels.

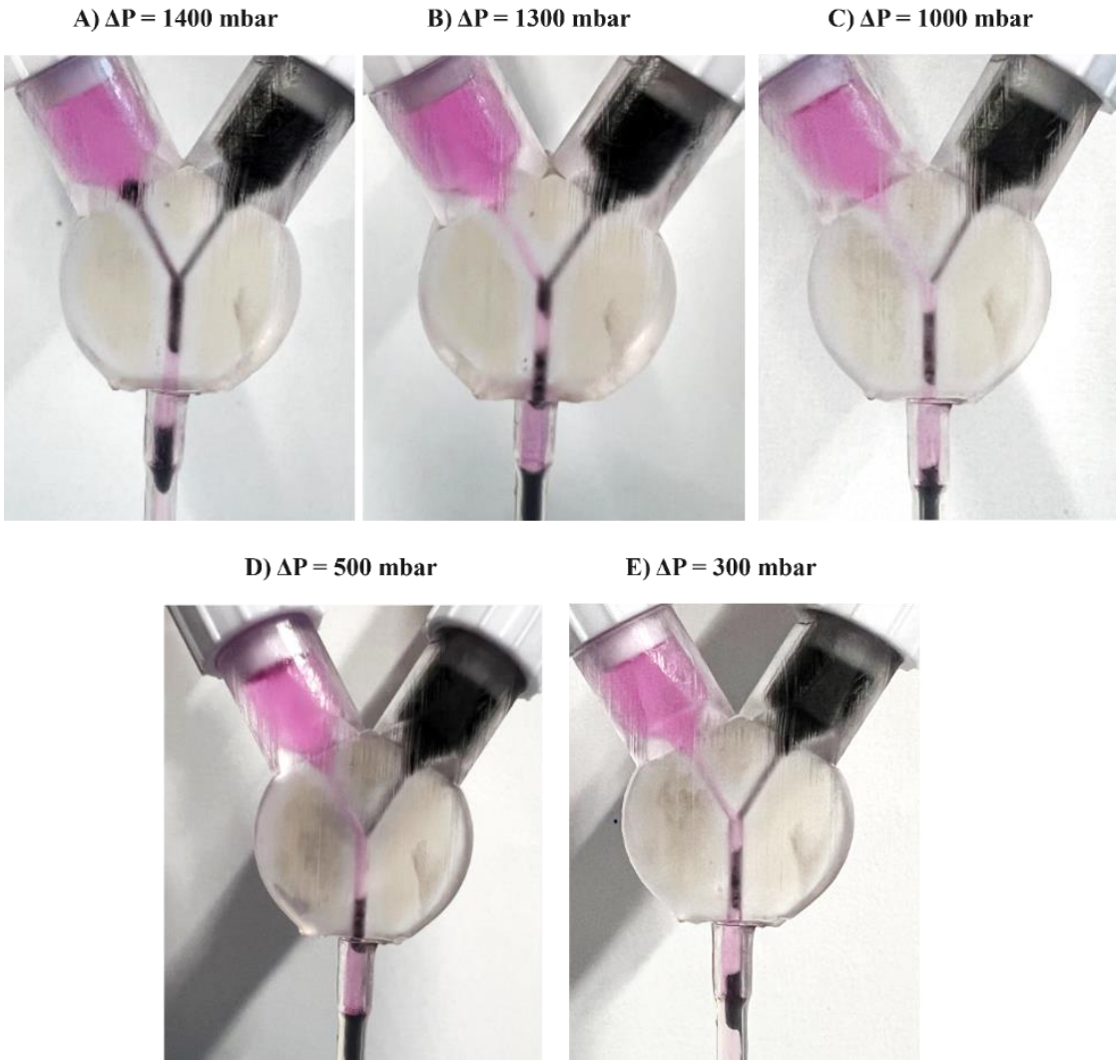

Figure 22. The flow of 30 % w/w Pluronic with switching of 30 s with P_{flow} 2000 mbar and ΔP ranging from 1400 mbar to 300 mbar.

2.2.6. Multimaterial Extrusion Printing and In-Situ Crosslinking of monofilament PluDA Fibers

Stable PluDA fibers could be generated by extrusion of PluDA inks and covalently crosslinking of the printed fiber via UV light exposure as it passes through a silicone tube attached to the nozzle outlet.[3] A customized holder held the silicone tube vertically and directed the curing light beam perpendicular to the tube at a fixed position for consistency of crosslinking **(Figure**

24A). The crosslinking of the PluDA 23.1 % w/w ink inside the tube increased the required pressure for extruding fibers from 700 to 1500 mbar. Using a P_{flow} = 1700 mbar, we determined the minimum irradiance required to obtain fibers with sufficient mechanical stability for handling while remaining extrudable. An irradiance of 97 mW cm^{-2} (5 % power) led to sticky fibers while irradiances ≥ 147 mW cm^{-2} (30 % power) caused clogging in the tube. At irradiance of 115 mW cm^{-2} (10 % power) stable segmented fibers could be printed at a constant printing rate of 8.8 ± 0.5 mg min^{-1} within a time window of 10 – 60 min (**Figure 23**). The rate was determined by weighing the extruded material generated in the preceding 2.5 min or 5 min time interval. Note that the first data point includes a contribution from uncrosslinked PluDA in the pre-filled nozzle which was extruded when printing started. The extrusion process was carried out using a P_{flow} = 1700 mbar, tube length = 4 cm, UV irradiance = 115 mW cm^{-2} (10 % power setting), and t_{switch} = 30 s. The printing rate of 8.8 ± 0.5 mg min^{-1} was constant during 10 – 60 min time window. In the initial phase of printing (< 10 min), the print rate decreased with time before stabilizing, and beyond 60 min the print rate declined.

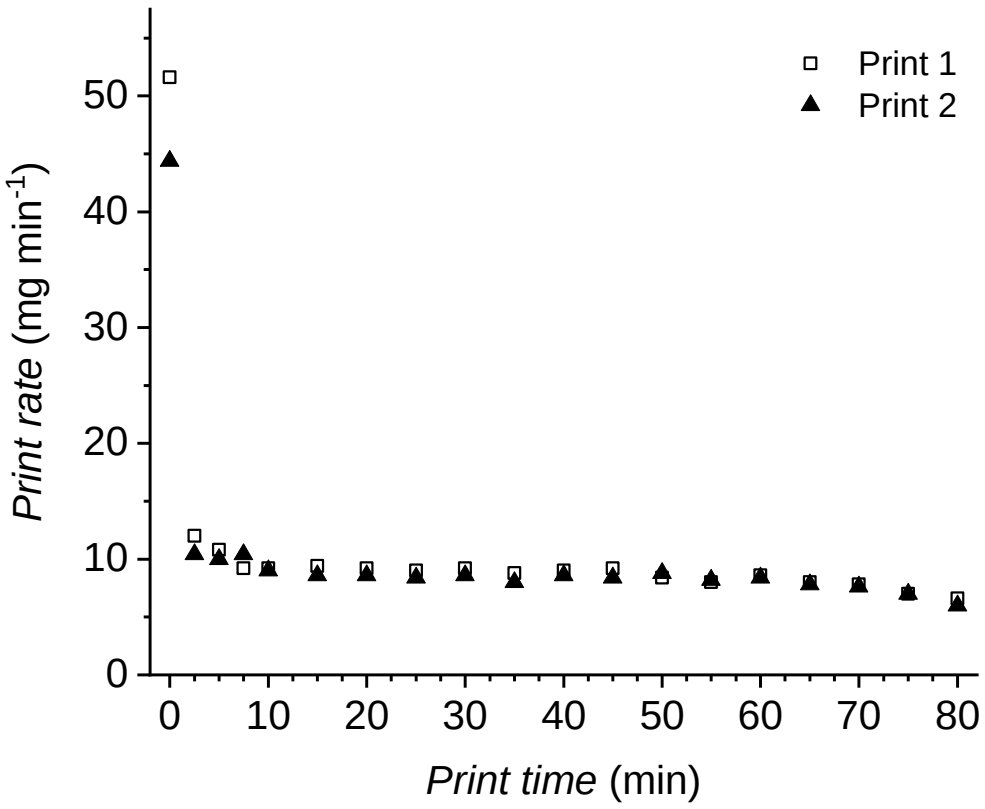

Figure 23. Print rate over time for two independent printing runs (N = 2).

The backflow of PluDA in the static channel, which materialized as an absent or a shorter first segment after switching, was corrected by applying pressure to the static channel, P_{static}, of 1200 mbar. A segmented fiber printed under these conditions is shown in **Figure 24B.**

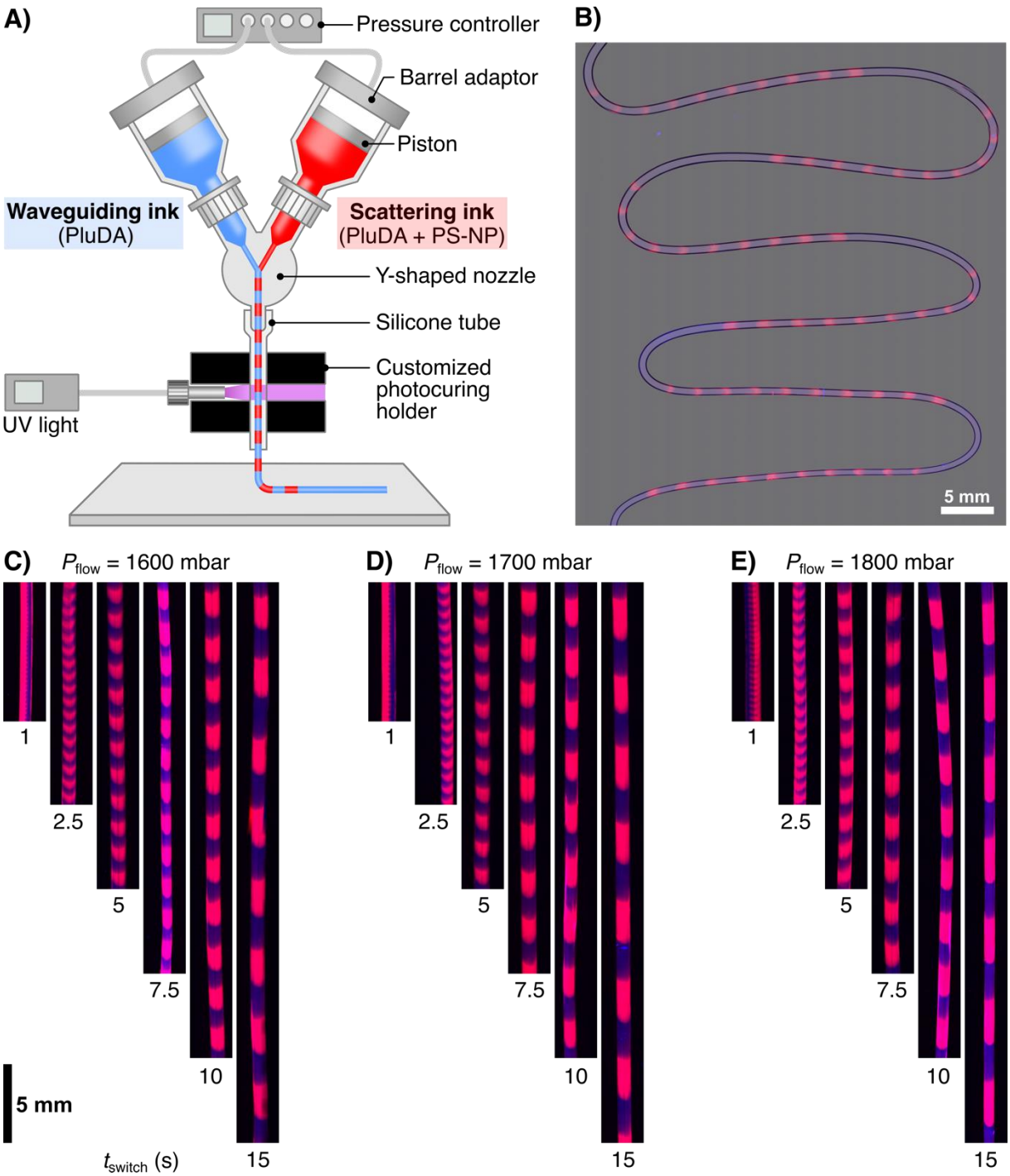

Figure 24. A) Setup for multimaterial printing and in situ photocrosslinking of the extruded fibers. B) Image of a printed fiber. The scattering zones were labelled by adding fluorescent particles to the scattering ink. The image is an overlay of the brightfield image, the red fluorescence capturing particle fluorescence, and the blue channel capturing autofluorescence of

the blank PluDA hydrogel. **C) – E)** Fluorescence images of fibers printed at different P_{flow} and t_{switch} values and constant P_{static} = 1200 mbar. Images are an overlay of the red and blue fluorescence channels. The scale bar in C) also applies to D) and E).

We then determined the shortest printable segment length, i.e. the spatial resolution of the printing method, by printing fibers at increasingly shorter switching times. At printing pressures, P_{flow} = 1600 and P_{static} = 1200 mbar, alternating segments of lengths between 2.2 and 0.4 mm were obtained using switching times between 15 and 2.5 s (**Figure 24C**). **Figure 25** shows the quantification of the segment lengths of fibers presented in **Figures 24C-E**. By increasing P_{flow} to 1700 and 1800 mbar, slightly longer segments were obtained, i.e. 2.6 ± 0.1 mm and 2.9 ± 0.1 mm respectively at 15 s switching time. These length scales are comparable to multimaterial printing with silicones, in which the minimum segment lengths also approach the diameter of the thread.[1] **Figure 26** demonstrates an example of how the segment lengths of the printed fiber were measured using Python. The fiber was printed under the conditions P_{static} = 1200 mbar, P_{flow} = 1600 mbar and t_{switch} =15 s. The corresponding fluorescence intensity profile, analyzed with Python, includes baseline fits (orange lines) and full-width at half-maximum (FWHM) lines (green lines), which were used to accurately determine the scattering and waveguiding segment lengths. This approach provided a systematic and precise method for segment length quantification.

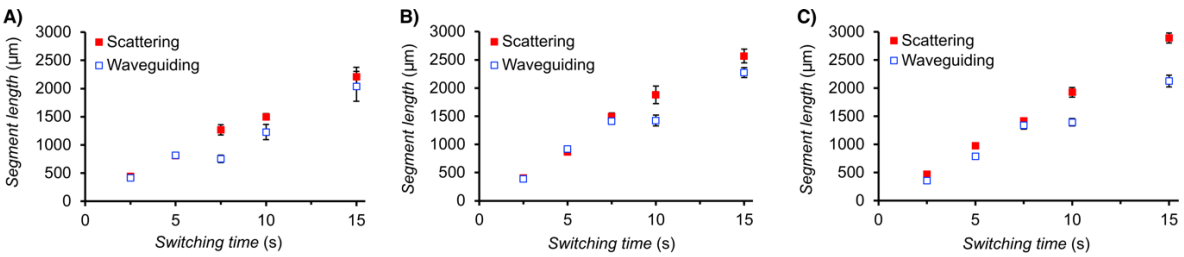

Figure 25. Quantification of segment lengths as a function of switching time printed at P_{flow} of A) 1600 mbar, B) 1700 mbar, and C) 1800 mbar, with P_{static} = 1200 mbar. For each data point, 10 segments were analyzed for both waveguiding and scattering inks and shown as the mean ± s.d. Shorter than expected waveguiding lengths were observed at longer switching times. The reason cannot be explained at this point.

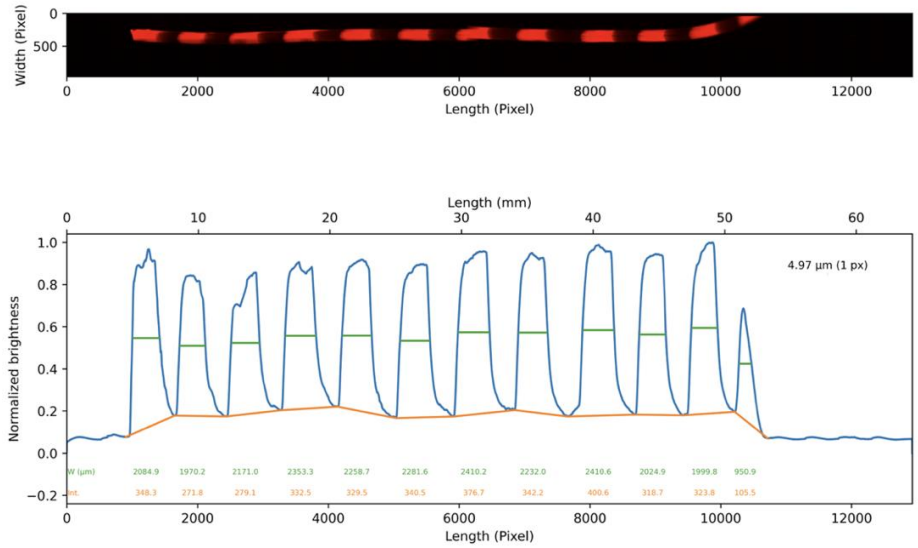

Figure 26. Segmented fiber printed at P_{static} = 1200 mbar, P_{flow} = 1600 mbar and t_{switch} = 15 s, and its corresponding fluorescence intensity profile generated with Python.

After characterizing the extrusion printing of PluDA 23.1% w/w and achieving stable fibers using PluDA with Irgacure as a photoinitiator and UV crosslinking, we proceeded to print PluDA at 30% w/w and replaced the scattering ink with plasmonic ink by incorporating AuNRs. An initial screening experiment to adjust the light intensity for crosslinking was performed by printing fibers with the 30% w/w waveguiding ink at pressures between 1500 and 2500 mbar and light irradiances between 78 mW cm^{-2} and 115 mW cm^{-2} (1 % to 10 % power). The printability of the fibers was assessed by visual inspection and the resulting printability window is represented in **Figure 27**. The in situ UV crosslinking in the silicone tube decelerated the flow of the ink. At pressures below 2200 mbar and UV irradiance of 87 mW cm^{-2} (3% power), continuous flow was observed, but the extrusion rate was slow (< 1 mm per minute) and clogging within the silicone tube occurred after 15 minutes printing. At pressure <2200 mbar and UV irradiance < 87 mW cm^{-2}, the filament was not fully crosslinked and had a sticky appearance. The best printing conditions were found at a pressure of 2300 mbar and UV irradiances of 90 - 97 mW cm^{-2} (4-5% power) , where stable, crosslinked fibers were successfully extruded. The flow rate in this pressure range was 1.3 mm min^{-1}. Fibers printed at 2500 mbar also rendered mechanically stable filaments at UV intensity > 100 mW cm^{-2} (6-7 % power). The flow rate under these conditions was 1.4 - 1.5 mm min^{-1}. Intensities above 115 mW cm^{-2} resulted in clogging within the silicone tube, whereas intensities below 5% rendered sticky fibers. In summary, fibers printed at high pressure require higher light intensity to achieve the necessary exposure dose that guarantees mechanical stability. In contrast, printing at too low pressure led

to clogging of the nozzle because of the high viscosity reached by the crosslinked hydrogel as it passes through the exposure zone. Stable fibers were printed at intermediate pressures and intensities, as revealed in the printing window in **Figure 27.** The results highlight the critical balance between extrusion pressure and UV intensity necessary to produce filaments without operational issues such as clogging or incomplete crosslinking.

To estimate the maximum flow rate that allows full crosslinking of the fiber as it passes through the silicon tube at a given exposure intensity, the stability of fibers printed at 2300 mbar and illuminated at 4 and 5 % power and of fibers printed at 2500 mbar and illuminated at 7 and 8 % intensity, was assessed by quantifying the polymer fraction of the fiber after immersion in 10 mL MiliQ water for 24 h. **Table 6** shows the polymer fraction of fibers as estimated by weighting of the fiber before and after immersion. Fibers printed at 2500 mbar and exposed to 103 – 108 mW cm^{-2} (7-8% power) retained ca. 70% gel fraction, while fibers printed at 2300 mbar and exposed to 90 – 97 mW cm^{-2} (4-5% power) retained ca. 61% of gel fraction after immersion. This indicates a higher crosslinking of the Pluronic chains in the 2500 mbar extruded fibers. Subsequent experiments were performed using printing pressures of 2500 mbar and a UV power of 7%.

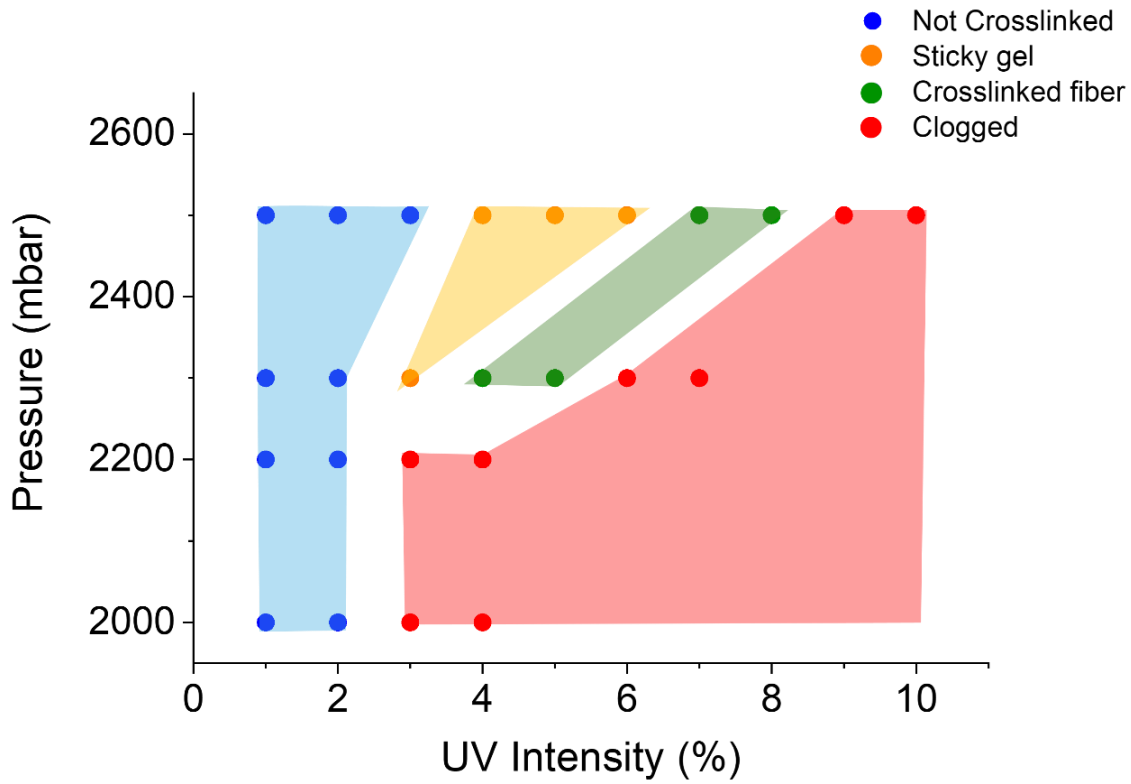

Figure 27. Printing window for 30 % w/w PluDA inks. The printability was assessed by qualitative analysis of extruded crosslinked fibers.

Table 6. Gel fraction measurements of crosslinked samples printed at different conditions.

Pressure (mbar)	UV intensity (%)	Gel fraction
2300	4	61.41 ± 1.75
2300	5	61.34 ± 1.42
2500	7	69.95 ± 0.14
2500	8	70.02 ± 1.03

We further investigated the influence of P_{static} on segment length and tailing behavior. Segmented fibers were printed at P_{flow} of 2500 mbar and t_{switch} of 15 s while P_{static} increased from 1500 to 2400 mbar with UV intensity of 7 %. To visualize the profile of the interface between the two inks, crimson fluorescence particles were added to one of the inks. The corresponding fluorescence images of the fibers are presented in **Figures 28B-F**. **Figure 28A** presents the normalized fluorescence intensity profiles along the fiber length for fibers printed at ΔP of 100, 300, 500, 800, and 1000 mbar. The transition length, defined as the distance over which the intensity decreases from 90% to 10% of its peak value, was quantified to evaluate the sharpness of segment interfaces. At lower ΔP values (100 and 300 mbar), poorly defined segments were observed due to co-extrusion of both inks. For ΔP=100 mbar, this co-extrusion resulted in a Janus-like fiber morphology where both inks flowed simultaneously, producing blurred segment boundaries with a long transition length of approximately 650 µm. At ΔP = 300mbar, the segments became more distinct but still exhibited co-extrusion, yielding a transition length of 546.34 µm.

As ΔP increased, the transition lengths decreased and sharper segment interfaces were obtained. At ΔP=500 mbar, the transition length was 491.88 µm, and at ΔP=800mbar, it was 585.04 µm. However, at ΔP=1000 mbar, although the transitions remain sharp (transition length of 403.11 µm), slight irregularities in segment length suggest potential negative effects from over-pressurization. These findings demonstrate that the ΔP range between 500 and 800 mbar provides uniform segment lengths with sharper interfaces. Lower ΔP values lead to co-extrusion of both inks, while excessively high ΔP induces extrusion irregularities and compromises segment uniformity.

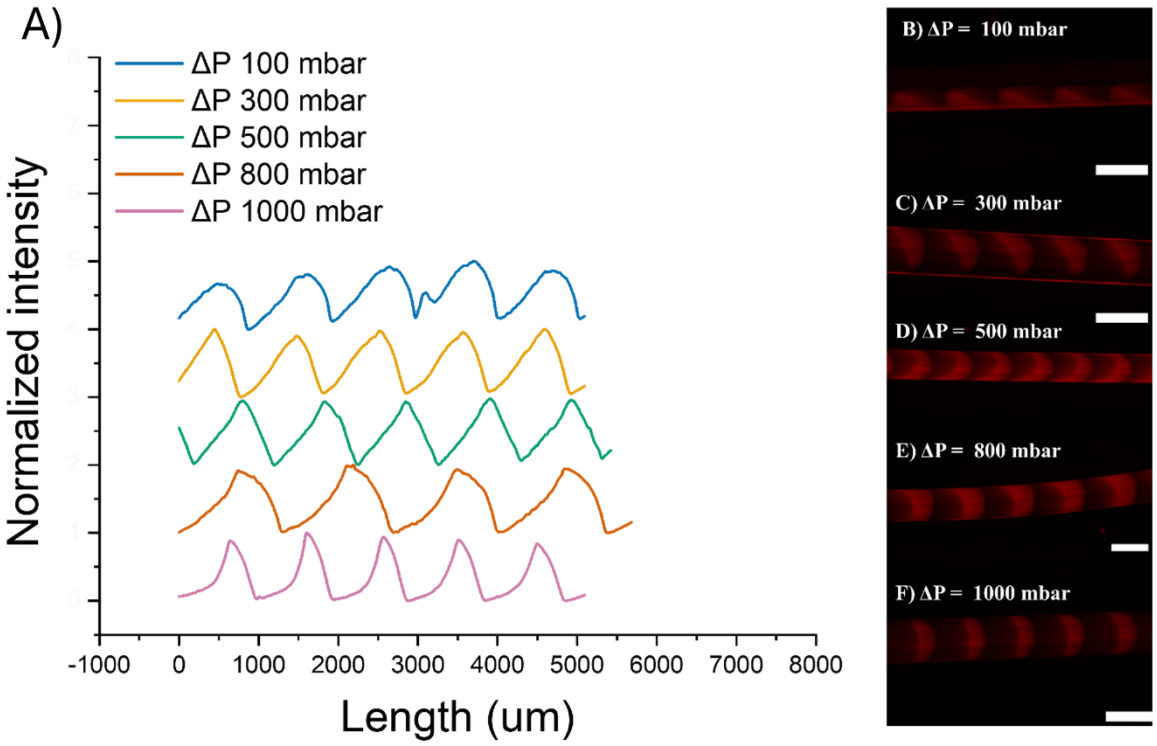

Figure 28. A) Analysis of the segment lengths in fibers printed with varying P_{static} between 1500 and 2400 mbar and a P_{flow} of 2500 mbar. The corresponding ΔP ranged from 100 to 1000 mbar. A t_{switch} of 15 was used in the experiment. B-F) The fluorescence images of the fibers are shown on the right. **C**rimson fluorophore (red) was added to the ink to allow imaging. The scale bar corresponds to 1 mm.

With these screening experiments, the printing parameters to obtain stable fibers with 30% w/w Pluronic hydrogels containing multimaterial segments of controlled length between 2 and 5 mm were established: P_{flow} = 2500 mbar, UV intensity = 7%, ΔP = 500 mbar and t_{switch} between 45 s and 135 s. Using these conditions, segmented Pluronic fibers with 2 mm and 5 mm length segments were printed **(Figures 29 A-D)**. The samples with 5 mm and 2 mm plasmonic segments were used to quantify the attenuation of light by the AuNRs and the cumulative effects of light absorption and heat generation (**Section 4.2.2**). The sample with multiple 2 mm segments separated by 2 mm waveguiding spaces allowed us to study the propagation of light between discrete plasmonic areas and the distribution of heat generated in a multi-segment configuration (**Section 4.2.2**).

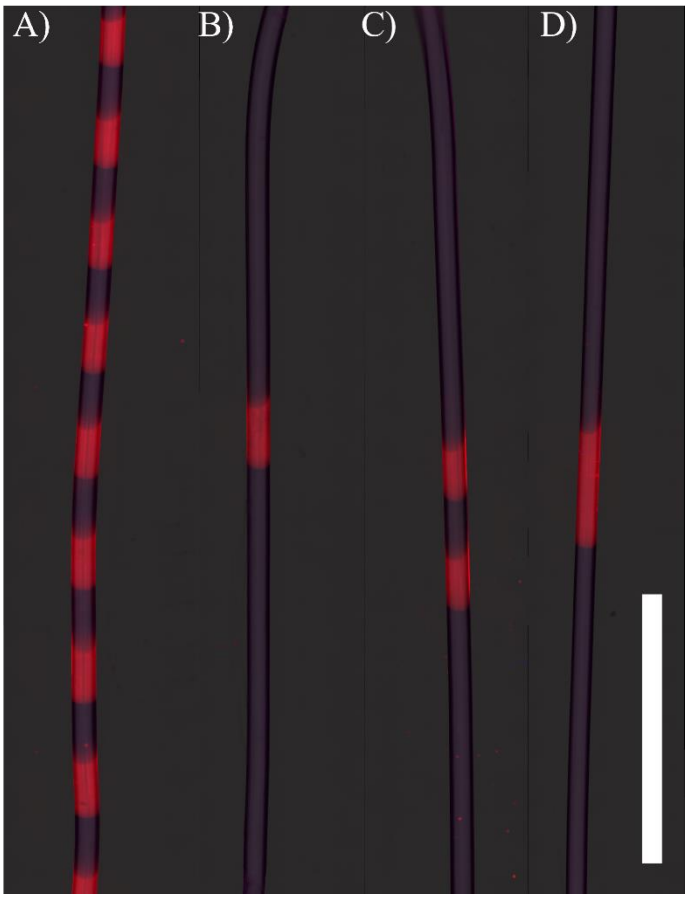

Figure 29. Fluorescence image of printed plasmonic fibers with segments of different lengths. The red color corresponds to plasmonic segments containing Crimson fluorospheres. A) Printed fiber obtained with t_{switch}= 45 seconds, which resulted in segments of 2 mm length. B, C) Segmented fibers with one or two plasmonic segments of 2 mm length C) Fiber with one 5 mm segment printed using a t_{switch} = 113 seconds. Scale bar corresponds to 10 mm and applies to all images.

These results demonstrate the possibility to generate optical waveguides with mm-sized segments containing plasmonic nanoparticles. The possibility of applying these fibers for local heating is described in **section 4.2.2**.

2.2.7. Multimaterial Extrusion Printing and In-Situ Crosslinking of core-cladding PluDA Fibers

To print core-cladding fibers, we adapted the nozzle design from Raymond et al.[147], who demonstrated co-extrusion printing of core-shell filaments and combined it with our previously used multimaterial nozzle allowing extrusion and switching between two core inks. The nozzle had 2 inlets for the core and 2 outlets for the shell where only one was used for extrusion. Each

inlet had a 500 µm inlet diameter and a 1 mm outlet diameter and a junction angle of 60 ° with a wall thickness of 250 µm (**Figure 30A,B**). The nozzle was fabricated by stereolithography (SLA) with a commercial acrylate-based resin (**Figure 30C,D**).

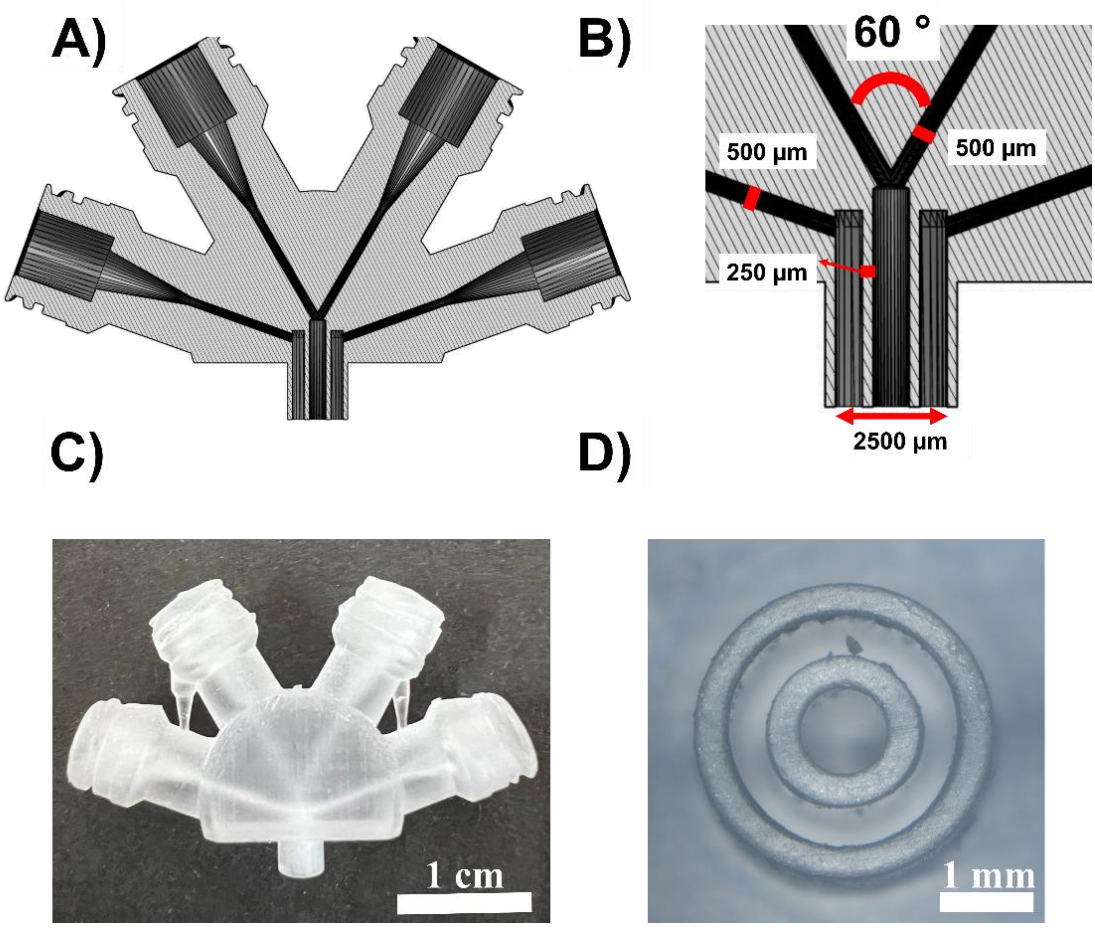

Figure 30. A,B) Geometry of the nozzle for printing segmented core-cladding fibers. C) Image of the SLA-printed nozzle. D) Cross-sectional view of the printed nozzle.

To visualize flow, we used 30% w/w Pluronic with black dye (0.5% w/w) and pararosaniline (0.06% w/w) as core inks. For the cladding, we utilized Pluronic at 23.1% w/w concentration to obtain RI contrast. The printing process was conducted at a temperature of 22.6 ± 0.5 °C. Consistent with previous experiments, 30% w/w Pluronic core inks required a minimum pressure of 1500 mbar to be extruded. 23.1% w/w Pluronic shell inks were extrudable at 900 mbar when co-extruded with the core. Lower pressures resulted in the extrusion of the core material only, without adequate extrusion of the cladding ink (**Figure 31**).

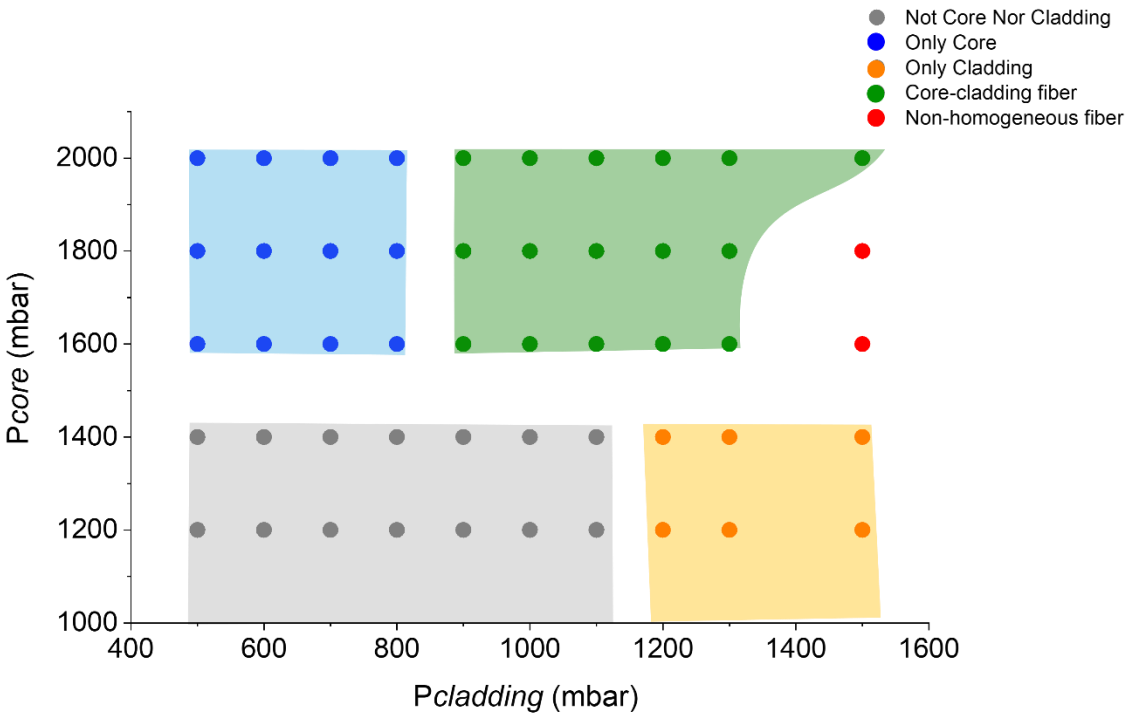

Figure 31. Printability window of extrusion printing of Pluronic 30 % w/w in core-cladding nozzle.

The pressure applied to the cladding ink, $P_{cladding}$, significantly influences the core diameter in segmented fibers (**Figure 32**). We define the core diameter ratio as the ratio of the extruded core diameter to the nozzle core diameter (1 mm). At pressures between 900 and 1100 mbar, the core diameter ratio is above 1, indicating that the extruded fiber diameter is larger than the nozzle diameter. This is due to the compression exerted by the core on the cladding. As $P_{cladding}$ increases, the core diameter ratio decreases. This behavior aligns with observations from previous research in coaxial extrusion[147], and is attributed to the rapid movement of the shell, which compresses the core and reduces its diameter. The core diameter ratio equals 1 at a $P_{cladding}$ of 1200 mbar. Increasing $P_{cladding}$ to 1300 mbar compresses the core and leads to a core diameter ratio of 0.7.

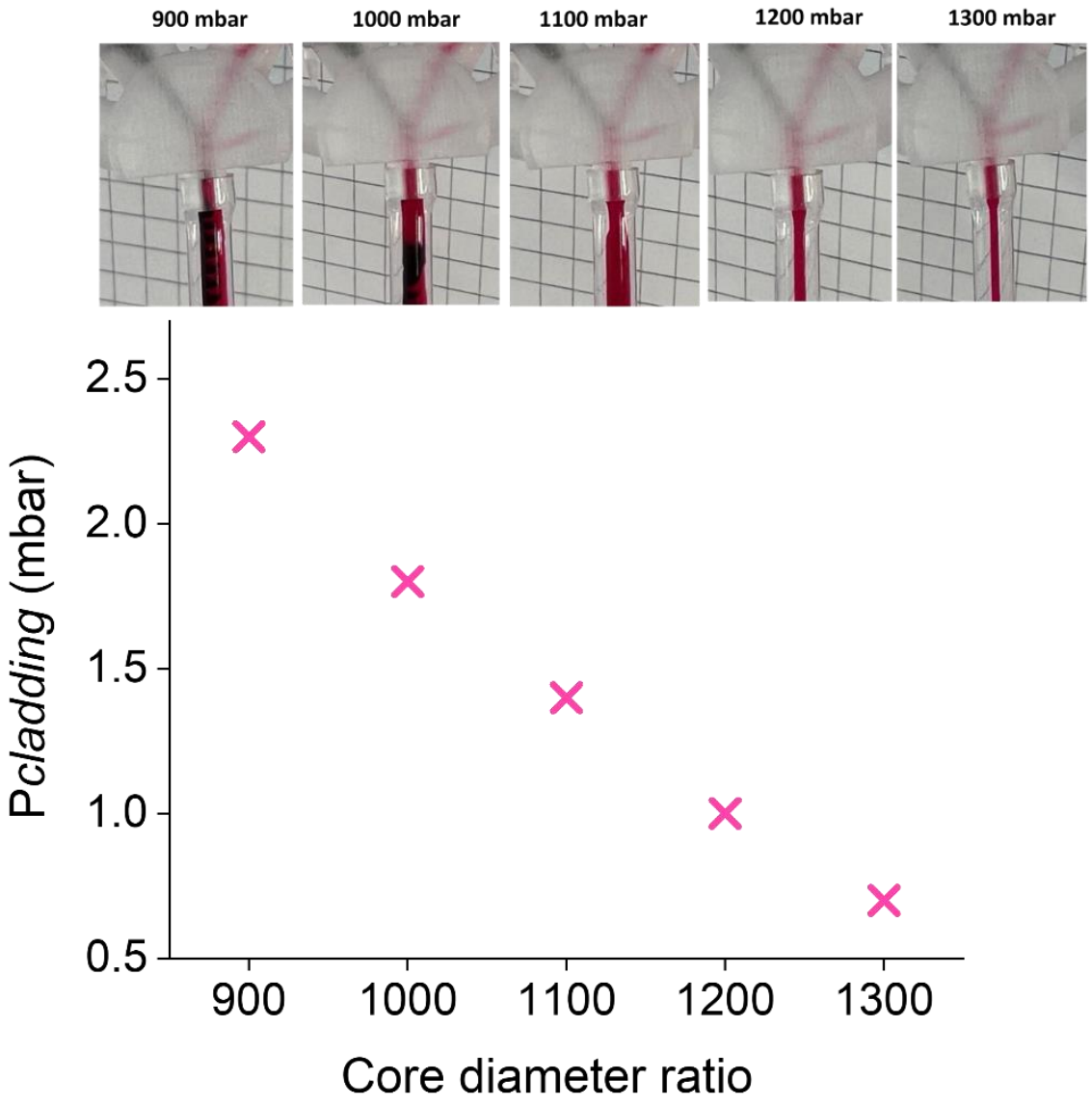

Figure 32. The core diameter ratio as a function of *P*cladding.

Core-cladding structures with segmented cores were successfully extruded at P_{flow}=1800 mbar applied to the core ink, a P_{static}= 1300 mbar alternating between the two core inlets, and a $P_{cladding}$ of 1200 mbar applied to the cladding (without crosslinking). By adjusting t_{switch} (10 s, 5 s, 2 s, 500 ms) core-cladding structures with segmented cores with variable lengths between 1.2 cm and 0.5 mm were extruded. For t_{switch} = 500 ms the two inks flowed in parallel without effective switching (**Figure 33**).

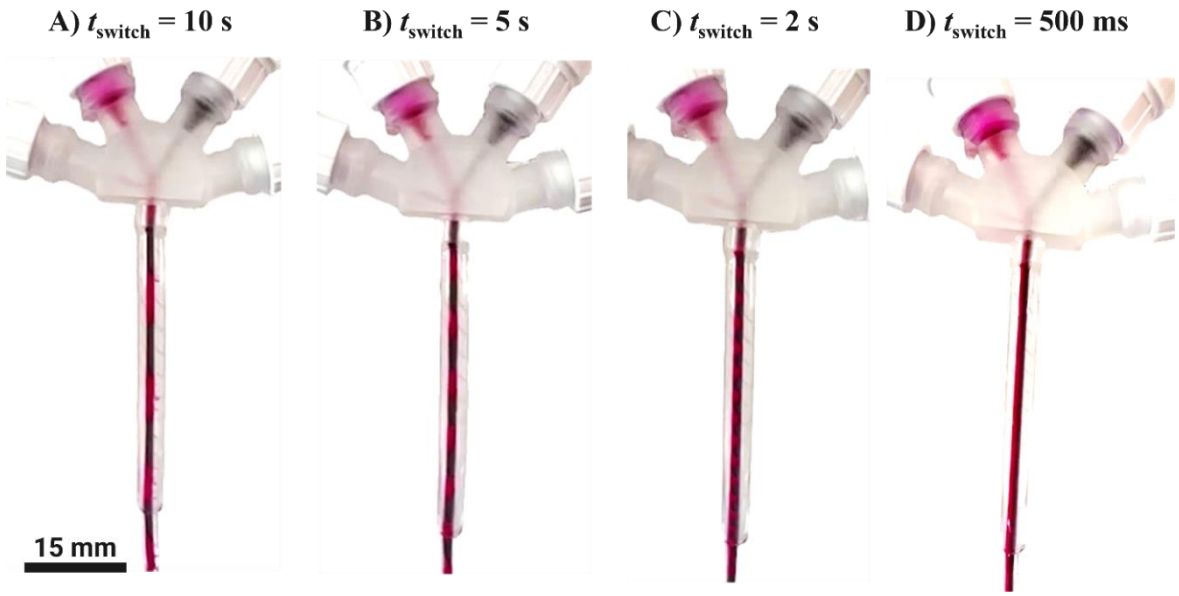

Figure 33. Snapshots of core-cladding segmented flow of Pluronic core (30% w/w) and cladding (23% w/w) inks using different switching times. The inks were stained with carbon black (0.5 % w/w) and pararosaniline (0.06 % w/w) for visualization in the core. P_{flow} = 1800 mbar, P_{static} = 1300 mbar $P_{cladding}$ = 1200 mbar. The scale bar applies to all images.

Once the extrusion conditions to obtain continuous core-cladding flow with segmented cores were established with Pluronic inks, the printing of crosslinked, plasmonic optical fibers was attempted using PluDA-based inks. For this purpose, a silicone tube with an inner diameter of 2.5 mm and a length of 4.5 cm was attached to the nozzle to allow crosslinking of the PluDA after extrusion. **Figure 34A,B** present the schematic representation of the printing setup and pressure profiles, and **Figure 34C** shows the actual implemented printing setup. **Table 7** presents the Printing parameters and the range of the values used.

Table 7. Printing parameters for extrusion printing of core-cladding waveguides

Printing parameters	**Value ranges**
Nozzle inlet diameter	500 µm
Nozzle outlet diameter	1000 µm
Nozzle cladding diameter	500 µm
Tube inner diameter	2.5 mm
P_{flow}	1800 – 2900 mbar
P_{static}	1500 – 2000 mbar
$P_{cladding}$	1500 - 2000 mbar
Switching time (t_{switch})	15 – 900 s
UV intensity	78 – 97 mW cm^{-2} (1% - 5 % power)

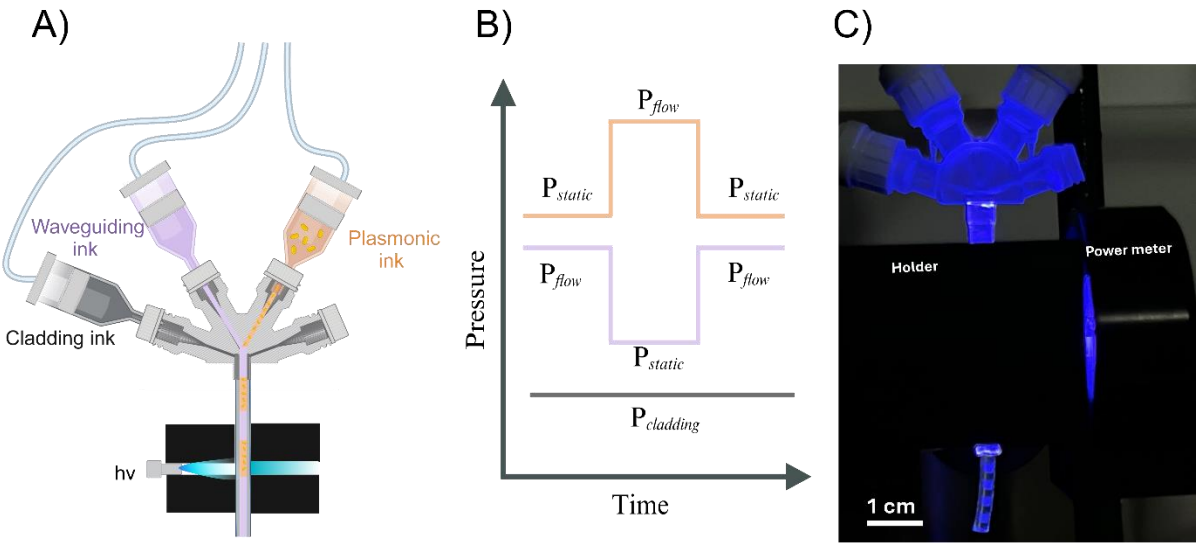

Figure 34. Schematic of the multi-material core-cladding extrusion printing setup. B) Schematic of the pressure profile for the segmented core-cladding printing. C) Image of extrusion printing setup with UV crosslinking.

Figure 35 illustrates the printability window for the extrusion of core-cladding fibers under the abovementioned conditions. Co-extrusion of core and cladding materials occurred at P_{core} between 2200 and 3000 mbar and $P_{cladding}$ between 1700 and 2000 mbar. Outside this range, various extrusion failures are observed: when P_{core} is 2400–3000 mbar and $P_{cladding}$ is below 1700 mbar, only the core material extrudes, while at $P_{cladding}$ of 1800–2100 mbar and P_{core} below 2200 mbar, the cladding material is extruded dominantly. Non-homogeneous fibers form when P_{core} is around 2400 mbar and $P_{cladding}$ is at 1500 mbar, indicating an imbalance in material flow rates. In the shaded region, where P_{core} is below 2400 mbar and $P_{cladding}$ is below 1700 mbar, slow flow rates lead to clogging in less than 5 minutes.

Using an irradiance of 97 mW cm^{-2} (5% power), stable core-cladding fibers with a segmented core were printed at a rate of 1.5 mm min^{-1} within a time window of 10 to 70 minutes. A P_{static} of 1900 mbar was used to correct the backflow of PluDA in the static channel. These optimized conditions rendered continuous, stable, core-cladding fibers with segmented cores. The gel fraction of the fiber was 69.2 ± 0.4 %.

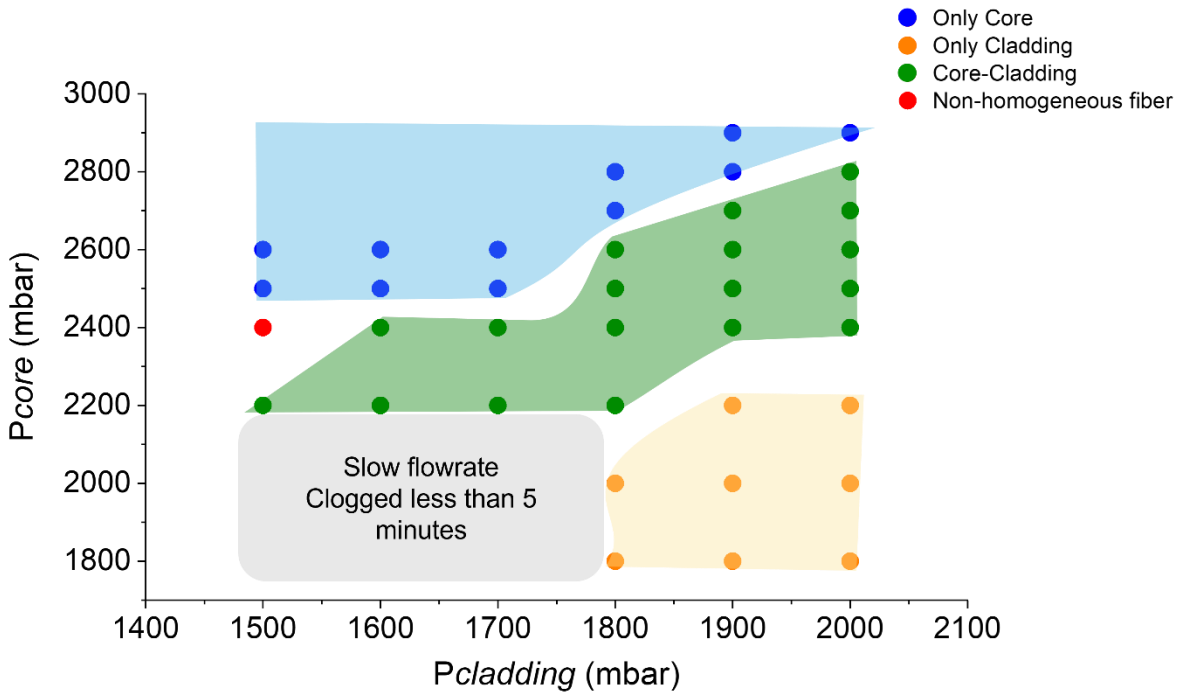

Figure 35. Printability window for extrusion printing of core-cladding PluDA in different Pcore and P cladding.

For a core flow pressure of 2400 mbar and a static pressure of 1900 mbar, various cladding pressures $P_{cladding}$ were tested to obtain fibers with different diameters of core and cladding. $\Delta P_{core\text{-}cladding}$ is defined as the difference between P_{core} and $P_{cladding}$. With increasing $\Delta P_{core\text{-}cladding}$ from 400 to 800 mbar, fibers with ≈ 2.5 mm overall thickness and variable core diameters between 0.69 ± 0.04 mm and 2.10 ± 0.09 mm and claddings between 0.88 ± 0.04 and 0.15 ± 0.02 were obtained (**Figure 36** and **Table 8**). The inverse relationship reflects the interplay between core and cladding flow rates, where higher pressure differences prioritize the core material's extrusion over the cladding. A $P_{flow,core}$ - $P_{flow,\ cladding}$ of 600 mbar was selected for further experiments, which gives a cladding thickness of 0.49 ± 0.05 mm and core diameters of 1.45 ± 0.12 mm.

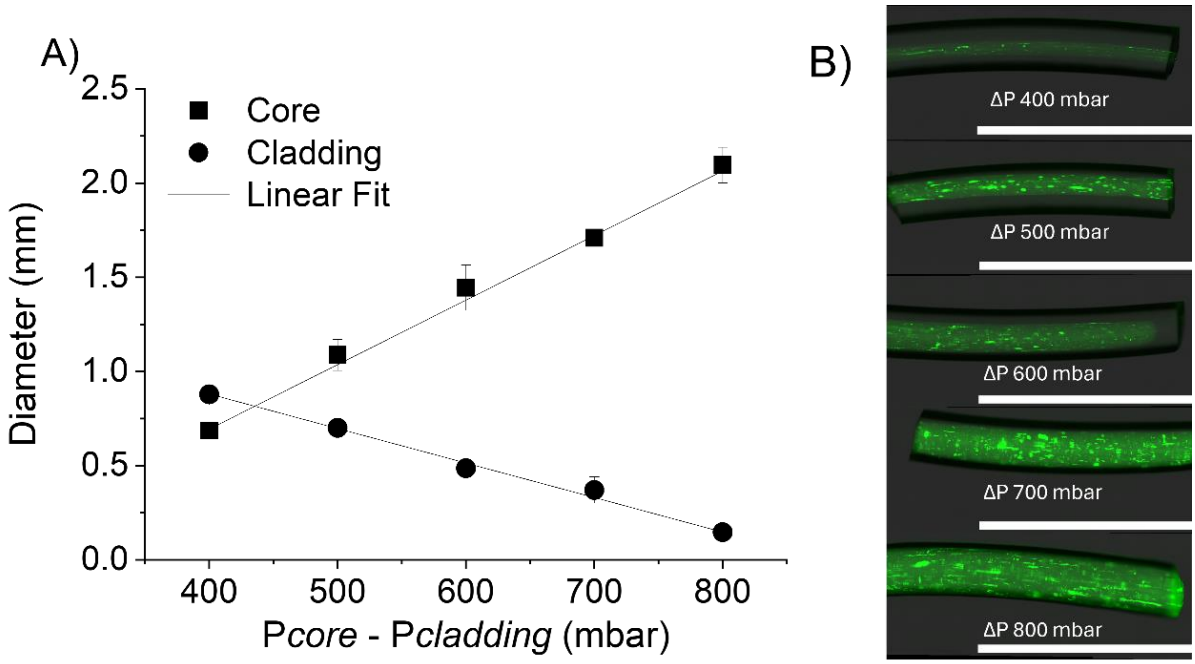

Figure 36. A) Plot showing the dependence of core diameter and cladding thickness on the ΔP between core and cladding including the linear fit. N= 3 B) Printed fibers with tunable core diameter with different pressures. Scale bar 10 mm.

Table 8. Values of the core diameter and cladding thickness in different pressure conditions. N = 3.

ΔP (mbar)	Average core diameter (mm)	Average cladding thickness (mm)
400	0.69 ± 0.04	0.88 ± 0.04
500	1.09 ± 0.08	0.70 ± 0.02
600	1.45 ± 0.12	0.49 ± 0.05
700	1.71 ± 0.03	0.37 ± 0.07
800	2.10 ± 0.09	0.15 ± 0.02

2.2.8. Characterization of Fiber Stability in Aqueous Conditions

The swelling behavior of printed core-cladding PluDA fibers was evaluated at room temperature (RT), 37°C, and 40°C for 24 hours in 5 mL of water (**Figure 37**). At RT, the fibers exhibited the highest swelling ratio, reaching approximately 350% after 2 hours, followed by a gradual decrease due to the loss of uncrosslinked PluDA.[135] At 37°C, the swelling ratio stabilized at

~200% after 2 hours and remained constant over the 24 hours. In contrast, at 40°C, the swelling ratio was lower and stabilized at ~100%.

This behavior is attributed to the thermosensitive nature of Pluronic diacrylate, a block copolymer with temperature-dependent hydrophilicity. At lower temperatures, the hydrophilic segments dominate, promoting water absorption and higher swelling ratios. As the temperature increases, the hydrophobic interactions among the polymer chains become more pronounced, reducing the water uptake capacity. At 40°C, the stronger hydrophobic association in Pluronic micelles likely restricts the polymer network's expansion, limiting water absorption. The differences in swelling ratios across temperatures highlight the balance between hydrophilic and hydrophobic interactions within the crosslinked polymer matrix, with higher temperatures suppressing the swelling due to enhanced hydrophobicity.

The fibers exhibited stability across all tested temperatures. No significant deformation or mechanical damage was observed. The chemically crosslinked polymer network formed during UV curing maintains structural integrity in the aqueous environment. The photothermal response of the fibers are tested in **Chapter 4**.

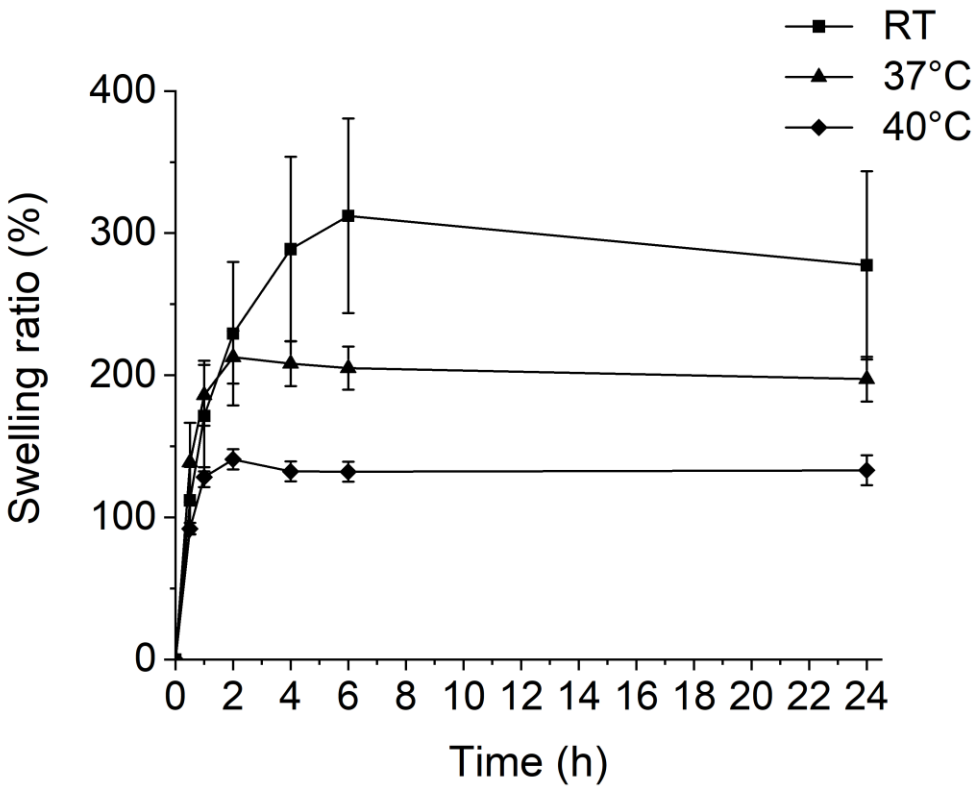

Figure 37. Swelling behavior of printed core-cladding fibers over 24 hours at RT, 37 °C and 40 °C. N=3

2.3. Conclusive remarks

This chapter demonstrates the potential of Pluronic-based hydrogels for multimaterial fiber printing, offering the possibility to print fibers with tunable and localized optical properties at sub-millimeter spatial resolution. The shear-thinning behavior and thermoresponsive gelation of Pluronic F-127, along with its chemical modification to PluDA, allow for controlled extrusion processing and post-printing stabilization. The tunable refractive index (RI) of PluDA hydrogels, ranging from 1.366 at 23.1% w/w to 1.38 at 33.3 % w/w, provides a suitable range for the fabrication of core-cladding fibers with RI contrast. In this work, these properties establish PluDA hydrogels as promising candidates for use in flexible optical waveguides.

Increasing the Pluronic concentration from 23% to 33.3% w/w influenced yield stress (from 0.62 kPa to 2.02 kPa) and the required extrusion pressures (from 700 mbar to 3000 mbar), and affected process stability and material switching behavior. Successful multimaterial switching achieved at optimized concentrations (23.1% and 30% w/w), enabled the fabrication of sub-millimeter multimaterial fiber segments with resolution comparable to reported extrusion printed silicone-based fibers . UV crosslinking was successfully integrated in the multimaterial extrusion printing process, allowing for the continuous fabrication of chemically crosslinked hydrogel-based optical fibers. The degree of crosslinking, influenced by UV power, directly affected the material's flow properties and printability of the fiber. By optimizing UV exposure parameters, gel stability was ensured while preserving the optical and mechanical properties of the fibers. The fibers retain their structural integrity at room temperature and elevated temperatures (37 °C and 40 °C), making them suitable for subsequent photothermal applications.

This research introduces a scalable and reproducible fabrication strategy for hydrogel-based multimaterial fibers, integrating extrusion-based multimaterial printing, customized nozzle designs, and UV crosslinking to create multifunctional fiber structures. This method could be extended to incorporate additional cladding layers by designing advanced nozzles. Preliminary work in this thesis utilizing three-layer nozzles demonstrated successful fabrication of segmented core-shell-shell structures.

The printed segmented fibers offer a soft alternative to hard materials reported for side-emitting biomedical waveguides. The fibers are printed in minutes and the tailored emission is achieved in a continuous process suitable for manufacturing. In contrast, hard waveguides with tailored side-emission profiles are produced using post-processing steps such as pulsed laser treatment to pattern microcavities in the core or to introduce sidewall patterns/windows in the cladding[61], focused ion beam milling of windows in a reflective layer, heat treatment to introduce microbubbles in the core[103], coating with scattering particles, or etching/polishing to control

surface roughness or cladding thickness. None of these processes are applicable to hydrogel waveguides. Tapered hydrogel slab waveguides have been generated by molding, and side-emitting hydrogel optical fibers have been prepared by manual pipetting of PEG-based precursor solutions containing scatterers into a vertical cylindrical mold to generate mm-scale segments with scattering ability. Our approach offers automated, continuous manufacturing of optical fibers with sub-millimeter segment lengths where segment length and position are simply programmed using the pressure controller. This gives unprecedented flexibility in tailoring the side emission profile. The in situ curing directly generates stable fibers that do not require postprocessing treatments for further stabilization. The fabrication process is amenable to including other types of scattering particles (e.g. with different size or refractive index) which could offer further options for tuning side-emission profiles. We also present PluDA as a valuable addition to the suite of soft materials suitable for multimaterial printing.

In the following chapters, we explore the integration of functional additives, including scatterers and plasmonic nanoparticles, to enable controlled heat and light delivery.

3. Light emission from segmented optical waveguides

3.1. Introduction

Side-emitting optical fibers are designed to emit light along their length, illuminating larger areas than end-emitting fibers, which are restricted to point-specific lighting. A variety of strategies have been employed to achieve side emission. Among them, introducing scatterers into the fiber core has been explored using different materials and techniques. For example, side emission in polyethersulfone (PES) optical fibers has been controlled by generating microbubble cavities through thermal treatment.[103] These bubbles, formed within the fiber matrix at a controlled distance from the surface, act as scattering centers, with attenuation lengths tunable between 5.4 and 0.2 cm depending on processing conditions. Similarly, poly(ethylene glycol) dimethacrylate (PEGDMA) hydrogel waveguides containing polystyrene (PS) and TiO_2 particles, allow for side scattering behavior based on particle size and concentration gradients. These approaches demonstrated that manipulating the distribution and size of scatterers enables control over light outcoupling and side emission.

The described methods lead to exponential light loss along the fiber length, often requiring additional light sources at both fiber ends to compensate for attenuation. In the reported works, the side emission is restricted to fiber lengths shorter than 3 mm. In this chapter, the side-emission profile of printed optical fibers containing scattering segments is characerized. We investigate whether tailored side-emission profiles can be achieved by fabricating fibers with sequential waveguiding and scattering segments of varying lengths. Specifically, we designed segmented fibers capable of outcoupling 60% of 520 nm light over a 3 cm length. Furthermore, we assess the functional performance of these fibers by embedding them in a gelatin film containing fluorescent nanoparticles to evaluate their ability to activate photophysical processes.

3.2. Results and discussion

3.2.1. Characterization of side-emission profiles from printed fibers

To test the side emission from the printed segmented fibers, a 520 nm laser was incoupled to the fiber end. This wavelength was selected because green light is used for photodynamic therapy (PDT)[6] and optogenetics.[31] We first tested the optical loss of waveguides without scattering segments. **Figure 38** shows the autofluorescence signal of a printed waveguiding fiber with PluDA 23.1% w/w, which reflects the light intensity decay as it travels through the fiber length.

An exponential fit of the intensity profile along the section from 25 mm to 175 mm yields an attenuation coefficient of 0.0845 cm^{-1} ('-b' in the fitting parameters from the figure above). This corresponds to an optical loss of 0.37 dB cm^{-1}. The optical loss of the samples was calculated. For a waveguide, $P = P_0 e^{-\alpha z}$ where P_0 is the power at point zero in the fiber, a is the attenuation coefficient, and P is the power remaining inside the fiber as a function of distance traveled in the propagation direction (z). Rearranging gives:

$$ln\left(\frac{P}{P_0}\right) = -\alpha z \quad (1)$$

Optical loss (L) in dB per unit length is given by:

$$L = \frac{10log_{10}\left({}^{P}/_{P_0}\right)}{z} = \frac{10log_{10}(e)}{z} \cdot ln\left(\frac{P}{P_0}\right) \quad (2)$$

Substituting (1) into (2) gives:

$$L = -10log_{10}(e) \cdot \alpha \approx -4.3\alpha \quad (3)$$

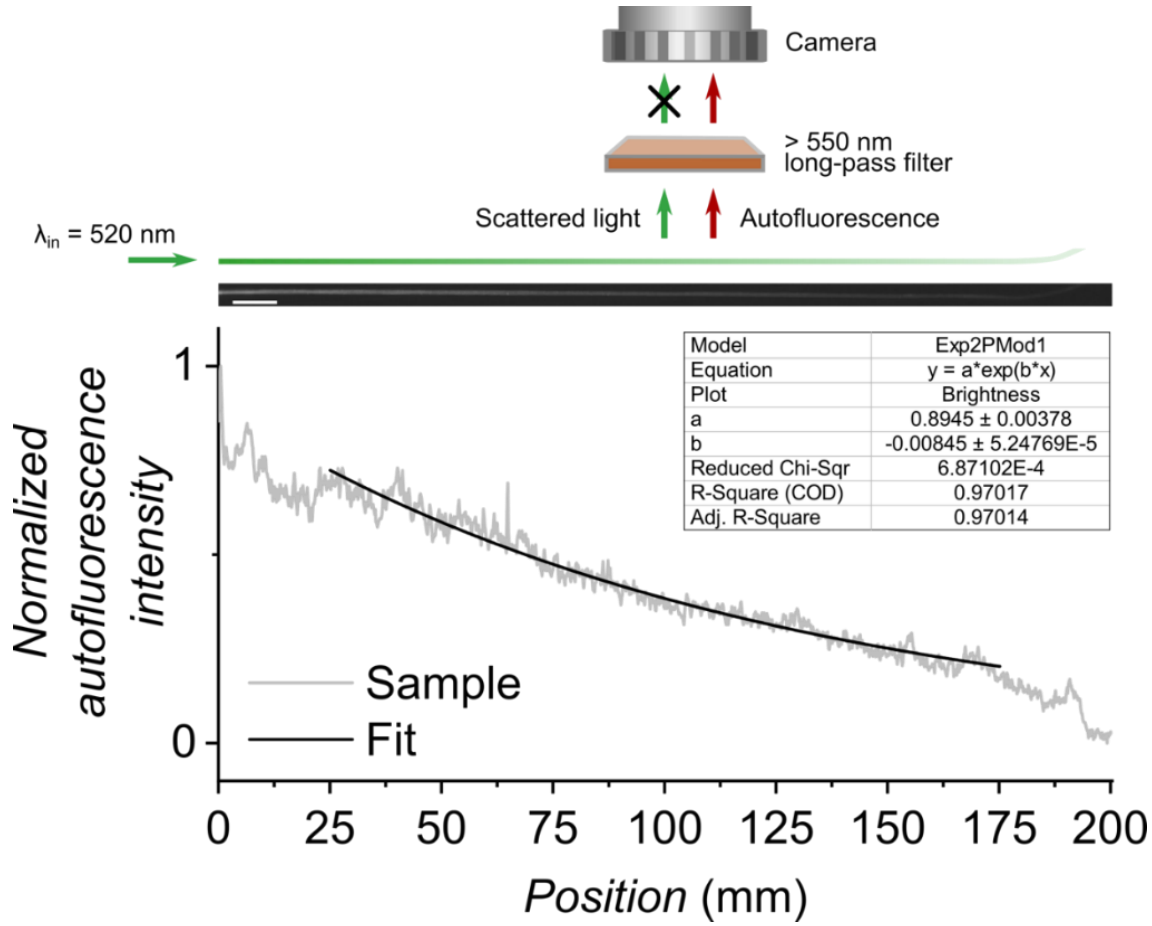

Figure 38. Autofluorecsnece schematic, image and corresponding intensity profile for a waveguiding fiber. Scale bar = 1 cm.

We then tested the side-emission from a printed fiber containing waveguiding ink intercalated with a single scattering element of ca. 3 cm length (**Figure 39**). Under these imaging conditions scattering from the waveguiding segment is not observed while a high scattered light intensity is observed from the scattering segment. This highlights the contrasting optical properties of the two segments and confirms the suitability of multimaterial printing method to create waveguides that outcouple light at an intended zone. The image in **Figure 39** corresponds to Sample 1 in the plot. The white triangle shows the transition between the waveguiding and the scattering material, with negligible side-emission intensity observed from the waveguiding portion to the left of the arrow. The three side-emission profiles were aligned in the plot by arbitrarily setting the z = 0 positions to be the points at which the side-emission intensity reached 0.5. The exponential fit of the intensity profiles from the three fibers (between 10 and 25 mm) gives an optical loss of 4.5 ± 0.5 dB cm^{-1} (av. ± s.d.; N = 3) (attenuation coefficient of 1.0 ± 0.11 cm^{-1}) calculated using Equation 3.

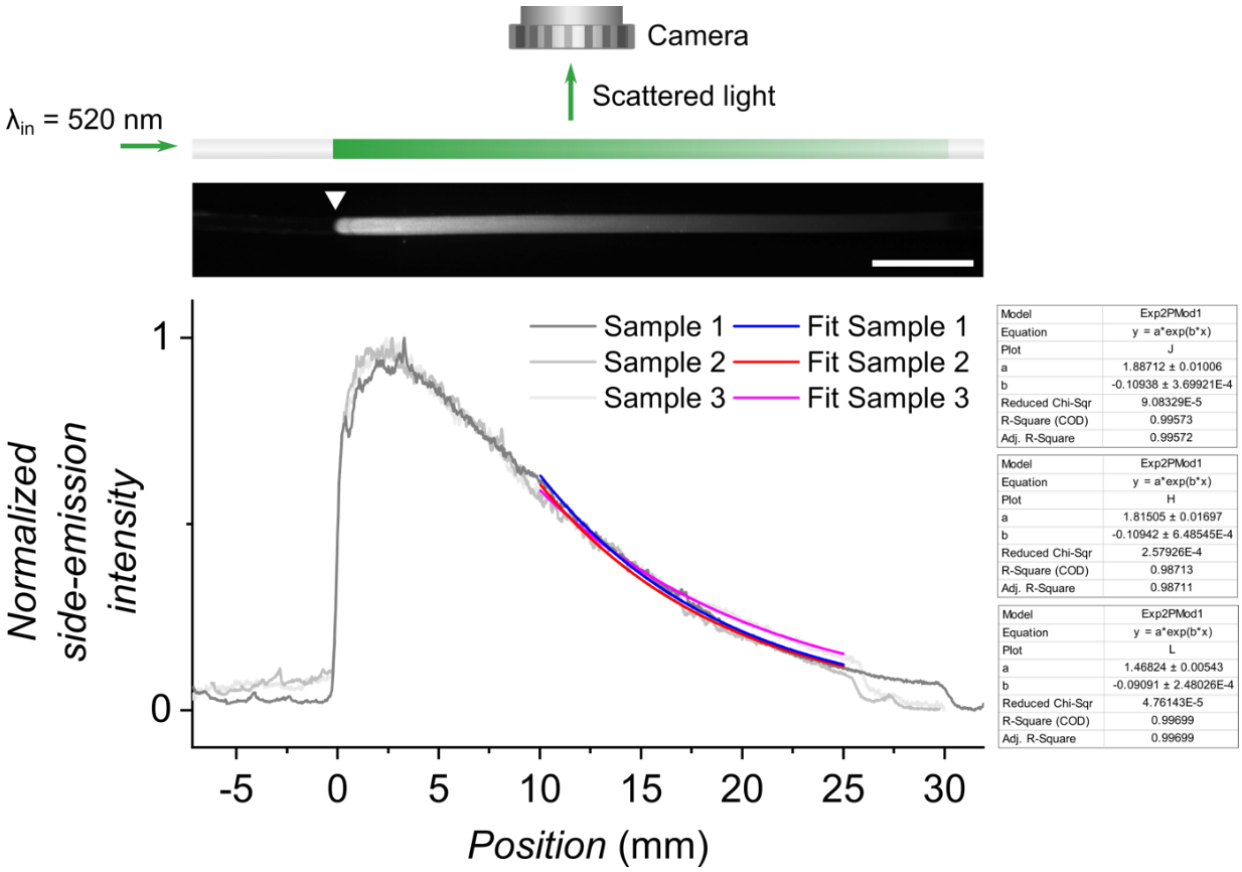

Figure 39. Image of scattered 520 nm light from a 3-cm scattering segment, and corresponding intensity profiles generated from three such fibers. Scale bar = 5 mm

We tested whether tailored side-emission profiles could be obtained by fabricating fibers with sequential waveguiding/scattering segments of varying lengths. We designed segmented fibers that could outcouple 60 % of 520-nm light over a 3-cm length. This length scale is representative of biomedical scenarios such as PDT of solid tumors or activation of optogenetically engineered cells within a biomaterial. To achieve uniform light outcoupling along the 3-cm length of the fiber, segment lengths were calculated to ensure equal light outcoupling from each segment. Based on the attenuation coefficient of 1.4 cm^{-1}, determined from the absorbance of PluDA (23.1% w/w) with 200-nm PS-NP (0.01% w/w) at 520 nm (**Table 9, Figure 40**), a total of 10 scattering segments with progressively increasing lengths were designed and evenly distributed along the fiber. For comparison, a single scattering segment measuring 6.6 mm would theoretically outcouple the same amount of light as the entire series of calculated segments.

Table 9. Scattering segment lengths and positions for the 10-segment fiber designed to outcouple 60 % of 520-nm light over 3 cm, using the attenuation coefficient of 1.4 cm^{-1} determined from Absorbance of PluDA 23.1% w/w plus 200-nm PS-NP (0.01% w/w) at 520 nm .

Segment #	Scattering start (mm)	Scattering end (mm)	Scattering length (mm)	Segment mid-point (mm)	Cumulative light outcoupled (%)
1	1.277	1.723	0.446	1.50	6
2	4.262	4.738	0.476	4.50	12
3	7.245	7.755	0.509	7.50	18
4	10.226	10.774	0.548	10.50	24
5	13.203	13.797	0.593	13.50	30
6	16.177	16.823	0.646	16.50	36
7	19.145	19.855	0.710	19.50	42
8	22.106	22.894	0.788	22.50	48
9	25.058	25.942	0.884	25.50	54
10	27.996	29.004	1.008	28.50	60

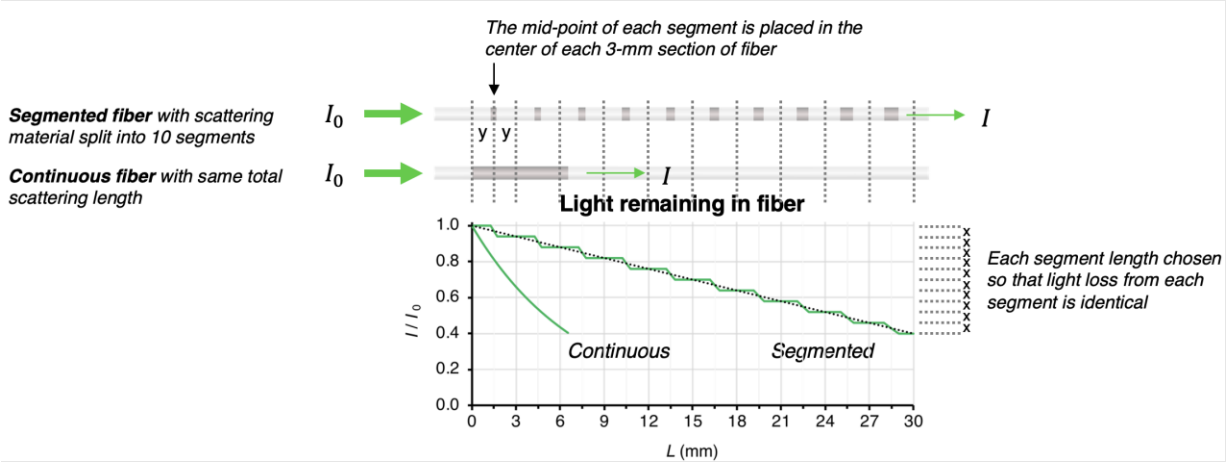

Figure 40. Targeted segmented fiber design (top) with the theoretical decay of light power within the fiber assuming exponential light loss by scattering only. A continuous scattering segment that would give the same amount of light loss is also shown (bottom). Input assumptions: 520 nm light, attenuation coefficient 1.4 cm^{-1} .

We then tried to print the fibers with distributed scattering segments according to the design. **Figure 41A** shows the scheme and fluorescent microscopy image of the printed samples. The light grey dotted line in the scheme shows the targeted intensity profile.

The fiber was visualized using fluorescence microscopy, where fluorescent particles were utilized to delineate the scattering segments. **Figure 41B** illustrates the fluorescence intensity profile along the printed fiber. The printed scattering segments show the expected length demonstrating a high spatial control in the extrusion printing process. **Figure 41C** presents the quantification of segment lengths from the 10-segment fibers. The lengths of the scattering segments, defined as the FWHM values for each peak, range from 904 .24 µm to 564.59 µm which are relatively close to the target values (1008 µm to 446 µm), while the lengths of the waveguiding segments were systematically ca. 250 µm lower than the target values. Error bars are standard deviation (N = 4). Segments are arbitrarily numbered from the longest scattering segment to the shortest. The waveguiding segments are between the scattering segments, i.e. waveguiding segment 1 is between scattering segments 1 and 2.

The fibers printed with the target design were evaluated to test the tailored side emission profile, and the results were compared to those of a fiber with a continuous scattering segment.

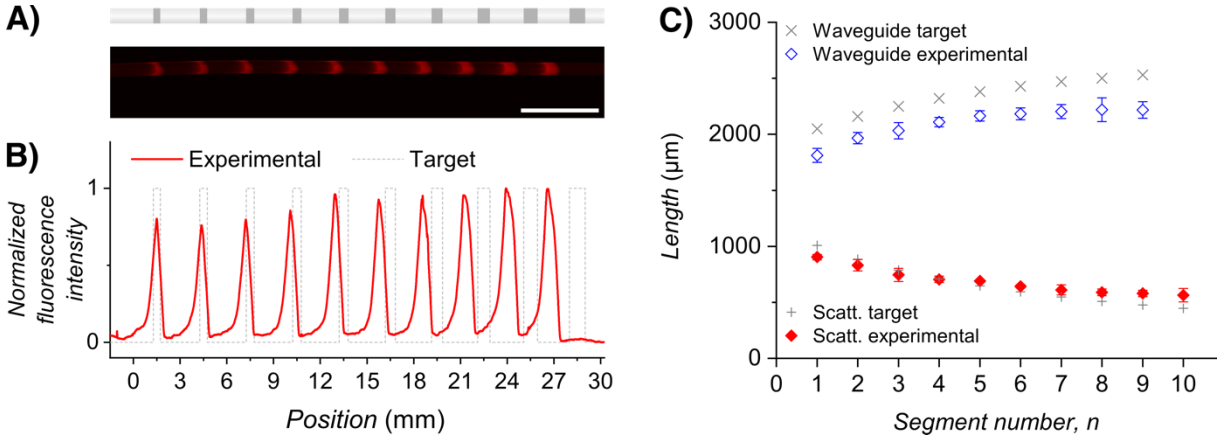

Figure 41. A) Diagram of the targeted segmented fiber showing the length and placement of scattering segments (darker grey) and image of a representative printed fiber. The fiber was imaged by fluorescence microscopy. Fluorescent particles were used to visualize the scattering segments. Scale bar = 5 mm. B) Fluorescence intensity profile of the printed fiber in A). The light grey dotted line shows the targeted intensity profile. C) Quantification of the segment lengths from 10-segment fibers.

Figure 42A shows a schematic diagram and the side emission image from the fiber with 3-cm scattering element. **Figure 42B** presents the normalized side-emission intensity profile of the scattering segment. As previously mentioned, exponential fitting of the side-emission intensity data from the scattering segment yielded an attenuation coefficient of 1.0 ± 0.11 cm^{-1} (optical loss 4.5 ± 0.5 dB cm^{-1} (av. ± s.d.; N = 3)).

Figure 42C shows a schematic of the target fiber containing the ten discrete scattering segments with lengths from 0.45 mm to 1.0 mm and an image of the printed fiber coupled to a 520-nm laser. Outcoupling is observed from each individual scattering segment, and the side-emission intensity profile approaches the theoretical one (**Figure 42D**). The close match demonstrates high spatial control in the printing process. The area of each side emission peak correlates with the total number of photons outcoupled from that scattering segment. These areas are similar for each segment (**Figure 42E**), indicating that each of the ten segments outcoupled approximately the same amount of light as intended in the fiber design. Note that this analysis does not consider light outcoupled from the waveguiding portions of the fiber, as this emission is negligible compared with the side-emitted light from the scattering domains. In conclusion, this result demonstrates the possibility to generate side emitting waveguides with customized size emission profiles by tailoring the length of waveguiding and scattering segments of printed hydrogel fibers using multimaterial extrusion printing technology.

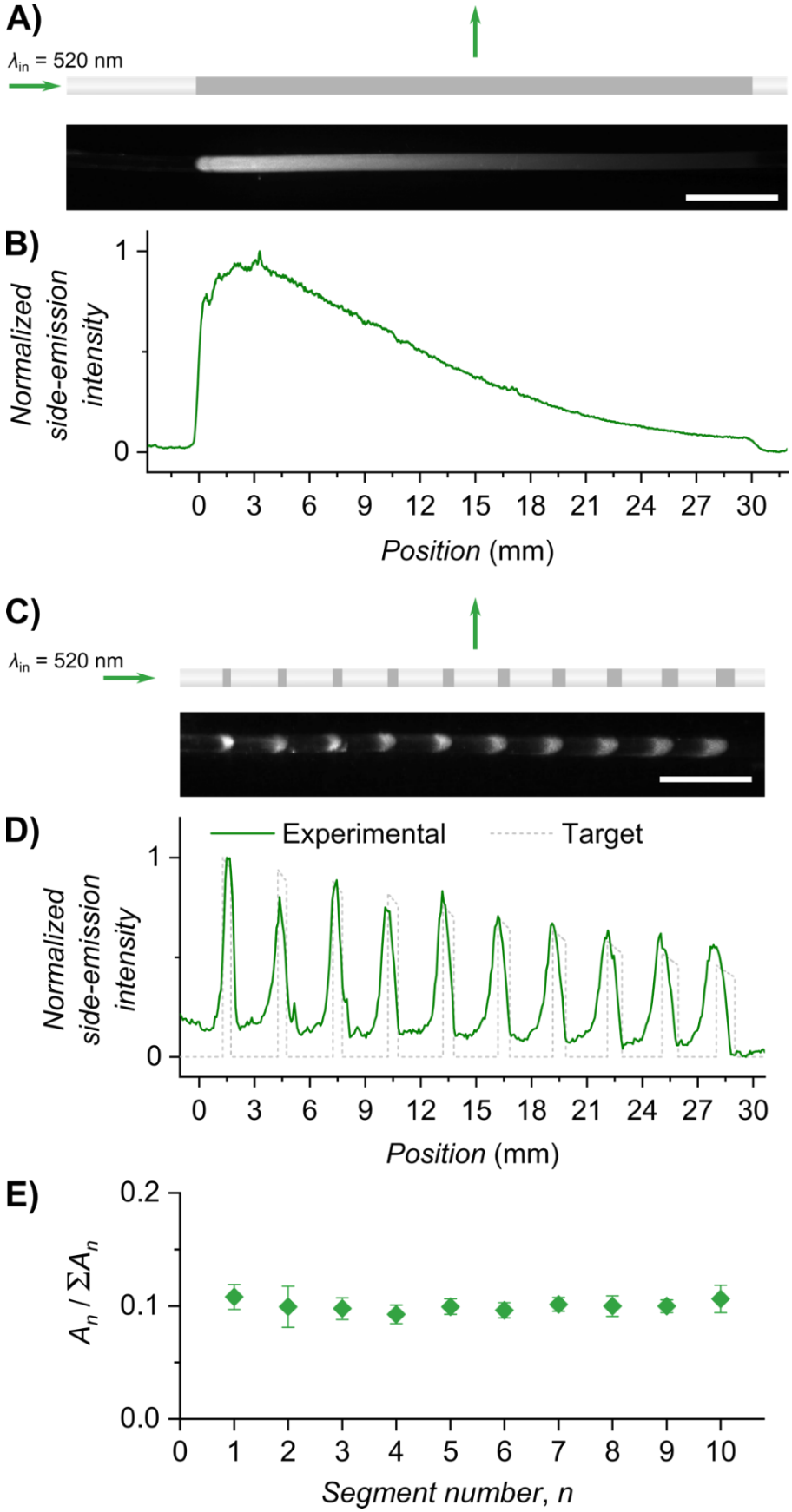

Figure 42. Light emission from side-emitting waveguides in air. **A)** Schematic and representative image of a waveguiding fiber with intercalated 3-cm scattering segment

outcoupling 520-nm light. Scale bar = 5 mm. **B)** Corresponding side-emission intensity profile. **C)** Schematic and representative image of the 10-segment fiber outcoupling 520-nm light, and **D)** its corresponding intensity profile compared with the targeted profile. The maximum of the shortest segment was placed at the position of 1.5 mm, corresponding to the targeted mid-point of that segment in the fiber design. **E)** Area of each segment's side-emission peak (A_n, where n is the segment number) divided by the sum of the areas of all 10 peaks. Error bars are standard deviation from four individual fibers (N = 4). Scale bars = 5 mm. The direction of the incoupled laser light was opposite to (**Figure 42A**) or the same as (**Figure 42C**) the ink flow (printing direction).

3.2.2. Activation of photophysical processes using side-emitting fibers

The ability of the segmented, side-emitting optical fibers to activate photophysical processes was tested by embedding fibers in a gelatin film containing fluorescent nanoparticles that fluoresce when excited with 520-nm light (**Figure 43A)**. To minimize light loss from the waveguiding portions, the fibers were clad with a calcium alginate (Ca-Alg) layer. A top-view image of the fiber-hydrogel construct with in-coupled 520-nm laser light is shown in **Figure 43B**. The ten individual side-emitting segments appear as bright spots within the fiber, indicating that side-emission was taking place. Significant light intensity is also evident in the surrounding hydrogel due to scattering of the outcoupled light by the nanoparticles embedded in the surrounding hydrogel, best observed by obscuring the fiber from the image (**Figure 43C**). Note that this scattering from the surroundings is negligible in air and therefore not visible in **Figure 43C**. The intensity profile of the light in the surrounding hydrogel shows a saw-teeth profile with maxima co-located with the position of the scattering segments of the fiber (**Figure 43D**). A decay in the intensity along the fiber length is observed as expected. Some undesired outcoupling of light also occurs from the waveguiding portion of the fiber prior to the start of the segments, highlighting the sensitivity of the system to defects such as fiber bends or cladding inhomogeneities.

To determine whether the outcoupled light from the fiber could also activate fluorescence of the particles embedded in the surrounding gelatin hydrogel, images were taken with a long-pass filter (> 550 nm) to exclude scattered light (**Figure 43E**). Fluorescence signal was observed in the surrounding hydrogel and also within the fiber since we used PS-NPs scatterers labelled with a fluorescent dye in the scattering ink. By obscuring the fiber from the image (**Figure 43F**), we observe only the fluorescence in the surrounding hydrogel. The corresponding intensity profile (**Figure 43G**) shows a saw-teeth form, similarly to the emitted light profile (**Figure 43D**), with

stronger fluorescence around the scattering domains. The fluorescence intensity decayed along the fiber, though with a less steep profile. The angular dependence of scattering, which is expected to be predominantly in the forward direction based on the size and refractive index of our particles, is evident in both the scattering (**Figure 43B**) and the fluorescence (**Figure 43E**) images. In summary, our experiments confirm that out-coupled photons from the segmented waveguide were able to excite fluorescence in the surrounding gelatin hydrogel. Fluorescence was spatially co-located with the series of scattering segments, i.e. the printed side-emitting waveguides allowed tailored, local excitation of photophysical processes.

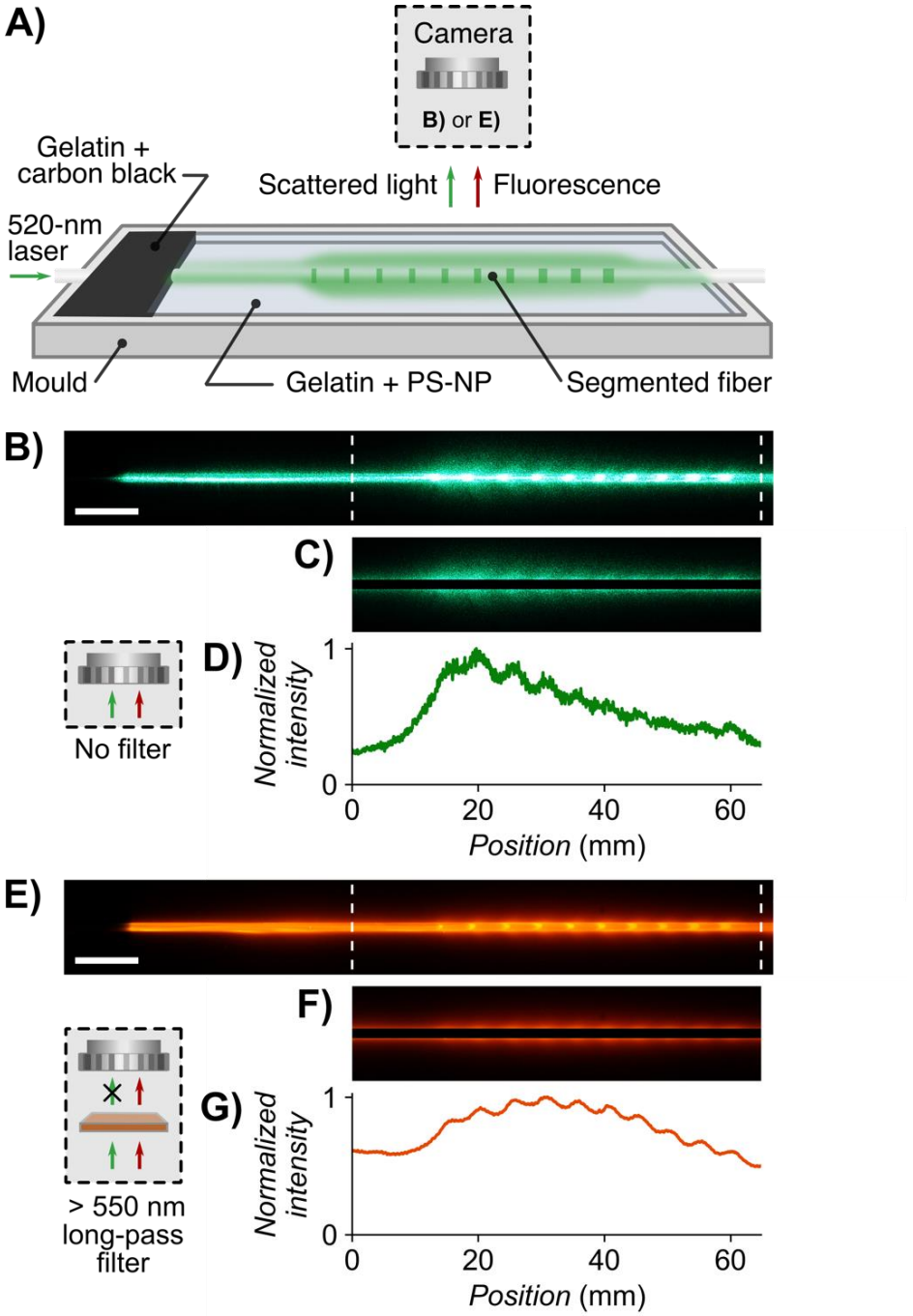

Figure 43. Activation of fluorescence in a hydrogel by an embedded side emitting fiber. The hydrogel contains fluorescent nanoparticles. The PS-NPs in the scattering segments of the fiber are also fluorescent for imaging purposes. **A)** Schematic of the phantom tissue model. The thickness of the gelatin film matched the thickness of the fiber to restrict the fluorescence to the fiber plane and facilitate imaging of the outcoupled light and excited fluorescence. **B)** Top view image of 520-nm light emitted from the fiber into the surrounding gel. **C)** Same image as in B) with the fiber excluded. **D)** Intensity profile of the image in C). **E)** Top view image of the same system using a long-pass filter (> 550 nm) to block incident green photons and observe only the

fluorescence signal which was generated both in the fiber and in the surrounding gel. **F)** Same image as in E) with the fiber excluded to eliminate the fluorescence signal from the PS-NPs inside the scattering segments of the fiber. **G)** Intensity profile of the image in F). All scale bars are 10 mm.

3.2.3. Light-guiding properties of segmented core-cladding fibers

Figure 44 shows macroscopic images of the printed segmented core-cladding waveguide under two different light sources. In **Figure 44A**, the waveguide is illuminated using the torch of an iPhone 13 Pro, demonstrating the distribution and transmission of broadband light through the segments. In **Figure 44B**, a laser emitting at 630-650 nm is coupled into the waveguide, highlighting the focused and wavelength-specific light propagation within the core segments. These images illustrate the waveguide's ability to guide and emit light effectively under varying light sources. **Figure 45** presents fluorescent microscopy images of a printed core-cladding fiber with single (2 mm) and multiple segments, incorporating gold nanorods (AuNRs, 0.07 mg mL^{-1}) and Fluospheres (0.01% w/w). The photothermal properties of the segmented core-cladding fibers are characterized in **Chapter 4.**

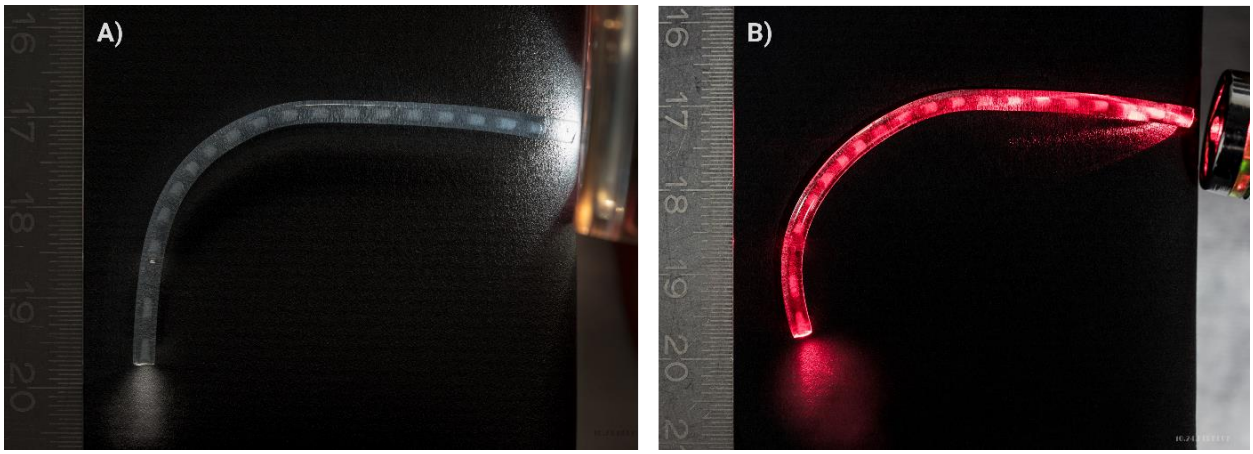

Figure 44. Macroscopic image of printed segmented core-cladding waveguide incoupled with A) Iphone13pro torch, B) Laser 630-650 nm

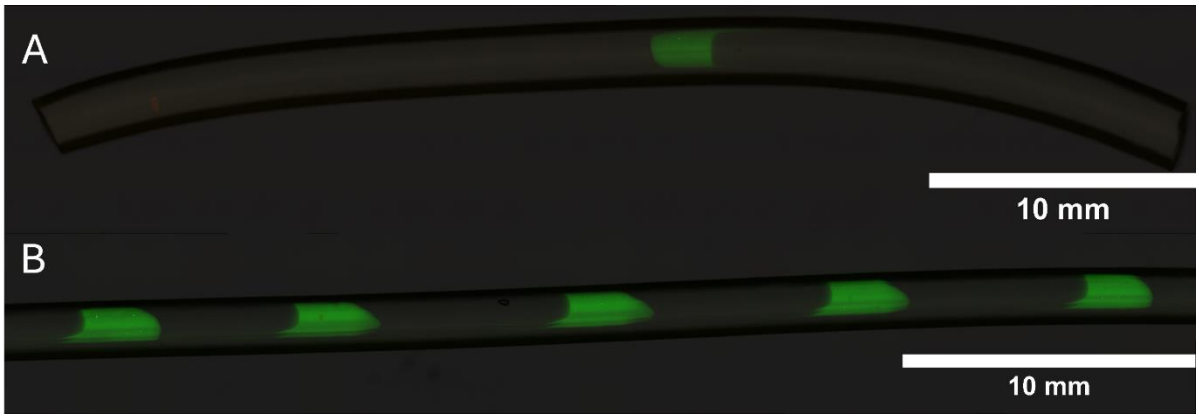

Figure 45. Fluorescent microscopy of the printed core-cladding fiber containing A) single and B) multiple segments of AuNRs (0.07 mg mL^{-1}) + Fluospheres. The images are an overlay of the brightfield image, the green fluorescence (0.01 % w/w Fluosphere) capturing particle fluorescence.

3.3. Conclusive remarks

In this chapter, we tested the side emitting properties of printed hydrogel optical waveguides. Fibers with 30 mm scattering segments showed an optical loss of 4.5 ± 0.5 dB cm^{-1} along the fiber. By distributing scattering elements of increasing length along the fiber length, side-emission could be extended over 30 mm fiber. The resulting side-emission intensity profile closely matched theoretical predictions, demonstrating that individual segments outcouple the expected amount of light. This localized emission makes the developed waveguides interesting for application in photodynamic therapy (PDT).

The functionality of these fibers was further validated by exciting fluorescence within a hydrogel, confirming that out-coupled photons can activate photophysical processes with spatial resolution.

The use of a higher refractive index ink in the core relative to the cladding effectively preserved total internal reflection, enabling segmented core-cladding fibers to demonstrate efficient light-guiding capabilities.

The sensitivity of our fibers to unwanted outcoupling in the waveguiding portions is a limitation that results from their mechanical flexibility and the manual fabrication of fiber cladding and surrounding hydrogel. This can introduce inhomogeneities in the cladding/surrounding hydrogel interfaces and deviations in geometry (e.g. microbends) that can impact light confinement. More

robust light confinement is envisaged by upgrading the fabrication process to print a cladding layer simultaneously with the core.

Our system uses a single channel of scattering ink, which gives a constant concentration of scatterer within scattering segments of variable length. In the future, nozzles with a higher number of inlet channels could be used to accommodate inks with different particle concentrations and generate gradient or other more complex side-emission profiles, or introduce additional segment types or concentric fiber layers.

4. Photothermal properties of plasmonic waveguides

4.1. Introduction

Gold nanorods (AuNRs) show localized surface plasmon resonance (LSPR), high near-infrared (NIR) absorbance, and excellent photothermal efficiency. Recent studies have shown that AuNRs can be incorporated into various hydrogel systems, including alginate, PluDA, PNIPAM, and 4-arm PEG, and provide photothermal properties. To deliver light to the hydrogel, researchers have used focused laser exposure or optical fibers. Additionally, optical fibers have been integrated into plasmonic hydrogel composites containing AuNRs and localized photothermal effects have been demonstrated, allowing for controlled heating and targeted therapeutic delivery.

In this chapter, we investigate the photothermal activity of plasmonic hydrogel waveguides containing segments with AuNR along the fiber length. The waveguides are composed of 30% w/w PluDA in the core and 23.1% w/w PluDA in the cladding. We first assessed the physicochemical properties of the fibers at application-relevant temperatures, followed by photothermal study of various designs using an 808 nm laser incoupling setup. Selim Basaran contributed to the analysis of the IR camera images in this part of the experiments.

4.2. Results and discussions

4.2.1. Photothermal Analysis of Segmented Monofilament Waveguides

To test the photothermal response of the AuNRs embedded in the printed hydrogel fibers, they were illuminated with a 808 nm light source from the top. A laser beam with 10 mm diameter was used for illumination and the evolution of the spatial temperature distribution was recorded using an IR camera. Illumination at 808 nm resulted in an immediate local rise of temperature at and around the plasmonic segments **(Figure 46B-C).** These results confirm that the AuNRs inside the crosslinked PluDA hydrogel maintained plasmonic properties and the printed inks show photothermal properties.

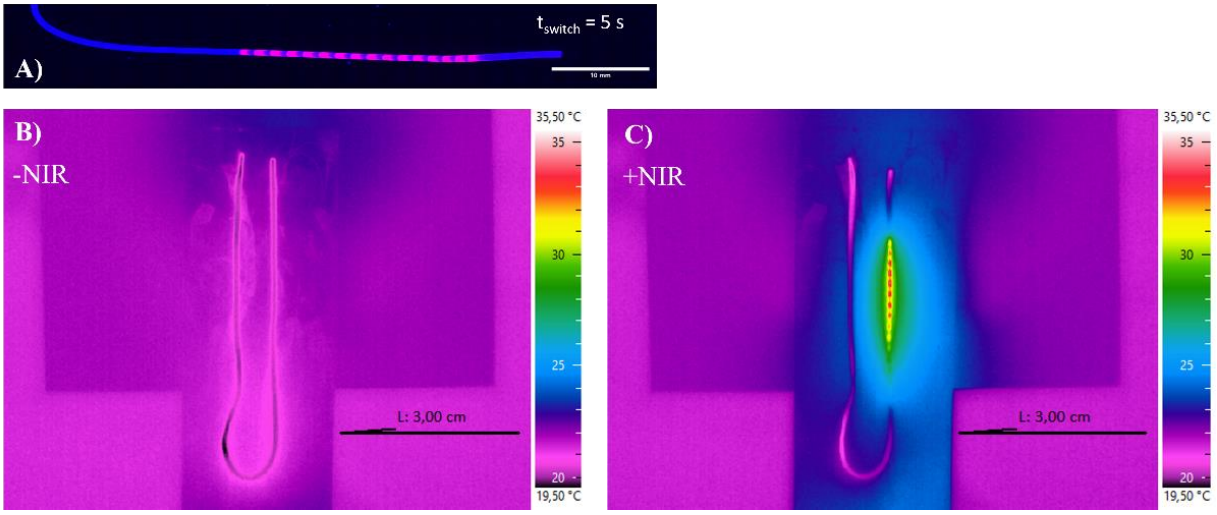

Figure 46 A) Printed fiber containing multiple plasmonic segments with a length of 1 mm. scale bar 10 mm. B) Images of the printed fiber captured with an IR camera. The fiber is placed on a glass slide and images were taken before (B) and during (C) 808 nm irradiation from the top.

To prevent dehydration during illumination and heating, the fibers were placed within a quartz cuvette and submerged in water for the rest of the experiments **(Figure 47A).** In the water bath an increase in the temperature at the plasmonic segment was also observed (**Figure 47B**), from 20 ± 1 °C to 31 ± 1 °C. An elliptic hot spot centered at the plasmonic segment(s) along the fiber

was observed (**Figure 47B, ii&iii**). These results indicate that the plasmonic segments allow local control of the temperature with light.

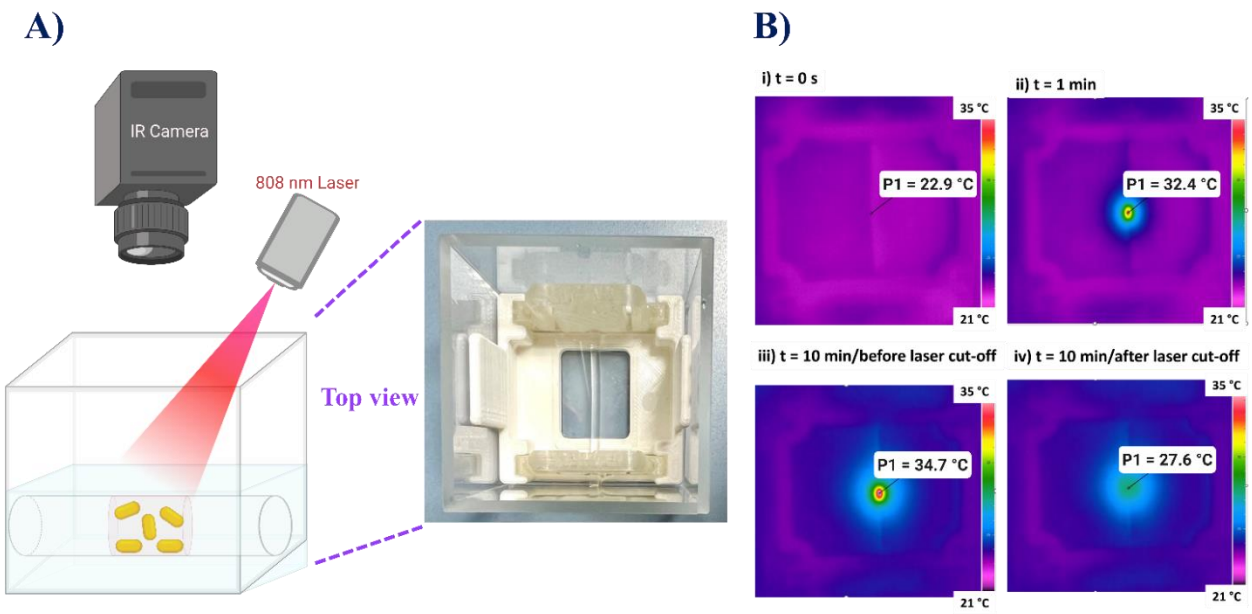

Figure 47 A) Top view image of the holder containing the fiber, highlighted inside the red box. B) Snapshots from the IR camera showing the top view of the cuvette with a 2 mm plasmonic fiber segment illuminated at 808 nm at the following time points: i) t = 0 s, ii) t = 1 min, iii) t = 10 min and iv) 10 min after laser cut-off.

We monitored the temperature changes within the plasmonic segment in cycles of light exposure by quantitative analysis of the IR images at different time points. **Figure 48** represents the average temperature measured within the region where the temperature reaches the highest value during illumination (which coincides with the center of the plasmonic segment) during two cycles of 10 min laser-on followed by 5 min laser-off. Temperature images were recorded each 30 seconds with the IR camera.

Upon illumination, the temperature raised rapidly and reached a constant value around 30°C after 3 to 4 minutes. As the light was switched off, the temperature dropped to almost the initial value within 5 minutes. The second illumination cycle showed a similar profile, indicating that the fiber does not change or is damaged during the heating cycle. The fiber with two plasmonic

segments showed similar temperature profiles for each of the segments, as expected when the fiber is illuminated from the top and both segments receive similar photon densities.

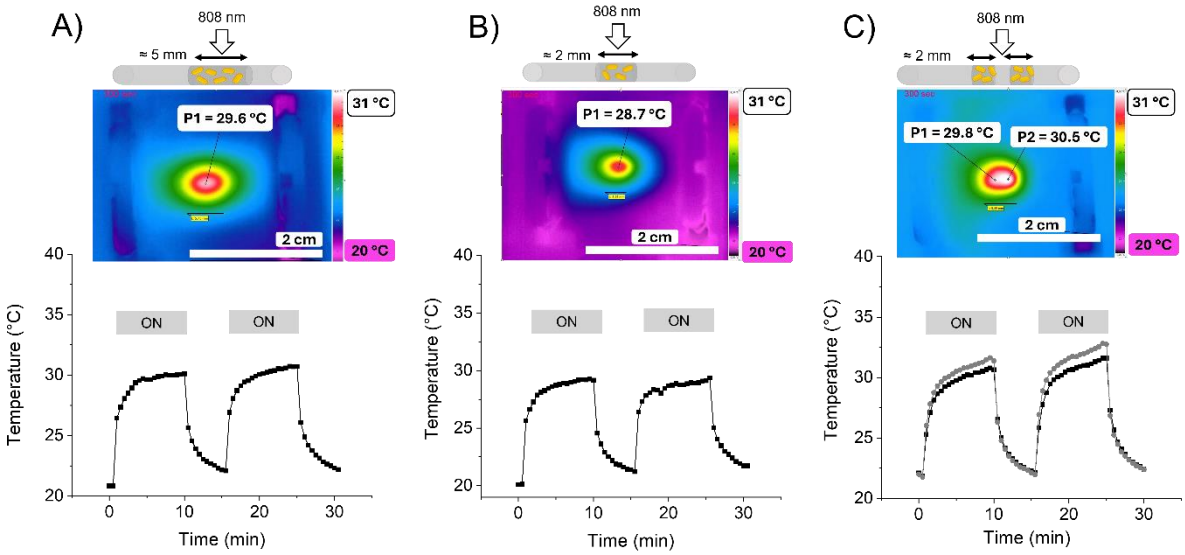

Figure 48 Exemplary IR images and temperature vs. time plots of illuminated fibers with plasmonic segments of A) 5 mm B) 2 mm and C) 2 × 2 mm length. The snapshots correspond to t = 5 minutes

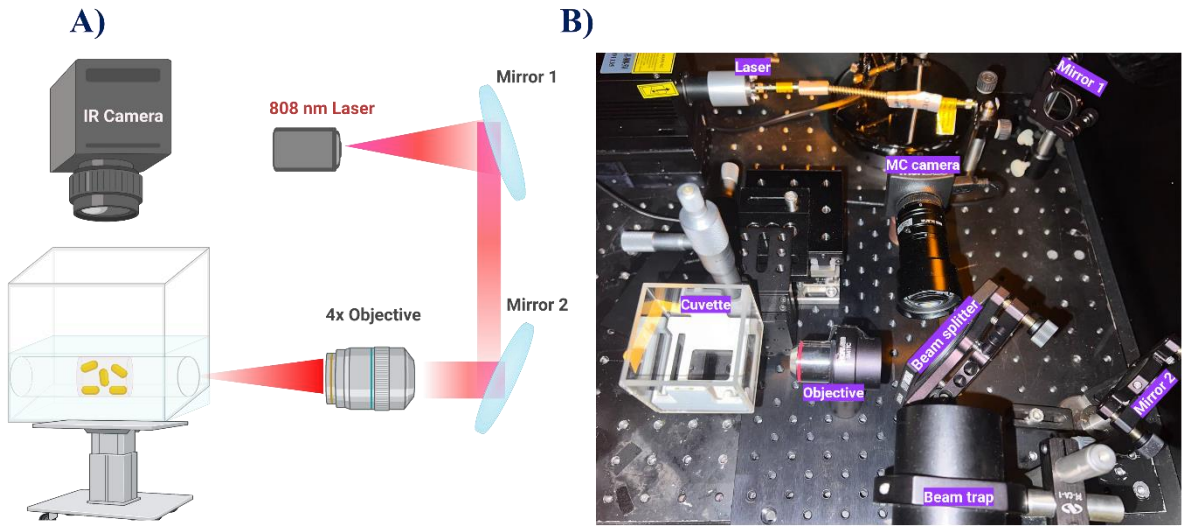

Figure 49 A) Customized setup to incouple light into the plasmonic waveguides. B) Image of the laser focusing setup.

We then tested the combined waveguiding and photothermal functions of the printed plasmonic fibers. **Figure 49A** illustrates the schematic of the setup for light incoupling, where an 808 nm laser beam is directed via two mirrors and a 4× objective lens onto the proximal tip of the fiber. A beam splitter and a camera were used to capture cross-sectional images and monitor the alignment of the beam and the intensity (**Figure 49B**). To check the incoupling of the laser beam to the core of the fiber, the proximal tip of the fiber was imaged before and after laser incoupling. An IR camera was positioned at a 90° angle to the fiber to measure heat development.

Figure 50 shows the photothermal response of plasmonic fiber segments after incoupling light at the proximal tip (808 nm, 164 ±1 mW), evaluated over two repeated laser cycles of 10 min light-on and 5 min light-off. The corresponding temperature-time plot follows the 10 min light on - light off cycles with a heating - cooling response. For the fiber with a single 5 mm plasmonic segment (**Figure 50A**), a hot spot with a maximum temperature of approximately 35.5°C at the place of segment was observed after 5 minutes of illumination. In the fiber with a single 2 mm plasmonic segment (**Figure 50B**), the thermal response reaches a peak temperature of 36.5°C. For the fiber with two 2 mm plasmonic segments separated by a 2 mm gap (**Figure 50C**), thermal imaging reveals two distinct hotspots corresponding to the individual plasmonic segments. **Figure 51** presents a magnified view of the focused light distribution alongside the corresponding fluorescence microscopy image of the sample. The total length of the heated region is approximately 6 mm. The heating in the first segment is more pronounced, while the second segment exhibits an elongated, oval-shaped distribution, indicative of light diffusion into

the second segment. However, the heating effect in the second segment is less intense than in the first, likely due to optical and thermal losses during propagation.

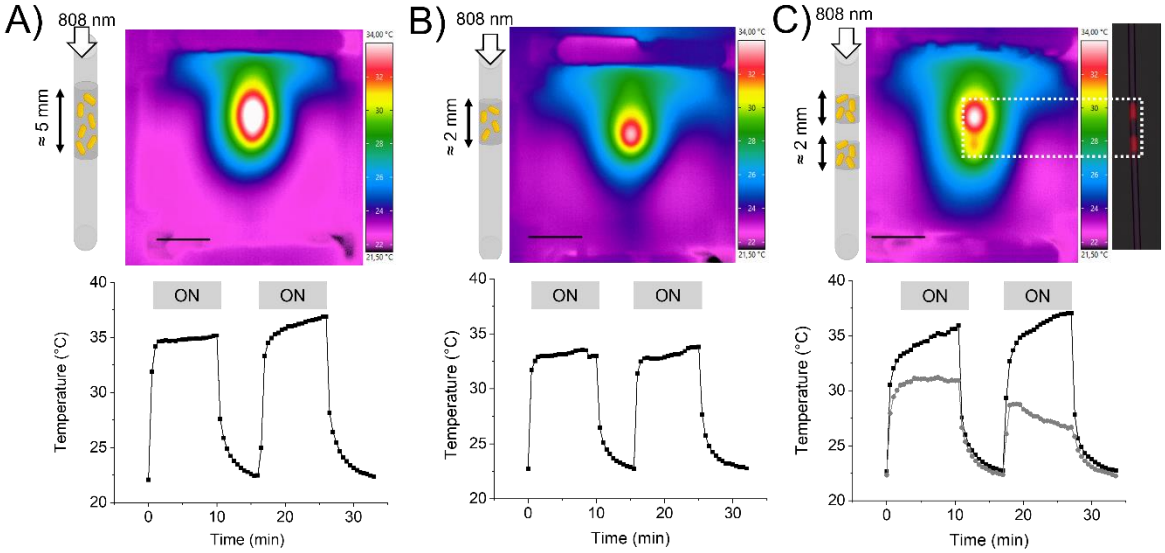

Figure 50 Temperature over time plots for incoupling setup for samples with A) 5 mm, B) 2 mm, and C) 2 × 2 mm Plasmonic segments with corresponding IR snapshots at t = 5 minutes. The grey line corresponds to the temperature in the second segment. The analysis of the IR camera images in this experiment was done by Selim Basaran.

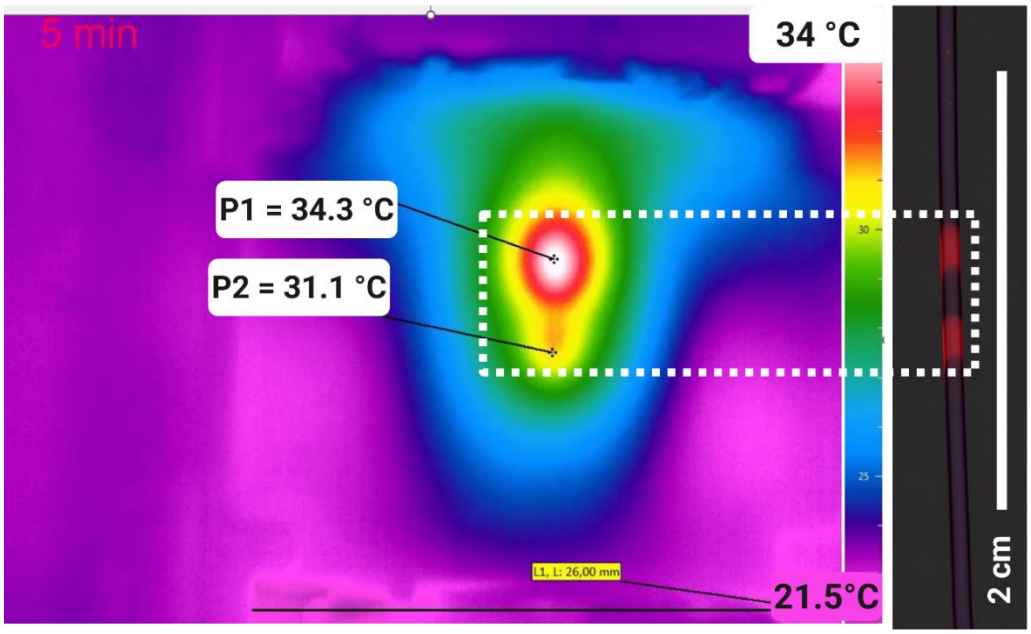

Figure 51. Comparison of the locations of observed heated spots with the fluorescence microscopy images of the corresponding sample. Scale bar 2 cm applies to both images.

Figure 52 illustrates the lateral heat distribution profiles along the plasmonic segment with 5 mm and 2 mm lengths. For the 5 mm segment, a peak temperature of approximately 36.5°C and

a gradual decline in temperature to 32 °C at 5 mm from the hot spot was observed. The attenuation coefficient of 0.46 mm^{-1} measured for the 5 mm sample with an absorbance of 2 (section 2.2.7) implies that 90% of the incident light is absorbed within the first 5 mm. This significant absorption of light results in energy being converted into heat, leading to a temperature increase.

The 2 mm segment exhibits a more localized heat profile, with a maximum temperature of around 34°C and a steep drop in temperature within 2 mm.

The broader lateral temperature distribution observed for the 5 mm segment compared to the 2 mm segment can be attributed to both optical and thermal effects. First, the exponential decay of light along the fiber due to intrinsic absorption and scattering plays a role in determining segment, light diffusion over a longer plasmonic region allows more energy to be absorbed and converted into heat, resulting in a broader lateral heat distribution. Conversely, in the 2 mm segment, the shorter interaction length confines the light absorption and photothermal conversion to a smaller region, leading to a more localized temperature profile. Since the incoupling of light was performed separately for each experiment, and the number of incoupled photons was not

identical, the absolute temperature values from 2 mm and 5 mm segmented fibers are not directly comparable.

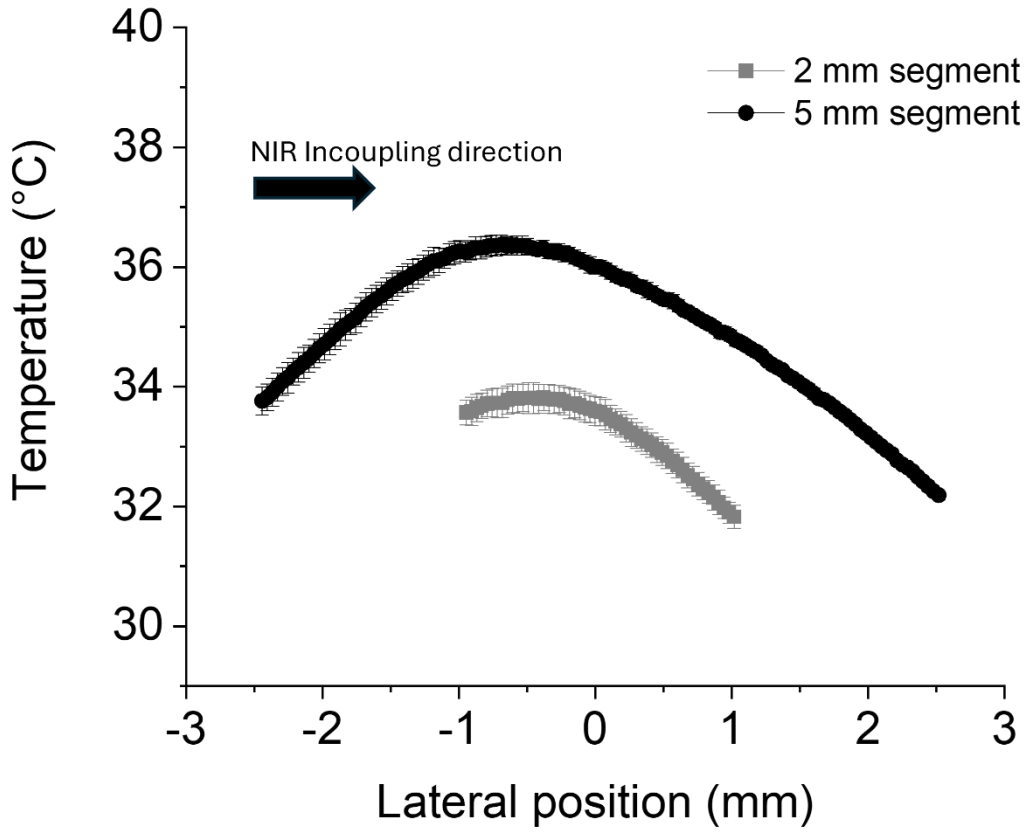

Figure 52 Lateral temperature distribution across the plasmonic segment for the waveguide containing 2 mm and 5 mm plasmonic segments.

4.2.2. Photothermal tunability and stability of the core-cladding waveguides

The temperature response of core-cladding fibers with varying laser intensities and illumination cycles was studied. Prior to the experiment, the printed fiber was immersed in Milli-Q water for 2 hours, placed in a customized holder for the measurements, and kept in Milli-Q water during the experiment to prevent dehydration. The diameter of the core-cladding fiber was 2.5 mm (pre-swollen state) and 3.5 mm (fully swollen state). The fibers were positioned in the previously described laser coupling setup, and the heating process was monitored using the IR camera.

The temperature response of a core-cladding fiber with a single 2 mm plasmonic segment under varying incoupled laser intensities ranging from 20 ±1 to 683 ± 1 mW is shown in **Figure 53**.

The temperature at the plasmonic segment increased as the laser intensity increased and stabilized between 23°C and 36°C for laser powers between 20 ±1 to 683±1 mW. These results demonstrate the possibility to tune the heating temperature at the plasmonic fiber by controlling the input laser power.

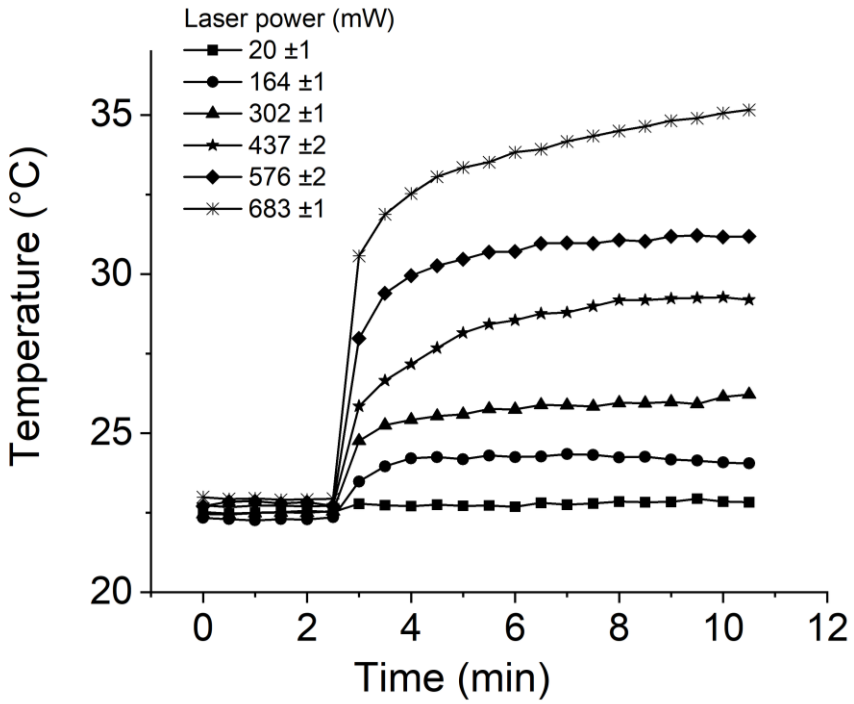

Figure 53. Temperature measured in the middle of a 2 mm plasmonic segment in a core-cladding fiber after incoupling NIR light at increasing laser power.

Figure 54A shows the temperature profile of a different core-cladding fiber at 576±2 mW power intensity obtained from IR camera images. A stable temperature of 32°C could be maintained during one hour, demonstrating the stability of the photothermal response of the PluDA plasmonic fibers under prolonged laser exposure. Parallel temperature measurements with a thermocouple placed inside the fiber (separate sample) near the plasmonic segment (≈ 1 mm space) revealed temperatures approximately 10° C higher than the temperature sensed by the IR camera (**Figure 55A,B**). The thermocouple was inserted into the fiber without any mechanical support or holder. As a result, the small fluctuations observed during the measurements can be attributed to the free movement of the thermocouple tip during the experiment.

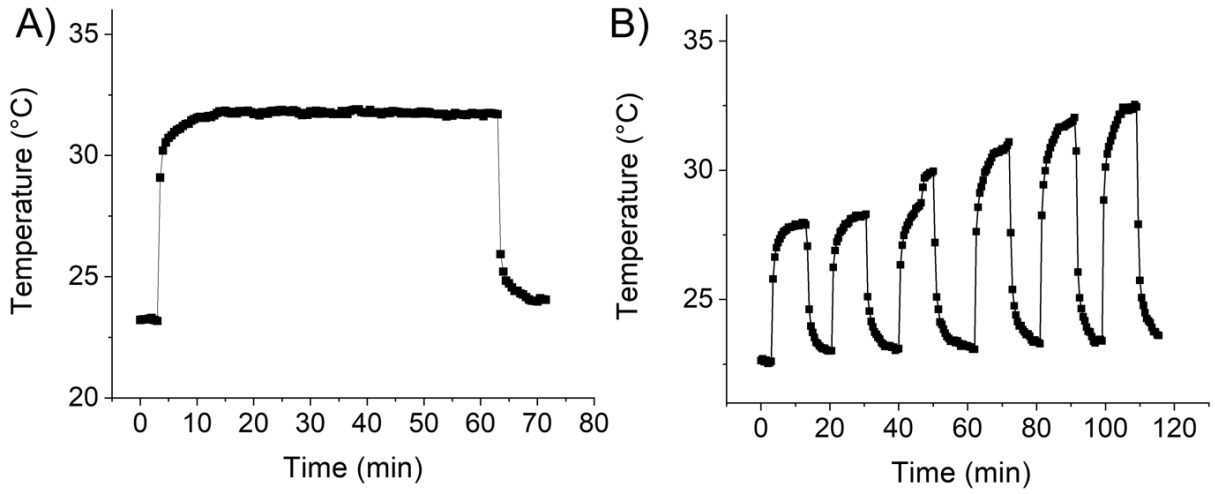

Figure 54. The temperature profile of a core-cladding fiber with a 2 mm plasmonic segment illuminated by an 808 nm laser at 576 ± 2 mW over one hour. B) Repetitive cycle of NIR irradiation in six cycles of ten minutes.

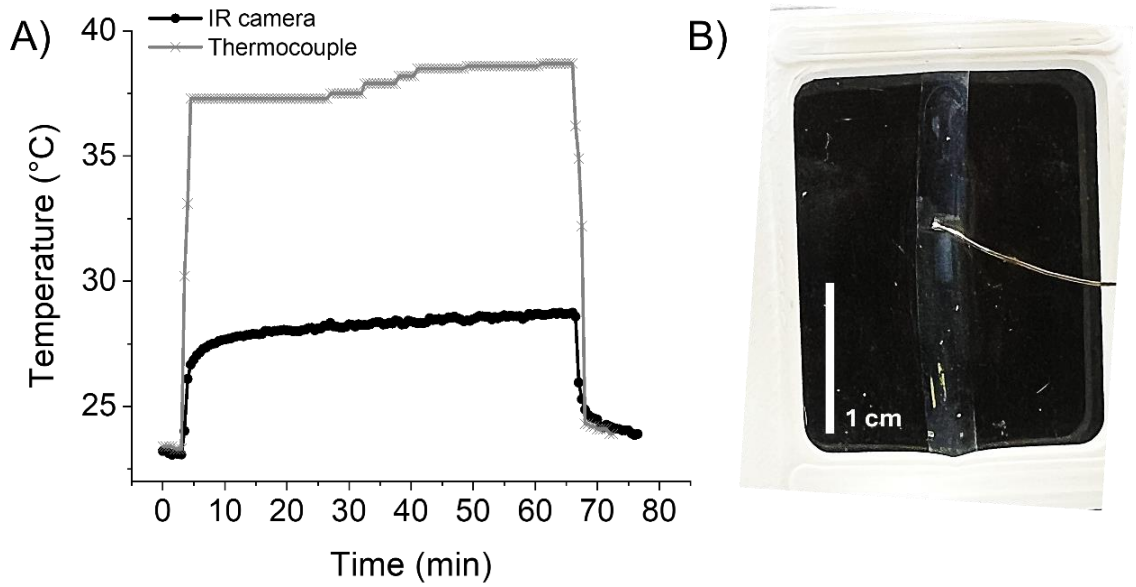

Figure 55. Temperature profile of a core-cladding fiber with a 2 mm plasmonic segment illuminated by an 808 nm laser at 576 ± 2 mW over one hour. B) Sample with inserted thermocouple within the fiber.

Figure 54B depicts the cyclic temperature response of a core-cladding fiber with a 2 mm plasmonic segment during 6 illumination cycles by an 808 nm laser at 576 ± 2 mW over a period of 120 minutes. Rapid heating and partial stabilization of temperature during the one phase, and rapid cooling when the light is switched off was observed. With each successive cycle, a gradual

increase in the peak temperature is observed due to the overall warming of the surrounding aqueous medium in the experimental chamber as the experiment progresses, and water eventually evaporates. The consistent photothermal response across multiple cycles demonstrates the robustness of the fiber and its ability to sustain repeated cycles of operation without significant degradation or loss in performance.

4.3. Conclusive remarks

In this study, we characterized the photothermal properties of multimaterial waveguides incorporating plasmonic gold nanorod (AuNR) segments. Building upon prior work in hydrogel-based optical fibers with controlled side emission[148], we replaced scattering elements with plasmonic AuNRs to enhance the functionality of the fibers for photothermal applications. The use of AuNRs in hydrogels has been previously explored for applications such as engineered living materials activation[112], drug delivery[109], and tumour therapies.[115] External NIR illumination of hydrogels containing AuNRs has been shown to generate significant localized heat, with temperature increases up to 77 °C.[115] A key limitation in existing approaches for plasmonic hydrogel photothermal applications is the reliance on external NIR light sources, which suffer from limited photon penetration in tissue. This inefficiency reduces the therapeutic potential for in vivo applications, particularly in deep tissue environments.

Optical fibers for direct light delivery to plasmonic hydrogels have been explored in the literature. Lacroce et al. employed silica-based optical fibers inserted into hydrogels containing AuNRs. This approach achieved localized temperature increases of up to 16.9 °C under NIR light irradiation.[113] However, silica fibers exhibit poor biocompatibility due to their rigidity[13b], which creates mechanical mismatches with soft biological tissues, limiting their utility in vivo.

Liu et al.[114] developed optical fibers using polydimethylsiloxane (PDMS) embedded with gold nanoparticles and coated with a polyacrylamide hydrogel. These soft fibers demonstrated significant heating capabilities, achieving nearly 50 °C temperature increases under 520 nm laser illumination. Despite their improved biocompatibility, the heating effect was confined to the fiber tip, resulting in poor spatial distribution of heat along the fiber's length and limiting their effectiveness for uniform activation of plasmonic hydrogels at targeted places.

The fibers in this Thesis integrate AuNR segments directly within the core . This method allows precise spatial control of the plasmonic segments and enhances light delivery to the target. By using core-cladding designs, we achieved stable optical fibers capable of sustaining their structure in aqueous media at room and 40 °C. Under NIR laser illumination, the waveguiding part can deliver light within the core to the AuNR-containing segments and generate localized

heating with temperature increases up to 40 °C at a concentration of 0.07 mg mL^{-1}, opening new avenues for controlled light delivery and thermal actuation The heat generated in these segments has the potential to trigger thermo-responsive systems, such as bacteria encapsulated in the hydrogel cladding, for controlled drug delivery within the body.

The use of multimaterial printing allows precise localization of the AuNR segments, enabling targeted heating and reducing off-target effects. Second, the core-cladding structure enhances light confinement as well as the bacterial confinement. Finally, the ability to integrate thermo-responsive systems within the cladding layer adds a new dimension of functionality, making these fibers suitable for sustainable, on-demand drug delivery platforms.

Future work will focus on localized activation of engineered living materials exploring the integration of alternative plasmonic nanoparticles with tailored optical properties that could further enhance the thermal response.

5. Conclusion and outlook

This thesis presents the design and a fabrication approach to hydrogel-based optical waveguides with tunable side emission and integrated thermal activation functionalities. To integrate these different functionalities in a single device, multimaterial extrusion printing was employed. Pluronic diacrylate (PluDA) solutions was selected as inks. A mixture of PluDA and polystyrene beads was used as the scattering ink to obtain side-emitting fibers. A mixture of PluDA and AuNRs for plasmonic ink and core-cladding designs were used in thermoresponsive fibers. The following conclusions are taken from the work performed:

1. Pluronic hydrogels are interesting materials for printing multimaterial hydrogel fibers with tunable and localized optical properties at sub-millimeter spatial resolution. Pluronic F-127, forms physically crosslinked micellar hydrogels within specific concentration and temperature ranges, exhibiting a lower critical solution temperature (LCST) near room temperature at concentrations above 15% w/w, allowing for temperature-controlled extrusion processing. At 17% w/w and 35 °C, Pluronic gels display a yield stress of 155 Pa, fulfilling the necessary criteria for extrusion-based multimaterial printing due to their viscoelastic and shear-thinning properties. The chemical modification of Pluronic F-127 with acrylate groups to form PluDA does not significantly alter its rheological behavior, while enabling post-processing stabilization through radical or photopolymerization crosslinking. PluDA hydrogels prepared at 23.1% w/w exhibit a refractive index (RI) of 1.366, increasing to 1.38 at 33% w/w (at 547 nm). This RI value exceeds the RI of biological tissues like skin (1.32) and falls within the intermediate hydrogel RI range (1.33–1.37), making PluDA a suitable waveguiding material. Additionally, its tunable RI allows for the selection of lower RI cladding materials for total internal reflection and efficient waveguiding performance. These properties make PluDA promising for flexible optical waveguides

2. Inks with increasing Pluronic concentrations from 23% to 33% w/w show a higher critical yield stress (from 0.62 kPa to 2.02 kPa), and require higher extrusion pressures (ranging from 700 mbar to 3000 mbar) and higher static pressure to prevent backflow during switching. In this work, successful switching was achieved using Pluronic at 23.1% and 30% w/w, enabling low transition lengths and the fabrication of sub-millimeter segments. This resolution is comparable to multimaterial extrusion printing of silicone,

demonstrating the feasibility of controlled switching in hydrogel-based multimaterial systems. The versatility of PluDA as a shear-thinning material not only supports the fabrication of hydrogel fibers but also offers the potential to create three-dimensional structures by programming the motion of the printhead. The use of multimaterial extrusion printing further enables the fabrication of complex fiber geometries and functional heterogeneities without the need for post-processing or additional stabilization steps

3. Introducing UV crosslinking into multimaterial extrusion printing enables the fabrication of chemically crosslinked and mechanically stable hydrogel-based optical fibers. The UV illumination intensity influences both the degree of crosslinking and the system's flow rate, impacting the overall printing process. The UV exposure intensity and the flow rate need to be adjusted to obtain crosslinked fibers while preserving the desired optical and mechanical characteristics. The printed fibers exhibit stability in an aqueous medium for over 24 hours at room temperature, 37°C, and 40°C, demonstrating their structural integrity under physiologically relevant conditions.
4. This work demonstrates that the combination of PluDA as a base ink, particle scatterers, and multimaterial extrusion printing enables the fabrication of waveguides with controlled light outcoupling along a defined fiber length. By precisely tuning segment lengths and spacing, the fabrication process allows for customized side-emission profiles, deviating from the typical exponential decay of light intensity observed in side-emitting fibers with a single emitting segment. The incorporation of alternative nanoparticles or functional fillers could expand the fibers' applicability. For instance, using particles with tunable absorption properties would enable multi-wavelength control, which is relevant for photonic therapies requiring distinct light-activation thresholds. PluDA's rheological properties allow a scalable printing process integrating scattering functionalities directly into the fibers, holding potential for applications where precise light delivery is critical, such as PDT. This capability reduces unnecessary light exposure to surrounding healthy tissues, thereby increasing treatment specificity and minimizing collateral damage.
5. Localized heating can be achieved by introducing AuNRs in segmented plasmonic hydrogel optical fibers with photothermal properties. The temperature elevation is dependent on the AuNrs concentration and laser power. In our case the printed fibers successfully guided 808 nm light to the plasmonic segments, demonstrating effective waveguiding functionality. Localized heating was observed, with temperature increases reaching up to 40 °C at nanorod concentrations as low as 0.07 mg mL^{-1}. This is within

the range of reported works from other authors, with examples ranging examples ranging from 0.001 up to 0.175 $mgmL^{-1}$ and achieving ΔT up to 30 °C. This thermal range within the physiological temperatures is relevant for potential applications in temperature-regulated drug release platforms. The ability to simultaneously deliver light and heat within a single fiber provides an integrated mechanism for spatially resolved therapeutic interventions.

The fabrication strategy described here—relying on continuous extrusion, in situ curing, and the incorporation of dynamic functional components—represents a step toward realizing adaptable, multifunctional optical fibers.

Moreover, the compositions used in this work are also applied in the field of living therapeutics. By expanding the cladding layers of the fibers to integrate thermo-responsive bacteria, the sie-emitting waveguides of this work can become interesting as implantable therapeutic devices, offering localized and controlled therapeutic action.

Another area of potential exploration is the extension of these fibers into soft robotics. Their ability to combine localized light delivery, thermal actuation, and responsiveness to external stimuli provides an opportunity for developing systems capable of sensing and interacting with their environment. For example, programmable hydrogel fibers could be embedded into robotic grippers or actuators, allowing for dynamic shape changes or drug release in response to specific environmental triggers.

6. Materials and methods

Formulation of Pluronic F-127 inks

Pluronic F-127 solutions were prepared by dissolving Pluronic F-127 (1.5 g, Sigma-Aldrich) in MilliQ water (5 mL) by overnight vortexing inside a 4 °C fridge. Homogeneous solutions with 23.1 % w/w polymer content were obtained and kept cold until used.

Colored Pluronic F-127 solutions were prepared similarly by adding pararosaniline (0.06 % w/w) or carbon black (0.5 % w/w) to the mixture prior to dissolution.

For the fluorescent scattering ink, carboxylate-modified polystyrene-based microspheres (Crimson FluoSpheres F8806, 200 nm diameter, fluorescent dye excitation and emission 625/645 nm respectively, Thermo Fisher Scientific) were incorporated at 0.01 % w/w by adding 25 µL of commercial FluoSphere stock dispersion (2 % w/w) to the Pluronic solution.

For the non-fluorescent scattering ink, carboxylate-modified polystyrene-based microspheres (CML Latex Beads, 200 nm diameter, Thermo Fisher Scientific GmbH) were incorporated at 0.01 % w/w by adding 12.5 µL of commercial PS stock dispersion (4 % w/w) to the Pluronic solution.

Formulation of photocrosslinkable PluDA inks

PluDA with a degree of acrylate functionality of 70 % was prepared as previously described.[23] A stock solution of photoinitiator was prepared by dissolving Irgacure 2959 (5 mg) in MilliQ water (1 mL) with sonication for 45 min. For the waveguiding ink, PluDA (1.5 g) was dissolved in a mixture of MilliQ water (3 mL) and photoinitiator stock solution (2 mL) to give 23.1 % w/w PluDA and 0.2 % w/w Irgacure 2959. Dissolution was performed overnight at 4 °C as described for Pluronic F-127. For the fluorescent scattering ink, the same FluoSpheres as described above were incorporated at 0.01 % w/w by adding 25 µL of commercial FluoSphere stock dispersion (2 % w/w) to the PluDA prior to dissolution. For the non-fluorescent scattering ink, the same PS particles as described above were incorporated at 0.01 % w/w by adding 12.5 µL of commercial PS stock dispersion (4 % w/w) to the PluDA prior to dissolution. For higher concentrations, PluDA (1720.4 mg) was dissolved in a mixture of Milli-Q water (2.4 mL) and photoinitiator stock solution (1.6 mL) to achieve a final concentration of 30% w/w PluDA and 0.2% w/w Irgacure 2959. The 33% w/w PluDA ink was prepared similarly by dissolving PluDA (2000 mg)

in Milli-Q water (2.4 mL) with photoinitiator stock solution (1.6 mL). Dissolution of these inks was performed following the same procedure as for Pluronic F-127.

For the plasmonic PluDA ink, CTAB-modified AuNRs were purchased from NANOPARTZ (length: 41 nm, diameter: 10 nm) . After sonicating the stock solution for 10 minutes, 6 mL of AuNRs were centrifuged at 12,800 RPM for 8 minutes, the supernatant (5720 µL) was removed and the 280 uL AuNRs were resuspended in the PluDA solution to a concentration of OD 2 by adding to 30% w/w PluDA solution containing 860.2 mg PluDA, Milli-Q water (920 µL) with photoinitiator stock solution (800 uL). The solution was vortexed for 30 seconds prior to inserting in to the cartridges.To facilitate imaging of the plasmonic segment, green FluoSpheres (F8810, Thermo Fisher Scientific; excitation and emission wavelengths: 580 and 605 nm, respectively) at 0.01% w/w concentration were incorporated into the PluDA solution. This was achieved by adding 25 µL of commercial FluoSphere stock dispersion (2% w/w) to the solution. The FluoSphere stock solution was sonicated for 10 minutes before incorporation.

Viscosity measurement by rheology

Viscosity measurements were performed using a controlled stress rheometer (HR-3, TA Instruments) equipped with a cone-plate geometry with 40 mm diameter and a cone angle of 1°. 300 µL of ink at 4 °C were pipetted into the cone-plate gap. The temperature was set at 25 °C, and shear sweeps were conducted over the shear rate range of 0.01 s^{-1} to 100 s^{-1}.

For strain sweep measurements, samples were prepared by pipetting 35 µL of freshly prepared PluDA solution onto the rheometer plate, allowing the gel to form between the plates (12 mm diameter, 300 µm gap). Strain sweeps were performed over a range of 0.001% to 1000% at a frequency of 1 Hz. In the resulting strain amplitude sweep curves, a line was fitted to the linear (plateau) region and the non-linear (drop-off) region. The intersection of these lines was determined as the critical strain value (γy).[123a]

UV spectroscopy characterization of the inks

Pluronic F-127 solutions (23.1 w/w %) supplemented with 0.01 % w/w PS particles or FluoSpheres were filled into a quartz cuvette with 10 mm path length and allowed to warm to room temperature. The absorbance was measured on a Varian UV/Vis Spectrometer 4000 over the wavelength range of 200 – 800 nm. Non-scattering ink was measured similarly. A solution of PluDA (30% w/w) or PluDA containing 0.07 mg mL^{-1} AuNRs was loaded into a quartz cuvette with a 10 mm path length and allowed to equilibrate to room temperature (5

minutes). Absorbance measurements were performed using a Agilent UV-Vis-NIR Spectrophotometer, covering the wavelength range of 200 to 1200 nm.

Nozzle fabrication

The design of the Y-shaped nozzle for monofilament fibers was uptaken from reported work.[148] The Y-shaped nozzle for printing core-cladding fibers was designed using AutoCAD software. The nozzle featured 500 µm diameter inlets for both the core and cladding materials, positioned at a 60° angle. The monofilament nozzle had an outlet diameter of 1000 µm, while the core-cladding nozzle had an outlet diameter of 1000 µm for the core and 500 µm for the cladding, resulting in a total inner outlet diameter of 2.5 mm. The nozzle was 3D printed using an ASIGA SLA printer with Optiprint Splint 385 resin. The printing process was conducted with a layer thickness of 50 µm and an exposure time of 0.5 seconds per layer.

Extrusion printing of Pluronic F-127 inks

Pluronic F-127 inks at ≈ 0°C containing pararosaniline and carbon black were poured into two capped 10 mL syringes (product number 502783, VIEWEG). The syringe pistons were fitted to the syringe barrels, and each syringe was sonicated in an inverted position on ice for 1 h to remove bubbles. Backflow control valves (BCV) with Luer-Lock (Fresenius BCV, C2 Medical) were then fitted to the syringe tips, and the syringes were attached to the two inlets of the Y-shaped nozzle with its outlet facing upwards. The pistons were pushed manually to fill the inlets and outlet without bubble generation. In this inverted position, the setup was left for 1 h at room temperature for the inks to achieve room termperature and form physical gels. The nozzle was then clamped in the holder of a 3D-Bioscaffolder extrusion printer (GESIM). Barrel adapters from a pneumatic pressure controller (OB1 MK4, Elveflow) were fitted to the syringes, and the controller was programmed to alternate between 0 mbar and 750 mbar in each channel with switching times of 5 s, 2 s, 1 s, and 0.5 s. A video of the extruded ink was captured and representative frames for switching times of 5, 2, 1 and 0.5 s . The controller was set to a flow pressure, P_{flow} range of 0-750 mbar for 23.1 % w/w, 1000–2000 mbar for the 30% w/w ink and 2000–3000 mbar for the 33% w/w ink. Static pressure, P_{static}, was varied from 500 to 1000 mbar for the 30% w/w ink and between 1500 and 2500 mbar for the 33% w/w ink. Switching times, t_{switch}, of 30, 15, 10, 5 and 1 s were used for the 30% w/w ink and t_{switch} of 30 and 15 s for the 33% w/w ink. Videos and images of the extruded ink were captured using an iPhone 13 Pro.

For core-cladding extrusion, 30% w/w Pluronic F-127 ink containing pararosaniline and carbon black were used as core inks and 23.1% w/w Pluronic F-127 was used as cladding ink. Extruded ink images and videos were captured using an iPhone 13 Pro.

Setup for photocrosslinking PluDA fibers

Cold waveguiding and scattering PluDA inks were loaded into the printing setup as described above. A transparent silicone tube (inner diameter = 1.02 mm, length = 4.5 cm) was attached to the nozzle outlet. The tube was placed vertically inside a customized holder in which the UV lamp (Omnicure S1500, 320-500 nm output, Excelitas Canada Inc.) was fitted perpendicular to the silicone tube. The light power was measured at the position of the silicone tube using a power meter (FieldMaster, Coherent Corp.).

Determination of curing and extrusion printing parameters

The required irradiance to generate stable fibers (23.1 % w/w) was assessed using a P_{static} = 1200 mbar and a P_{flow} = 1700 mbar. UV lamp powers from 5 % (97 mW cm^{-2}) to 30 % (147 mW cm^{-2}) were tested. The extrusion rate was quantified by cutting and weighing fiber segments produced in intervals of 2.5 min (during the first 10 min) or 5 min (during the remaining time) throughout the 80 min fabrication time. The obtained segment lengths were quantified using a light power of 10 %, P_{static} = 1200 mbar, and varying switching times (15, 10, 7.5, 5, 2.5, 1 s) and flow pressures (1600 mbar, 1700 mbar, 1800 mbar). Extrusion printing was performed for 10 min to allow the flowrate to stabilize, and then fibers with at least 20 alternating segments were produced. Fibers were collected on a glass slide moved by hand as the extrusion proceeded and stored in sealed petri dishes containing a wet tissue to prevent drying before imaging. The same procedure was repeated for 30 % w/w. The required printing pressures and irradiance to print crosslinked fibers were assessed first. P_{flow} ranges between 2000 to 2500 mbar and UV lamp powers between 1 to 10 % (78 - 115 mW cm^{-2}) were tested. Handeable fibers were obtained at P_{flow}=2300 mbar and lamp power 4 and 5%, and at P_{flow}=2500 mbar using lamp power of 7 and 8%. The printing rate was quantified by cutting and weighing fiber segments printed in intervals of 2.5 min (during the first 10 min) or 5 min (during the remaining print time) throughout a 80 min printing time. Segmented fibers were printed at light power of 7 %, P_{flow} = 2500 mbar, t_{swicth}=15 s and P_{static} 1500, 1700, 2000, 2100, 2200 and 2400 mbar. For this purpose, filaments were printed during 10 min to allow the flowrate to stabilize, and fibers with at least

20 alternating segments were printed. Fibers were collected on a glass slide manually moved and stored in sealed petri dishes containing a wet tissue to prevent drying before imaging.

Quantification of segment lengths

Fibers were imaged on a BZ-X800 fluorescence microscope (Keyence, Osaka, Japan) using a Plan-Apochromat 4X/ 0.2 NA objective (Keyence, BZ-PA04). The filter DAPI (BZ-X Filter OP-87762, excitation 360/40 nm, emission 460/50 nm) and TRITC (BZ-X Filter OP-87764, excitation 545/25 nm, emission 605/70 nm) were used to image the waveguiding (autofluorescence of PluDA) and scattering (Crimson FluoSpheres) segments, respectively. The fluorescence images were analyzed using a custom Python script that sums the intensity values of all pixels in the y-axis for a given 1 pixel-wide position on x-axis. This cumulative intensity was then normalized by the maximum column value of the image. For segmented fibers, the SciPy library [149]was used for detection of baseline, peaks, and peaks full width at half maximum (FWHM). The FWHM values and the spacings between them were taken as the segment lengths and the blank lengths respectively.

Fabrication of tailored side-emitting optical fibers

A segmented fiber with scattering segments was designed to outcouple 60 % of light over a 30 mm fiber length using scattering segments of different lengths. The design considered the attenuation coefficient of 1.4 cm^{-1} at 520 nm of the ink containing 0.01 % w/w FluoSpheres. The attenuation coefficient for the scattering fiber (0.96 cm^{-1}) could have also been used for designing the segment lengths. As the values are relatively close to one another, and are both only approximations for light loss behaviour in the first millimetre of scattering segments given interface effects when transitioning from waveguiding to scattering material, we arbitrarily used the bulk value. The design targeted equal light outcoupling segments and, therefore, the segment lengths increased along the optical fiber to compensate for decreasing power remaining within the fiber. The scattering lengths were calculated by dividing the exponential decay curve for a continuous scattering segment into 10 portions, each losing an equal amount of light. The mid-points of the 10 segments were then placed evenly along the 30 mm length . The design was fabricated by first assessing the flowrate of the waveguiding and scattering channels on the day of fabrication and using this to convert the desired segment lengths into switching times. The fibers were imaged by fluorescence microscopy and the scattering and waveguiding segment lengths were quantified using Python as described above.

Quantification of side-emission in air

Side-emission was measured by focusing a 520-nm laser (Compact Laser Modules with Phono Jack, 4.5 mW, Thorlabs) onto the proximal tip of each fiber using a planoconvex lens (f80, quartz glass, LINOS). A monochrome camera (Thorlabs DCC1545M) was set perpendicular to the fiber axis for imaging. Side-emission images were processed using the same Python script as for the fluorescence images to obtain the side-emission intensity as a function of fiber length. For determining the attenuation coefficient of scattering material, the side emission profiles for three separate fibers containing a ca. 30 mm scattering segment were fitted with an exponential decay function using Origin. The maximum in side-emission intensity occurs several millimeters beyond the start of the scattering segment due to the transition between waveguiding and scattering inks, and the exponential fit was therefore performed in the second half of the fiber.
For determining the proportion of light emitted from each segment of the tailored 10-segment fiber design, each segment's peak area was divided by the sum of the peak areas for all 10 segments. For determining optical loss in the waveguiding fiber, a 550-nm long-pass filter was placed in front of the camera lens to image only the autofluorescence generated in the fiber according to our previously reported method for hydrogel fibers.[81] Autofluorescence was preferred over scattering for the waveguiding fiber since the scattering signal can be easily dominated by fiber defects, while these do not impact the autofluorescence signal.

Activation of fluorescence inside a gelatine hydrogel with a segmented fiber

A printed 10-segment fiber was cladded by immersion in sodium alginate solution (2 % w/w) for 1 minute followed by immersion in calcium chloride solution (100 mmol L^{-1}).

A fluorescent hydrogel was prepared by dissolving gelatin (porcine skin, 300 g Bloom, Sigma-Aldrich) in DI water at 9.1 % w/w and heating to 70 °C with stirring. The gelatin solution was split into two portions. In one portion, red FluoSpheres (F8810, 200 nm diameter, fluorescent dye excitation and emission 580/605 respectively, Thermo Fisher Scientific) (0.4 % w/w) were added, and in the other portion carbon black (0.5 % w/w) was added and stirred for 2 h until fully dispersed. The solutions were used to fill a customized mold as follows.

A PVC mold containing a 1.3-mm wide groove for housing the optical fiber and a surrounding lip for filling the fluorescent gelatin was fabricated by CNC laser cutting. At the proximal end of the mold, a reservoir was introduced for placing gelatin containing carbon black. This mold was designed to facilitate i. straight and horizonal orientation of the fiber, ii. surrounding the first few centimeters of the fiber with carbon-black containing gelatin for blocking stray light from the

incoupling process, and iii. surrounding each side of the fiber with a thin layer of fluorescent gelatin for observing outcoupling from scattering segments.

The printed fiber was placed inside the groove and clamped at both ends. Gelatin solution containing carbon black was pipetted into the reservoir and the surrounding of the fiber up to 2 cm from the fiber tip. The fluorescent gelatin solution was pipetted around the rest of the fiber giving a consistent thickness layer of gelatin at both sides of the fiber and < 1 mm over the top of the fiber. 520 nm light was focused on the proximal tip of the fiber as described above for the side-emission experiments in air. Outcoupling of 520-nm light was imaged using a Sony Alpha 7. A 550-nm long pass filter was positioned in front of the camera lens to image the generated fluorescence.

Waveguiding properties in segmented core-cladding (macroscopic images)

The fibers were printed as described in the protocol. For imaging, the fibers were placed on non-reflective black substrates. An iPhone flashlight and a HJ portable laser diode (630-650 nm) were used as light sources. Images were captured using a Sony Alpha ILCE-7M4 camera with settings of ISO 640 and an aperture of f/8.

Refractometry

RI measurements were performed using a multiwavelength refractometer (Abbemat MW, Anton Paar Germany GmbH, Ostfildern-Scharnhausen, Serial Number: 81700806) at wavelengths 435.9, 480.5, 486.4, 547.0, 589.3, 646.3, and 656.0 nm. Circular hydrogel samples with a diameter of 9 to 10 mm and a thickness of 1 mm were used for the measurements. The sample was applied to the prism surface of the refractometer, ensuring complete coverage of the measuring area. A waiting period of 60 seconds was applied to allow the sample to equilibrate to the prism temperature, which was set at 20 °C. Measurements at the different wavelengths were conducted sequentially and readings were recorded once stable values were displayed for each wavelength.

Printing of segmented Plasmonic optical fibers

A segmented fiber with plasmonic segments was designed to absorb ≈ 90 % and ≈ 60 % of light over a 5 mm and 2 mm plasmonic segment length. The design was based on an attenuation coefficient of 0.4 cm^{-1} at 808 nm for ink containing 0.07 mg mL^{-1} AuNRs. Fibers with two consecutive 2 mm plasmonic segments separated by a 2 mm waveguiding segment were printed. On the day of printing, the flow rates for the waveguiding and plasmonic channels were measured

and used to convert the intended segment lengths into appropriate switching times. The fibers were analyzed using fluorescence microscopy, and the lengths of the scattering and waveguiding segments were quantified through Python-based image analysis, as previously described.

Quantification of gel fraction of printed PluDA fibers

Printed fibers of a length of 10 cm were cut and placed into pre-weighed glass vials. The vials containing the fibers were freeze-dried to remove water and weighed ($M1$). 5 mL of Mili-Q water was added to each vial to full cover the fibers and the vials were kept at room temperature for 24 hours to allow swelling and release of non-crosslinked material. Fibers were removed from the water, freeze-dried again and weighed ($M2$). The gel fraction was calculated as the ratio of the initial weight (M1) to the post-swelling weight ($M2$):

$$Gel\ fraction\ = \frac{M2}{M1} \times 100$$

This ratio represents the proportion of the crosslinked polymer network that remains insoluble after the swelling and washing process.

Quantification of swelling ratio

The swelling ratio of the printed fiber segments (2 cm in length) was determined as follows: The initial mass of the fibers was measured immediately after printing (W1). The fibers were immersed in 5 mL of Milli-Q water in well plates and stored under three different conditions: room temperature, incubator at 37 °C, and oven at 40 °C. At specified time intervals (30, 60, 120, 240 minutes, and 24 hours), the swollen fibers were removed, gently dried with a tissue to remove surface water, and their mass was measured (W2). The swelling ratio of the fibers was then calculated using the formula:

$$Swelling\ ratio\ = \frac{W_2 - W_1}{W_1} \times 100$$

Incoupling NIR laser to the fibers

The printed fibers were swollen in Milli-Q water for 2 hours. Fibers were placed in a custom 3D-printed holder and positioned inside a quartz cuvette (5 cm × 5 cm × 5 cm) (Hellma, spectral range 360-2500 nm, chamber volume 88000 µL, Merk) containing 13 mL of Milli-Q water to

prevent dehydration during the experiment. The cuvette was mounted on an adjustable platform, allowing movement in three directions to incouple the laser beam. A 808 ± 5 nm laser (CNI , INFRARED DIODE LASER AT 808nm ,3~6 W) was focused into the proximal tip of the printed fibers using a 4X microscope objective (Olympus Plan N 4X /0.10 Infinits/- UIS-2 FN22). The laser beam was directed into the 4X objective via two reflective mirrors (Thorlabs BB1-E02 Ø25,4mm ,400-750nm). To align the laser with the fiber, a monochrome camera (DCC1545M - USB 2.0 CMOS Camera, 1280 x 1024, Monochrome Sensor) was used to capture images of the proximal tip, assisted by the placement of a beam splitter (Fused silica, thickness 0.25 mm, 50.8 mm dimeter) and beam trap (customized , aluminum tube and PLA 3D printed) between the mirrors and the focusing lens. An IR camera (VarioCam@HD 980 S, Infratech, Germany) was positioned perpendicular to the fiber axis to capture thermal imaging for heat assessment. The heating images were processed using software IRBIS 3.1. The diameter of the extruded fibers was 1 mm. The laser power was measured using power meter (FieldMaster, Coherent Corp.) immediately after the 4x objective.

A K-Type thermocouple (1.4541 stainless steel) was stiched in the fiber near the segment (≈ 1 mm) to measure the internal temperature.

Quantification of heating as a function of laser intensity and illumination cycles

In the experiments with top illumiation, the fiber in the cuvette was exposed to a 808 nm laser focused to a 10 mm diameter beam and positioned at the top of the plasmonic segment. The IR camera was positioned perpendicular to the fiber axis for heat recording. Each experiment involved three cycles of laser exposure with a 10-minute duration per cycle and a 5-minute cooling interval between cycles. Recording began 2 minutes prior to laser activation.

For the experiments with incoupled light, a laser was incoupled on fibers containing 2 mm plasmonic segments, and temperature distribution profiles were imaged while varying the laser power (20 ± 1, 164 ± 1, 302 ± 1, 437 ± 2, 576 ± 2, 683 ± 1 mW). At each intensity, the temperature distribution was imaged. Imaging was started 2 minutes before the laser was turned on, during 10 min of laser irradiation, and the subsequent 5 minutes after the laser was turned off.

To assess the thermal stability of the fibers under high temperatures, 6 cycles of 10-minute laser exposure with 5 % (576 ± 2 mW) power were performed as part of the same experiment. The heating images were processed using software IRBIS 3.1.

Schematics

Schematics were drawn using Biorender and Microsoft powerpoint.

7. References

[1] P. Y. M. Yew, P. L. Chee, Q. Lin, C. Owh, J. Li, Q. Q. Dou, X. J. Loh, D. Kai, Y. Zhang, *Bioactive Materials* **2024**, 37, 407.

[2] a)W. Yan, A. Page, T. Nguyen-Dang, Y. Qu, F. Sordo, L. Wei, F. Sorin, *Advanced materials* **2019**, 31, 1802348; b)G. Loke, W. Yan, T. Khudiyev, G. Noel, Y. Fink, *Advanced Materials* **2020**, 32, 1904911; c)G. Loke, R. Yuan, M. Rein, T. Khudiyev, Y. Jain, J. Joannopoulos, Y. Fink, *Nature communications* **2019**, 10, 4010.

[3] a)S. Johannsmeier, M. L. Torres-Mapa, D. Dipresa, T. Ripken, D. Heinemann, A. Heisterkamp, *Optical Materials Express* **2019**, 9, 3925; b)M. Choi, M. Humar, M. S. Kim, S.-H. Yun, *Advanced materials (Deerfield Beach, Fla.)* **2015**, 27, 4081.

[4] J. Mueller, J. R. Raney, K. Shea, J. A. Lewis, *Advanced Materials* **2018**, 30, 1705001.

[5] S. Hassan, E. Gomez-Reyes, E. Enciso-Martinez, K. Shi, J. G. Campos, O. Y. P. Soria, E. Luna-Cerón, M. C. Lee, I. Garcia-Reyes, J. Steakelum, H. Jeelani, L. E. García-Rivera, M. Cho, S. S. Cortes, T. Kamperman, H. Wang, J. Leijten, L. Fiondella, S. R. Shin, *ACS Applied Materials & Interfaces* **2022**, 14, 51602.

[6] X. Li, J. M. Zhang, X. Yi, Z. Huang, P. Lv, H. Duan, *Advanced Science* **2019**, 6, 1800730.

[7] N. M. Larson, J. Mueller, A. Chortos, Z. S. Davidson, D. R. Clarke, J. A. Lewis, *Nature* **2023**, 613, 682.

[8] T. J. Ober, D. Foresti, J. A. Lewis, *Proceedings of the National Academy of Sciences* **2015**, 112, 12293.

[9] a)M. A. Skylar-Scott, J. Mueller, C. W. Visser, J. A. Lewis, *Nature* **2019**, 575, 330; b)I. Hassan, P. R. Selvaganapathy, *Advanced Materials Technologies* **2022**, 7, 2101709.

[10] J. Karvinen, M. Kellomäki, *Bioprinting* **2023**, 32, e00274.

[11] J. O. Hardin, T. J. Ober, A. D. Valentine, J. A. Lewis, *Advanced materials* **2015**, 27, 3279.

[12] Y. Yamada, *Annual Review of Heat Transfer* **1995**, 6.

[13] a)L. Acker, E. N. Pino, E. S. Boyden, R. Desimone, *Proceedings of the National Academy of Sciences* **2016**, 113, E7297; b)R. Nazempour, Q. Zhang, R. Fu, X. Sheng, *Materials* **2018**, 11, 1283.

[14] A. Alabugin, *Photochemistry and Photobiology* **2019**, 95, 722.

[15] C. E. Tedford, S. DeLapp, S. Jacques, J. Anders, *Lasers in surgery and medicine* **2015**, 47, 312.

[16] A. Kienle, R. Hibst, *Physical review letters* **2006**, 97, 018104.

[17] S. Pearson, J. Feng, A. del Campo, *Advanced Functional Materials* **2021**, 31, 2105989.

[18] S. He, J. Song, J. Qu, Z. Cheng, *Chemical Society Reviews* **2018**, 47, 4258.

[19] N. Ioannides, E. Chunga, A. Bachmatiuk, I. Gonzalez-Martinez, B. Trzebicka, D. Adebimpe, D. Kalymnios, M. H. Rümmeli, *Materials Research Express* **2014**, 1, 032002.

[20] G. Hocker, *Applied optics* **1979**, 18, 1445.

[21] R. C. Allil, M. M. Werneck, *IEEE Transactions on instrumentation and measurement* **2011**, 60, 2118.

[22] D. R. Biswas, *Optical engineering* **1992**, 31, 1400.
[23] Y.-H. Wu, H. B. Park, T. Kai, B. D. Freeman, D. S. Kalika, *Journal of Membrane Science* **2010**, 347, 197.
[24] Harshita, H. F. Wu, S. K. Kailasa, *Luminescence* **2023**, 38, 954.
[25] Y. J. Heo, H. Shibata, T. Okitsu, T. Kawanishi, S. Takeuchi, *Proceedings of the National Academy of Sciences* **2011**, 108, 13399.
[26] C. Zhang, G. G. Cano, P. V. Braun, *Advanced Materials* **2014**, 26, 5678.
[27] R. Boushel, C. Piantadosi, *Acta Physiologica Scandinavica* **2000**, 168, 615.
[28] A. Okamoto, *Chemical Society Reviews* **2011**, 40, 5815.
[29] L. Wu, C. Huang, B. P. Emery, A. C. Sedgwick, S. D. Bull, X.-P. He, H. Tian, J. Yoon, J. L. Sessler, T. D. James, *Chemical Society Reviews* **2020**, 49, 5110.
[30] A. K. Yetisen, N. Jiang, A. Fallahi, Y. Montelongo, G. U. Ruiz-Esparza, A. Tamayol, Y. S. Zhang, I. Mahmood, S. A. Yang, K. S. Kim, *Advanced Materials (Deerfield Beach, Fla.)* **2017**, 29.
[31] J. S. Gootenberg, O. O. Abudayyeh, J. W. Lee, P. Essletzbichler, A. J. Dy, J. Joung, V. Verdine, N. Donghia, N. M. Daringer, C. A. Freije, *Science* **2017**, 356, 438.
[32] J. Shen, C. Chui, X. Tao, *Biomedical Optics Express* **2013**, 4, 2925.
[33] a)J.-H. Choi, D. Oh, J. H. Lee, J.-h. Park, K.-p. Kim, S. S. Lee, Y.-J. Lee, Y.-S. Lim, T. J. Song, S. S. Lee, *Endoscopy* **2015**, 47, 1035; b)J. M. DeWitt, K. Sandrasegaran, B. O'Neil, M. G. House, N. J. Zyromski, A. Sehdev, S. M. Perkins, J. Flynn, L. McCranor, S. Shahda, *Gastrointestinal endoscopy* **2019**, 89, 390; c)C. Vicentini, A.-S. Vignion-Dewalle, E. Thecua, F. Lecomte, C. Maire, P. Deleporte, H. Behal, D. Kerob, A. Duhamel, S. Mordon, *British Journal of Dermatology* **2019**, 180, 765.
[34] H. Zhao, X. Wang, Z. Geng, N. Liang, Q. Li, X. Hu, Z. Wei, *Lab on a Chip* **2022**, 22, 4521.
[35] A. M. Fard, A. L. Reynolds, J. H. Lillvis, N. D. Nader, *Journal of American Association for Pediatric Ophthalmology and Strabismus* **2020**, 24, 331.
[36] S. J. Kwok, S. Forward, C. M. Wertheimer, A. C. Liapis, H. H. Lin, M. Kim, T. G. Seiler, R. Birngruber, I. E. Kochevar, T. Seiler, *Investigative ophthalmology & visual science* **2019**, 60, 2563.
[37] L. F. De Freitas, M. R. Hamblin, *IEEE Journal of selected topics in quantum electronics* **2016**, 22, 348.
[38] J. Shen, X. Tao, D. Ying, C. Hui, G. Wang, *Textile Research Journal* **2013**, 83, 730.
[39] R. S. Riley, E. S. Day, *Wiley Interdisciplinary Reviews: Nanomedicine and Nanobiotechnology* **2017**, 9, e1449.
[40] J. R. Melamed, R. S. Edelstein, E. S. Day, *ACS nano* **2015**, 9, 6.
[41] a)S. Lal, S. E. Clare, N. J. Halas, *Accounts of chemical research* **2008**, 41, 1842; b)L. Zou, H. Wang, B. He, L. Zeng, T. Tan, H. Cao, X. He, Z. Zhang, S. Guo, Y. Li, *Theranostics* **2016**, 6, 762.
[42] Y. Ran, Z. Xu, M. Chen, W. Wang, Y. Wu, J. Cai, J. Long, Z. S. Chen, D. Zhang, B. O. Guan, *Advanced science* **2022**, 9, 2200456.
[43] a)K. Deisseroth, *Nature methods* **2011**, 8, 26; b)K. Deisseroth, *Nature neuroscience* **2015**, 18, 1213.
[44] K. L. Montgomery, S. M. Iyer, A. J. Christensen, K. Deisseroth, S. L. Delp, *Science translational medicine* **2016**, 8, 337rv5.

[45] C. Crocini, C. Ferrantini, F. S. Pavone, L. Sacconi, *Progress in Biophysics and Molecular Biology* **2017**, 130, 132.
[46] J.-A. Sahel, E. Boulanger-Scemama, C. Pagot, A. Arleo, F. Galluppi, J. N. Martel, S. D. Esposti, A. Delaux, J.-B. de Saint Aubert, C. de Montleau, *Nature medicine* **2021**, 27, 1223.
[47] F. Pisanello, G. Mandelbaum, M. Pisanello, I. A. Oldenburg, L. Sileo, J. E. Markowitz, R. E. Peterson, A. Della Patria, T. M. Haynes, M. S. Emara, *Nature neuroscience* **2017**, 20, 1180.
[48] M. Choi, J. W. Choi, S. Kim, S. Nizamoglu, S. K. Hahn, S. H. Yun, *Nature photonics* **2013**, 7, 987.
[49] a)S. Park, Y. Guo, X. Jia, H. K. Choe, B. Grena, J. Kang, J. Park, C. Lu, A. Canales, R. Chen, *Nature neuroscience* **2017**, 20, 612; b)A. Canales, X. Jia, U. P. Froriep, R. A. Koppes, C. M. Tringides, J. Selvidge, C. Lu, C. Hou, L. Wei, Y. Fink, *Nature biotechnology* **2015**, 33, 277.
[50] N. Tanio, Y. Koike, *Polymer Journal* **2000**, 32, 43.
[51] D. Cai, A. Neyer, R. Kuckuk, H. Heise, *Optical materials* **2008**, 30, 1157.
[52] a)C. Wu, X. Liu, Y. Ying, *ACS sensors* **2021**, 6, 1446; b)H. Ma, A. Y. Jen, L. R. Dalton, *Advanced materials* **2002**, 14, 1339.
[53] G. Hougham, G. Tesoro, A. Viehbeck, J. Chapple-Sokol, *Macromolecules* **1994**, 27, 5964.
[54] R. J. Schechter, *Survey of Ophthalmology* **1977**, 21, 464.
[55] N. A. Mortensen, J. R. Folken, P. M. Skovgaard, J. Broeng, *IEEE Photonics Technology Letters* **2002**, 14, 1094.
[56] R. Khan, B. Gul, S. Khan, H. Nisar, I. Ahmad, *Photodiagnosis and Photodynamic Therapy* **2021**, 33, 102192.
[57] J. Zubia, G. Aldabaldetreku, G. Durana, J. Arrue, F. Jimenez, *Laser & Photonics Reviews* **2008**, 2, 182.
[58] R. T. Chen, L. Sadovnik, T. Jannson, J. Jannson, *Applied physics letters* **1991**, 58, 1.
[59] M. Pisanello, A. Della Patria, L. Sileo, B. L. Sabatini, M. De Vittorio, F. Pisanello, *Biomedical optics express* **2015**, 6, 4014.
[60] J. Feng, Y. Zheng, Q. Jiang, M. K. Włodarczyk-Biegun, S. Pearson, A. del Campo, *Advanced Materials Technologies* **2022**, 7, 2101539.
[61] S. Nizamoglu, M. C. Gather, M. Humar, M. Choi, S. Kim, K. S. Kim, S. K. Hahn, G. Scarcelli, M. Randolph, R. W. Redmond, *Nature communications* **2016**, 7, 10374.
[62] R. Ramaswami, K. Sivarajan, G. Sasaki, *Optical networks: a practical perspective*, Morgan Kaufmann, **2009**.
[63] R. C. da Silva Barros Allil, M. M. Werneck, *IEEE TRANSACTIONS ON INSTRUMENTATION AND MEASUREMENT IM* **2011**, 60, 2118.
[64] M. K. Szczurowski, T. Martynkien, G. Statkiewicz-Barabach, L. Khan, D. J. Webb, C. Ye, J. Dulieu-Barton, W. Urbanczyk, presented at *Photonic Crystal Fibers IV*, **2010**.
[65] R. Fu, W. Luo, R. Nazempour, D. Tan, H. Ding, K. Zhang, L. Yin, J. Guan, X. Sheng, *Advanced Optical Materials* **2018**, 6, 1700941.
[66] V. Egorov, S. Tsyuryupa, S. Kanilo, M. Kogit, A. Sarvazyan, *Medical engineering & physics* **2008**, 30, 206.
[67] S. P. Lacour, G. Courtine, J. Guck, *Nature Reviews Materials* **2016**, 1, 1.
[68] a)B. Galateanu, A. Hudita, C. Zaharia, M.-C. Bunea, E. Vasile, M.-R. Buga, M. Costache, *Polym. Polym. Compos. A Ref. Ser* **2019**, 1791; b)T. Shu, K. Zheng, Z. Zhang, J. Ren, Z. Wang, Y. Pei, J. Yeo, G. X. Gu, S. Ling, *Biomacromolecules* **2021**, 22, 1955.

[69] J. Guo, B. Zhou, C. Yang, Q. Dai, L. Kong, *Advanced Functional Materials* **2019**, 29, 1902898.
[70] D. Shan, C. Zhang, S. Kalaba, N. Mehta, G. B. Kim, Z. Liu, J. Yang, *Biomaterials* **2017**, 143, 142.
[71] F. Abbasi, H. Mirzadeh, A. A. Katbab, Wiley Online Library, 2001.
[72] J. Missinne, S. Kalathimekkad, B. Van Hoe, E. Bosman, J. Vanfleteren, G. Van Steenberge, *Opt. Express* **2014**, 22, 4168.
[73] L. Y. Tyng, M. R. Ramli, M. B. H. Othman, R. Ramli, Z. A. M. Ishak, Z. Ahmad, *Polymer international* **2013**, 62, 382.
[74] I. Martincek, D. Pudis, M. Chalupova, *IEEE Photonics technology letters* **2014**, 26, 1446.
[75] a)F. Pisano, M. Pisanello, S. J. Lee, J. Lee, E. Maglie, A. Balena, L. Sileo, B. Spagnolo, M. Bianco, M. Hyun, *Nature methods* **2019**, 16, 1185; b)M. Pisanello, F. Pisano, L. Sileo, E. Maglie, E. Bellistri, B. Spagnolo, G. Mandelbaum, B. L. Sabatini, M. De Vittorio, F. Pisanello, *Scientific reports* **2018**, 8, 4467.
[76] M. B. Applegate, G. Perotto, D. L. Kaplan, F. G. Omenetto, *Biomedical optics express* **2015**, 6, 4221.
[77] S. J. Kwok, M. Kim, H. H. Lin, T. G. Seiler, E. Beck, P. Shao, I. E. Kochevar, T. Seiler, S.-H. Yun, *Investigative ophthalmology & visual science* **2017**, 58, 2596.
[78] Y. Shen, Z. Wang, Z. Wang, J. Wang, X. Yang, X. Zheng, H. Chen, K. Li, L. Wei, T. Zhang, *InfoMat* **2022**, 4, e12318.
[79] A. Evertz, D. Schrein, E. Olsen, G.-A. Hoffmann, L. Overmeyer, *Optical Fiber Technology* **2021**, 66, 102638.
[80] J. Feng, Q. Jiang, P. Rogin, P. W. de Oliveira, A. Del Campo, *ACS applied materials & interfaces* **2020**, 12, 20287.
[81] J. Feng, Y. Zheng, S. Bhusari, M. Villiou, S. Pearson, A. del Campo, *Advanced functional materials* **2020**, 30, 2004327.
[82] S. T. Parker, P. Domachuk, J. Amsden, J. Bressner, J. A. Lewis, D. L. Kaplan, F. G. Omenetto, *Advanced Materials* **2009**, 21.
[83] H. Orelma, A. Hokkanen, I. Leppänen, K. Kammiovirta, M. Kapulainen, A. Harlin, *Cellulose* **2020**, 27, 1543.
[84] A. Leber, C. Dong, S. Laperrousaz, H. Banerjee, M. E. Abdelaziz, N. Bartolomei, B. Schyrr, B. Temelkuran, F. Sorin, *Advanced Science* **2023**, 10, 2204016.
[85] D. Liu, J. Ren, J. Wang, W. Xing, Q. Qian, H. Chen, N. Zhou, *Journal of Materials Chemistry C* **2020**, 8, 15092.
[86] J. Ren, D. Liu, B. Zhang, J. Wang, H. Chen, Y. Yao, Z. Wang, N. Zhou, *Additive Manufacturing* **2024**, 87, 104234.
[87] C. F. Guimarães, R. Ahmed, A. Mataji-Kojouri, F. Soto, J. Wang, S. Liu, T. Stoyanova, A. P. Marques, R. L. Reis, U. Demirci, *Advanced Materials* **2021**, 33, 2105361.
[88] J. Ren, D. Liub, B. Zhangb, J. Wang, H. Chen, Y. Yao, Z. Wang, N. Zhou, *Additive Manufacturing* **2024**, 104234.
[89] J. Chen, H. Wen, G. Zhang, F. Lei, Q. Feng, Y. Liu, X. Cao, H. Dong, *ACS applied materials & interfaces* **2020**, 12, 7565.
[90] Z. Zhao, E. Shang, N. Zhang, Y. Xiong, Y. Liu, H. Zhang, W. Chen, D. Fan, *Journal of Food Engineering* **2025**, 384, 112240.

[91] A. M. Aravanis, L.-P. Wang, F. Zhang, L. A. Meltzer, M. Z. Mogri, M. B. Schneider, K. Deisseroth, *Journal of neural engineering* **2007**, 4, S143.
[92] M. Cinquino, C. T. Prontera, M. Pugliese, R. Giannuzzi, D. Taurino, G. Gigli, V. Maiorano, *Micromachines* **2021**, 12, 652.
[93] T. Dias, R. Monaragala, *Textile Research Journal* **2012**, 82, 1164.
[94] L. Alidokht, K. Fitzpatrick, C. Butler, K. Z. Hunsucker, C. Braga, W. A. Maza, K. P. Fears, M. Arekhi, M. Lanzarini-Lopes, *Biofilm* **2024**, 7, 100186.
[95] Y. Oguz, C. Cochrane, S. R. Mordon, J. C. Lesage, V. Koncar, in *Advances in Smart Medical Textiles*, Elsevier, 2016.
[96] E. Segev, J. Reimer, L. C. Moreaux, T. M. Fowler, D. Chi, W. D. Sacher, M. Lo, K. Deisseroth, A. S. Tolias, A. Faraon, *Neurophotonics* **2017**, 4, 011002.
[97] J. Guo, H. Huang, M. Zhou, C. Yang, L. Kong, *Analytical chemistry* **2018**, 90, 12292.
[98] E. Ujah, M. Lai, G. Slaughter, *Scientific Reports* **2023**, 13, 4495.
[99] L. Wondraczek, A. Gründler, A. Reupert, K. Wondraczek, M. A. Schmidt, G. Pohnert, S. Nolte, *Scientific reports* **2019**, 9, 9600.
[100] J. Schröder, A. Reupert, L. Wondraczek, *Optical Materials Express* **2022**, 12, 2318.
[101] J. Xu, Y. Ao, D. Fu, Y. Lin, X. Shen, C. Yuan, Z. Yin, *Journal of Photochemistry and Photobiology A: Chemistry* **2008**, 199, 165.
[102] M. Lanzarini-Lopes, B. Cruz, S. Garcia-Segura, A. Alum, M. Abbaszadegan, P. Westerhoff, *Environmental science & technology* **2019**, 53, 10880.
[103] S. Shabahang, S. Forward, S.-H. Yun, *Opt. Express* **2019**, 27, 7560.
[104] F. Pisanello, L. Sileo, I. A. Oldenburg, M. Pisanello, L. Martiradonna, J. A. Assad, B. L. Sabatini, M. De Vittorio, *Neuron* **2014**, 82, 1245.
[105] M. Lanzarini-Lopes, Z. Zhao, F. Perreault, S. Garcia-Segura, P. Westerhoff, *Water Research* **2020**, 184, 116191.
[106] S. M. Bilankohi, *Oriental Journal of Chemistry* **2015**, 31, 2259.
[107] A. Guglielmelli, F. Pierini, N. Tabiryan, C. Umeton, T. J. Bunning, L. De Sio, *Advanced Photonics Research* **2021**, 2, 2000198.
[108] J. Zeng, D. Shi, Y. Gu, T. Kaneko, L. Zhang, H. Zhang, D. Kaneko, M. Chen, *Biomacromolecules* **2019**, 20, 3375.
[109] S. Jiang, K. Wang, Y. Dai, X. Zhang, F. Xia, *Macromolecular Materials and Engineering* **2019**, 304, 1900087.
[110] M. Liu, P. Huang, W. Wang, Z. Feng, J. Zhang, L. Deng, A. Dong, *Journal of Materials Chemistry B* **2019**, 7, 2667.
[111] C. Lee, K. Lim, S. S. Kim, E. S. Lee, K. T. Oh, H.-G. Choi, Y. S. Youn, *Journal of Controlled Release* **2019**, 294, 77.
[112] S. Basaran, S. Dey, S. Bhusari, S. Sankaran, T. Kraus, *Biomaterials Advances* **2023**, 147, 213332.
[113] E. Lacroce, L. Bianchi, L. Polito, S. Korganbayev, A. Molinelli, A. Sacchetti, P. Saccomandi, F. Rossi, *Nanoscale Advances* **2023**, 5, 6870.
[114] B. Liu, H. Zhu, D. Zhao, G. Nian, S. Qu, W. Yang, *Advanced Optical Materials* **2021**, 9, 2101036.
[115] D. Jaque, L. M. Maestro, B. del Rosal, P. Haro-Gonzalez, A. Benayas, J. Plaza, E. M. Rodríguez, J. G. Solé, *nanoscale* **2014**, 6, 9494.

[116] S. Li, C. Yang, J. Li, C. Zhang, L. Zhu, Y. Song, Y. Guo, R. Wang, D. Gan, J. Shi, *International Journal of Nanomedicine* **2023**, 4485.
[117] M. Di Biase, P. De Leonardis, V. Castelletto, I. W. Hamley, B. Derby, N. Tirelli, *Soft Matter* **2011**, 7, 4928.
[118] M. Bohorquez, C. Koch, T. Trygstad, N. Pandit, *Journal of colloid and interface science* **1999**, 216, 34.
[119] R. N. Shamma, R. H. Sayed, H. Madry, N. S. El Sayed, M. Cucchiarini, *Tissue Engineering Part B: Reviews* **2022**, 28, 451.
[120] P. Linse, *Macromolecules* **1993**, 26, 4437.
[121] C. Wu, T. Liu, B. Chu, D. K. Schneider, V. Graziano, *Macromolecules* **1997**, 30, 4574.
[122] K. Mortensen, Y. Talmon, *Macromolecules* **1995**, 28, 8829.
[123] a)S. Bhusari, M. Hoffmann, P. Herbeck-Engel, S. Sankaran, M. Wilhelm, A. Del Campo, *Soft matter* **2024**, 20, 1320; b)R. K. Prud'homme, G. Wu, D. K. Schneider, *Langmuir* **1996**, 12, 4651; c)K. Mortensen, W. Batsberg, S. Hvidt, *Macromolecules* **2008**, 41, 1720.
[124] a)D. Missirlis, N. Tirelli, J. A. Hubbell, *Langmuir* **2005**, 21, 2605; b)M. Di Biase, R. E. Saunders, N. Tirelli, B. Derby, *Soft Matter* **2011**, 7, 2639.
[125] a)C. R. López-Barrón, R. Chen, N. J. Wagner, P. J. Beltramo, *Macromolecules* **2016**, 49, 5179; b)M. Müller, J. Becher, M. Schnabelrauch, M. Zenobi-Wong, *Biofabrication* **2015**, 7, 035006.
[126] W. Wu, A. DeConinck, J. A. Lewis, *Advanced materials* **2011**, 23, H178.
[127] H. Priks, T. Butelmann, A. Illarionov, T. G. Johnston, C. Fellin, T. Tamm, A. Nelson, R. Kumar, P.-J. Lahtvee, *ACS applied bio materials* **2020**, 3, 4273.
[128] X. Liu, H. Yuk, S. Lin, G. A. Parada, T. C. Tang, E. Tham, C. de la Fuente-Nunez, T. K. Lu, X. Zhao, *Advanced Materials* **2018**, 30, 1704821.
[129] J. D. Weiss, A. Mermin-Bunnell, F. S. Solberg, T. Tam, L. Rosalia, A. Sharir, D. Rutsche, S. Sinha, P. S. Choi, M. Shibata, *bioRxiv* **2024**, 2024.10. 01.615991.
[130] S. Hassan, E. Gomez-Reyes, E. Enciso-Martinez, K. Shi, J. G. Campos, O. Y. P. Soria, E. Luna-Cerón, M. C. Lee, I. Garcia-Reyes, J. Steakelum, *ACS applied materials & interfaces* **2022**, 14, 51602.
[131] S. Shabahang, S. Kim, S. H. Yun, *Advanced Functional Materials* **2018**, 28, 1706635.
[132] V. Lenaerts, C. Triqueneaux, M. Quartern, F. Rieg-Falson, P. Couvreur, *International journal of pharmaceutics* **1987**, 39, 121.
[133] M. Jalaal, G. Cottrell, N. Balmforth, B. Stoeber, *Journal of Rheology* **2017**, 61, 139.
[134] Z. Fu, V. Angeline, W. Sun, *International journal of bioprinting* **2021**, 7.
[135] S. Bhusari, J. Kim, K. Polizzi, S. Sankaran, A. Del Campo, *Biomaterials Advances* **2023**, 145, 213240.
[136] D. C. Ames, S. Propst, A. Shah, J. Mueller, *Advanced Materials*, 2407599.
[137] I. Hassan, P. R. Selvaganapathy, *Additive Manufacturing* **2022**, 50, 102559.
[138] M. Matiatou, P. Giannios, S. Koutsoumpos, K. G. Toutouzas, G. C. Zografos, K. Moutzouris, *Results in Physics* **2021**, 22, 103833.
[139] C. Zhou, D. E. Heath, A. R. M. Sharif, S. Rayatpisheh, B. H. Oh, X. Rong, R. Beuerman, M. B. Chan-Park, *Macromolecular Bioscience* **2013**, 13, 1485.
[140] M. I. Lucío, A. Cubells-Gómez, Á. Maquieira, M.-J. Bañuls, *Analytical and Bioanalytical Chemistry* **2022**, 1.
[141] Y. Liu, S.-H. Chen, J. S. Huang, *Macromolecules* **1998**, 31, 6226.

[142] C. Wu, G. Xia, J. Sun, R. Song, *RSC advances* **2015**, 5, 97648.
[143] C. Chaibundit, N. M. Ricardo, F. d. M. Costa, S. G. Yeates, C. Booth, *Langmuir* **2007**, 23, 9229.
[144] M. R. McGrory, M. D. King, A. D. Ward, *The Journal of Physical Chemistry A* **2020**, 124, 9617.
[145] S. Ansari, M. A. I. Rashid, O. Chatterjee, P. R. Waghmare, Y. Ma, D. Nobes, presented at *Proceeding of the 10th, Pacific Symposium on Flow Visualization and Image Processing*, **2015**.
[146] D. B. Kolesky, R. L. Truby, A. S. Gladman, T. A. Busbee, K. A. Homan, J. A. Lewis, *Advanced materials* **2014**, 26, 3124.
[147] L. Raymond, W. Hua, N. Valentin, R. Coulter, E. Bandala, K. Leong, J. Okaikoi, Y. Jin, *Journal of Manufacturing Science and Engineering* **2024**, 146.
[148] Z. Kafrashian, S. Brück, P. Rogin, M. Khamdan, H. S. U. B. Farrukh, S. Pearson, A. Del Campo, *Advanced Materials* **2024**, 2309166.
[149] a)P. Virtanen, R. Gommers, T. E. Oliphant, M. Haberland, T. Reddy, D. Cournapeau, E. Burovski, P. Peterson, W. Weckesser, J. Bright, *Nature methods* **2020**, 17, 261; b)M. Mansouri, M.-D. Hussherr, T. Strittmatter, P. Buchmann, S. Xue, G. Camenisch, M. Fussenegger, *Nature communications* **2021**, 12, 3388.

8. Publications

Plasmonic Hydrogel-Based Segmented Waveguides for Targeted Photo-Thermal Therapy. (2025). Draft in preparation.

Fabrication Technologies for Soft, Multimaterial Optical Fibers for In Vivo Diagnostics and Phototherapy, With a Focus on Extrusion Printing (2026). *Advanced Materials Technologies.*

Approaches for side-emission in soft optical fibers (2025). Draft in preparation

Segmented, Side-Emitting Hydrogel Optical Fibers for Multimaterial Extrusion Printing. (2024). *Advanced Materials*.

Surfactant-assisted-water-exposed electrospinning of novel super hydrophilic Polycaprolactone-based fibers:Cell culture studies. (2019).

Journal of Biomedical Materials Research, Part A.

Surfactant-assisted-water-exposed electrospinning of novel super hydrophilic Polycaprolactone-based fibers: Analysis of drug release

behavior. (2018). *Journal of Biomedical Materials Research, Part A.*

9. Curriculum Vitae

Zahra Kafrashian

Date of Birth: December 8th, 1992

Place of Birth: Tehran, Iran

Education

11.11.2019-present PhD candidate at INM- Leibniz Institute for New Materials, Saarbrücken, Germany

Title of Thesis: Hydrogel-Based Side-Emitting Optical Waveguides for Light and Heat Delivery

Supervisor: Prof. Dr. Aránzazu del Campo Bécares

2016-2018 M.Sc. in Polymer Science and Engineering, Amirkabir University of Technology (Tehran Polytechnic), Tehran, Iran

Title of Thesis: Investigation and characterization of hydrophilic properties of electrospun nanofiberous PLGA/Pluronic blend and nanocomposite with nanohydroxyapatite

Supervisor: Prof. Dr. Vahid Haddadi

2012-2016 B.Sc. in Polymer Science and Engineering, Amirkabir University of Technology (Tehran Polytechnic), Tehran, Iran

Title of Thesis: Peripheral and kinetic study of amphiphilic chains in the vicinity of organic-aqueous solvents

Supervisor: Prof. Dr. Vahid Haddadi